PURE TENSILE FRACTURE MODELLING AND TOUGHNESS MEASUREMENTS
ON BRAZILIAN DISCS OF ANDESITE AND MARBLE

A THESIS SUBMITTED TO
THE GRADUATE SCHOOL OF NATURAL AND APPLIED SCIENCES
OF
MIDDLE EAST TECHNICAL UNIVERSITY

BY

CANSIN ÖZDOĞAN

IN PARTIAL FULFILLMENT OF THE REQUIREMENTS
FOR
THE DEGREE OF MASTER OF SCIENCE
IN
MINING ENGINEERING

AUGUST 2017

Approval of the thesis:

**PURE TENSILE FRACTURE MODELLING AND TOUGHNESS
MEASUREMENTS ON BRAZILIAN DISCS OF ANDESITE AND MARBLE**

submitted by **CANSIN ÖZDOĞAN** in partial fulfillment of the requirements for the
degree of **Master of Science in Mining Engineering Department, Middle East
Technical University** by,

Prof. Dr. Gülbin Dural Ünver
Dean, Graduate School of **Natural and Applied Science** _____

Prof. Dr. Celal Karpuz
Head of Department, **Mining Engineering** _____

Prof. Dr. Levend Tutluoğlu
Supervisor, **Mining Engineering Dept., METU** _____

Examining Committee Members:

Prof. Dr. Celal Karpuz
Mining Engineering Dept., METU _____

Prof. Dr. Levend Tutluoğlu
Mining Engineering Dept., METU _____

Prof. Dr. Tamer Topal
Geological Engineering Dept., METU _____

Assoc. Prof. Dr. H. Aydın Bilgin
Mining Engineering Dept., METU _____

Asst. Prof. Dr. İ. Ferid Öge
Mining Engineering Dept., Muğla Sıtkı Koçman Üniversitesi _____

Date: 14.08.2017

I hereby declare that all information in this document has been obtained and presented in accordance with academic rules and ethical conduct. I also declare that, as required by these rules and conduct, I have fully cited and referenced all material and results that are not original to this work.

Name, Last Name: Cansın Özdoğan

Signature:

iv

ABSTRACT

PURE TENSILE FRACTURE MODELLING AND TOUGHNESS MEASUREMENTS ON BRAZILIAN DISCS OF ANDESITE AND MARBLE

Özdoğan, Cansın

M.S., Department of Mining Engineering

Supervisor: Prof. Dr. Levend Tutluoğlu

August 2017, 148 pages

In fracture mechanics, mode I loading type is characterized by opening of cracks in tension. Considering the convenient availability samples from drilling work of the site investigations, core-based specimen geometries are commonly used in rock fracture testing. Three- or four-point bending loading and compressive loading are major loading configurations for fracture toughness testing.

For the investigation of geometric parameters in tensile fracturing of Brazilian disk type geometries, Flattened Brazilian disc (FBD) method is employed for mode I fracture toughness testing. This method is chosen due to simple specimen preparation procedure and loading configuration. Brazilian disc geometry is constructed with opposite flat ends corresponding to specific loading angles from the specimen center. Testing with this core-based geometry can be conducted without pre-cracking. Disc with flattened ends is subjected to compressive loading along vertical diametric line. Compressive loading generates a centerline crack under tensile opening mode.

Numerical modeling is conducted to compute mode I stress intensity factors for the centerline crack initiation. Parametric relations are proposed to express stress intensity

factor in terms of the geometric entities of the samples. Improved equations established the relations between the stress intensity factor and loading angle for a wider range of loading angles than those of the previous work. The range was expanded from $2°$ to $50°$.

Two rock types as Ankara andesite and Afyon marble were included in the testing work. Average mode I fracture toughness was measured as 2.58±0.34 MPa$\sqrt{m}$ and 3.43±0.27 MPa$\sqrt{m}$, respectively for 75 mm core specimens of andesite and marble. For 100 mm diameter samples, mode I toughness values were 3.34±0.15 MPa$\sqrt{m}$ for andesite and 3.04±0.70 MPa$\sqrt{m}$ for marble.

Specimen size effect on the toughness was investigated by employing two different diameters of 75 mm and 100 mm for andesite and marble core samples. The size effect is observed to be around 30% (3.34/2.58=1.29) for andesite having 75 mm and 100 mm diameter.

KEYWORDS: rock fracture testing, mode I fracture toughness, flattened Brazilian disc method, fracture numerical modelling

ÖZ

ANDEZİT VE MERMER BRAZİLYAN DİSKLERİNDE SAF ÇEKME KIRILMA MODELLEMESİ VE TOKLUK ÖLÇÜMÜ

Özdoğan, Cansın

Yüksek Lisans, Maden Mühendisliği Bölümü

Tez Yöneticisi: Prof. Dr. Levend Tutluoğlu

Ağustos 2017, 148 sayfa

Kırılma mekaniğinde mod I yüklemesi çekme etkisinden açılan çatlaklar ile karakterize edilmektedir. Kaya kırılma testlerinde karot bazlı numune geometrileri zemin etüdlerindeki delme faaliyetlerinden elde edilen numunelere kolay ulaşıldığından yaygın olarak kullanılmaktadır. Üç ile dört nokta eğilme ve basma yüklemeleri kırılma tokluğu testi için önemli yükleme şeklidir.

Brazilyan disk tipi geometrilerin çekme kırılmasına ilişkin boyutsal parametrelerinin araştırmasında mod I kırılma tokluğu testi için Düzleştirilmiş Brazilyan disk yöntemi kullanılmaktadır. Bu metod kolay numune hazırlama ve basit yükleme konfigürasyonu sebebiyle tercih edilmektedir. Brazilyan disk geometrisinin her iki zıt ucuda merkezden geçen belirli yükleme açılarına göre düzleştirilmiştir. Karot bazlı geometrilerin testi, henüz çatlak açılmadan gerçekleştirilebilmektedir. Düzleştirilmiş disk üzerinde basma yükü dikey çapsal hat boyunca etki etmektedir. Bu yük çekme etkisiyle merkez çizgisi boyunca çatlak oluşumunu sağlar.

Sayısal modelleme merkezde başlayan çatlak oluşumuna ilişkin mod I gerilme şiddeti faktörlerini hesaplamak amacıyla yapılmaktadır. Gerilme şiddeti faktörlerini numuneye özgü geometrik parametreler cinsinden ifade etmek için parametric denklemler

önerilmektedir. İyileştirilen formüller, gerilme şiddeti faktörü ile önceki çalışmalardan daha geniş bir yükleme açı aralığı arasında ilişki kurmuştur. Bu aralık, 2 derece ile 50 derece arasını kapsamaktadır.

Test çalışmasında Ankara andezit ile Afyon mermer olmak üzere iki çeşit kaya tipi kullanılmıştır. Ortalama mod I çatlak tokluğu 75 mm çaplı andezit ve mermer numunelerinde 2.58±0.34 MPa$\sqrt{m}$ ve 3.43±0.27 MPa$\sqrt{m}$ olarak ölçülmüştür. Mod I çatlak tokluğu her iki 100 mm çaplı örnekte andezit için 3.43±0.27 MPa$\sqrt{m}$ ve mermer için 3.04±0.70 MPa$\sqrt{m}$ 'dir.

Tokluk üzerindeki boyutsal etki, 75 mm ve 100 mm olan iki ayrı çaptaki andezit ile mermer karot numunelerini kullanarak incelenmiştir. Andezit için boyutsal etki 75 mm ve 100 mm çaplarda yüzde otuz civarında (3.34/2.58=1.29) görülmüştür.

Anahtar Kelimeler: kaya kırılma testi, mod I çatlak tokluğu, düzleştirilmiş Brazilyan disk yöntemi, kırılmaya ilişkin sayısal modelleme

ACKNOWLEDGEMENTS

TABLE OF CONTENTS

LIST OF TABLES

LIST OF FIGURES

FIGURES

xvii

xviii

LISTS OF SYMBOLS AND ABBREVIATIONS

2D: two-dimensional

3D: three-dimensional

a: half of crack length

A: mesh size

A: andesite

BDT : Brazilian disc

CB : chevron bend

CCNBD : cracked chevron notched Brazilian disc

CPD: crack propagation direction

CPE8: continuum plane strain eight noded element

CSTBD : cracked straight through Brazilian disc

D: disc diameter

d_e : distance of crack tip to central load application point

$dofs$: degrees-of-freedom

E : Elastic Modulus

FBD : flattened Brazilian disc

G : energy release rate

G_c : critical energy release rate

ISRM : International Society for Rock Mechanics

J: J integral

K: stress intensity factor

K_I: mode I stress intensity factor (opening mode)

K_{II}: mode II stress intensity factor (shearing mode)

K_{III}: mode III stress intensity factor (tearing mode)

K_{IC} : mode I fracture toughness

K_{IIC} : mode II fracture toughness

L: half of flattened length

LEFM: linear elastic fracture mechanics

LVDT: linear variable differential transformer

M: marble

MTS: maximum tangential stress

P: applied concentrated load

P_{max}: failure load

P_{min}: minimum local load

R: disc radius

r_c: radius of contour integral region

RP: reference point

S_{11} : normal stress in x-direction

S_{22} : normal stress in y-direction

S_{33} : normal stress in z-direction

S_{12} : shear stress in xy-direction

S: span length

SCB : semi-circular bending

SIF: stress intensity factor

SNDB : straight-notched disc bending

SR: short-rod

t: disc thickness

UCS : Uniaxial Compressive Strength

Y : dimensionless stress intensity factor

Y_I : mode I dimensionless stress intensity factor

Y_{II} : mode II dimensionless stress intensity factor

Y_{Imax} : maximum dimensionless stress intensity factor

w : projected width over loaded section

α: half of loading angle

ε : Strain

σ : stress

σ_1 : maximum principal stress

σ_3 : minimum principal stress

σ_t : tensile stress

α : a/R

τ : shear stress

μ: shear modulus

ϑ : Poisson's Ratio

θ : crack propagation angle

CHAPTER I

INTRODUCTION

In nature, the rocks contain different size cracks changing from microscale to macroscale and the cracks or flaws can exist in distinct shapes. These defects cause accumulation of infinite stress concentrations around the crack and is responsible for the stress transformation at the crack tip due to crack orientation. Thus, depending on the magnitude of stress, crack starts to form or propagate after failure, namely fracture happens. The science of rock fracture mechanics is primarily interested in fracture behavior during loading and fracture toughness, which is an expression of crack resistance to propagation of the crack. In development of fracture mechanics, supplementary fields of mechanics are benefitted to settle important relations between fracture and failure of the rock. These areas are summarized as continuum mechanics, solid mechanics, the elasticity and plasticity theories.

In classical mechanics, the materials are assumed to be flawless or without any cracks. However, fracture mechanics focuses on the material having cracks or defects. With regard to this, Inglis (1913) initially presented his mathematical solution involved with a elliptical hole defined in a plate by holding the linear elastic material assumption. This was concerned about high stress concentrations around elliptical cracks and ever yielding material condition. Then, Griffith's earliest work (1921) defined stress intensity factor as

a large amount of stress gathered at the crack tip compared to the rest of material by using Inglis' view about stress concentration. Advancing from this step, Griffith put forward that an increase in the potential energy is spent to the formation of new crack surfaces. Thus, Griffith (1921) invented the relation between stress intensity factor, K and critical energy release rate, G_c. After the development of elastic solutions, Irwin (1948) modified the Griffith theory by showing the plastic deformation in the metals. Later, Rice (1968) pioneered the field of the elastic plastic fracture mechanics by taking the plastic region concentrated around the crack tip into account using a simple mathematical theory.

1.1 Some fracture mechanics applications in the past

This part covers the important structures related to practice on the use of fracture mechanics in the past. Regarding this, the structures such as Liberty ships, aircrafts constructed during both World Wars provided many practical solutions against failures. Until World War II, rivets and bolts had been used as local crack arresters to prevent catastrophic failures. In World War II, weldment techniques began to be applied upon ships against fractures; however, 1031 damage or accidental events related to Liberty ships were recorded. This was caused by the ignorance and limited data about the fracture properties of welds. In the report about ship accidents (Kobayashi and Hisahiro, 1943), these brittle fractures in Liberty Ships occurred because high strength and ductile steels transformed into low strength and brittle steels at low temperature. Herein, low temperature caused the steel to show brittle-ductile transition property and so many ship accidents happened in wintertime. Besides this, low weldability of steel, low weld quality and poor design were responsible for them.

In the 1950s, another disaster was the first jetliner of the World named as Comet aircraft, which happened because of very small fatigue cracks beginning at the rivets surrounding the openings of window. These cracks were aroused from the square shape of window whose sharp corners caused greater stress concentration than curved or oval edges.

Moreover, repeated cabin pressure with the ups and downs provoked the metal to be fatigued (Shukla, 2005).

In the past, bridge collapses such as Point Pleasant Bridge disaster were experienced due to structural integrity. In this manner, the usage of only special material becomes inadequate, also tangled relations between materials, design, fabrication and loading conditions might raise fracture problems (Shukla, 2005).

The previous catastrophic events and investigations about them built up fracture mechanics knowledge applied in the fields of mechanical engineering, aerospace engineering, civil engineering, metallurgical engineering and mining engineering. From mining engineering perspective, the rock material and rock mass are with inherent cracks, discontinuities such as joints, voids etc. different from other disciplines.

1.2 The statement of the problem

Mode I fracture toughness is of interest in rock cutting, rock fragmentation, hydraulic fracturing. In underground mining applications, compressive loads are activated by the overburden stress. Stress concentrations due to the excavation-induced activities lead new crack surfaces to initiate.

For the measurement of rock fracture toughness, there are some methods recommended by ISRM and ASTM. The methods suggested by ISRM are chevron bend (CB), (Ouchterlony, 1988), short rod (SR), (Ouchterlony, 1988), cracked chevron notched Brazilian disc (CCNBD), (Fowell, 1995) and semi-circular bending (Kuruppu et al., 2015). Brazilian type methods with compressive loading on disc specimens include cracked chevron notched Brazilian disc (CCNBD), (Shetty et al., 1985), cracked straight through Brazilian disc (CSTBD), semi-circular bending test (SCB) (Chong and Kuruppu, 1984), Brazilian disc (BD) (Guo et al., 1993), flattened Brazilian disc (FBD) (Wang and Xing, 1999).

About the flattened Brazilian disc (FBD) testing method research outcomes like accurate stress intensity factors with tedious modeling work, testing procedure requirements, and reliable test results for a wide range of different rocks are limited. With recent improved fracture modeling and statistical processing techniques, it is possible to produce new expressions for stress intensity factors and fracture toughness measurement with FBD geometry.

1.3 The objective of the study

The major aim of this study is to measure the mode I fracture toughness values of the rocks in an improved and a more reliable way.

Although in previous studies, SIF solutions obtained from FBD related numerical models were profoundly investigated, there is still need for improvements. This study is designed to improve the quality of stress intensity factor computations by advanced numerical fracture modeling.

The second aim is to generate an improved parametric equation in order to compute stress intensity factor (SIF) in terms of the loading angle. Loading angle controls the width of the flat loading ends and thus the ideal specimen geometry to be used in testing.

Final goal is to check if selected rock types show a significant size effect as reported in the previous work by Bazant and Pfeiffer's (1987), Bazant and Kazemi, (1990), Bazant et al. (1991), Bazant et al. (1995, 1996) and Tutluoglu and Keles (2011). In recent literature survey, it is observed that there is a scant amount of researches interested in size effect issue of mode I fracture toughness measurements. This study aims at presenting extra findings and more explanations.

1.4 The methodology of the study

The first task is to create precise numerical models related to FBD specimen geometries with the same boundary conditions as in laboratory work. Testing work follows next on two rock types having different grain size and matrix.

In numerical work, according to input parameters obtained from mechanical properties of the rocks, FBD models are constructed by using ABAQUS v12. finite element program. Three major stages are the model generation, the mesh convergence study and the generation of the stress intensity factors (SIFs). Then, statistical processing of numerical modeling results yield expressions for estimating SIF in terms of loading angle and critical crack lengths of specimen geometries of various diameters.

Numerical models are generated under 2D plane strain condition to simplify the problem and save time. According to this, proper FBD geometries are constructed at each defined loading angle to catch convenient equations.

In experiments, two rock types namely andesite and marble are used in testing. These rocks are commonly used in the pavements, subway, wall lining, decoration etc. and are easily accessible. Ankara andesite is a pinkish-gray colored, fine grained, slightly weathered, massive, strong, igneous rock with some vesicles while Afyon marble is a beige-light gray colored, fine grained, fresh, strong metamorphic rock containing several micro fractures oriented in different directions. With the choice of these rocks, the variation in mode I fracture toughness results is assessed based on rock type.

In the experimental work, there exists three subdivisions containing the preparation of specimen, test set-up and size effect investigation. Firstly, specimen proper for FBD geometry with a specific loading angle is ready for testing and appropriate test procedure is applied by MTS 815 Rock Testing Machine in laboratory. In interpretation part, the consistency between past and present results are controlled and size effect is monitored according to current results.

Numerically computed critical crack lengths and experimentally measured critical crack lengths are compared to assess the quality of the modeling work to simulate real testing conditions.

Two fitting equations derived by Tutluoglu and Keles (2011) are used in experimental studies. There are some shortcomings of these equations. The drawbacks of the equations can be listed as low fit quality, wrong selection of parameters and narrower range of loading angle. Therefore, these equations can lead to controversial and misleading interpretations regarding site investigation and material design parameters. In this respect, an improved numerical equation is proposed. In order to monitor extensive fracture behavior of the material, the range of loading angle is relatively enlarged compared to the study investigated by Tutluoglu and Keles (2011).

1.5 Sign convention

This work is performed by means of ABAQUS finite element program utilized for analyzing the general engineering applications. During interpretation stage, the sign of mechanics used in ABAQUS program play an important role in the verification of the model. In the contrary to rock mechanics convention, stresses, strains and displacements having negative sign are interpreted as in compression whereas positive ones are in tension. Furthermore, ABAQUS program defines coordinates axes as the digits of *1, 2, 3* in three dimensional space corresponding to *x, y, z* axes in tensor notation. According to this, σ_{ij} is denoted by S_{ij} and S_{xx} gives the normal stress value along x-direction. Initial coordinate system referred to global reference system (*x, y, z*) is transformed into the local coordinate axes of *x', y', z'* located in ABAQUS visualization part. S_{11}' is expressed as the horizontal normal stress perpendicular to crack plane in this study while S_{22}' becomes the vertical normal stress parallel to crack plane.

The signs of stress intensity factors under mode I and mode II loadings (K_I and K_{II}) are interpreted differently from those of stresses. For instance, positive K_I value is obtained

as a result of the crack opening subjected to the tensile stresses which is interpreted as positive. Similarly, the sign of K_{II} value changes upon whether crack is opened or closed. Negative sign in K_{II} is induced by the negative shear stresses due to the closing of crack along crack line.

1.6 Outline of thesis

In Chapter 1, a brief introduction and some historical events about fracture mechanics are presented and in Chapter 2, rock fracture toughness tests suggested by ISRM and ASTM and former investigations about fracture toughness are discussed. In Chapter 3, numerical analysis related to various FBD geometries is presented to achieve mainly stress intensity factor equation. In Chapter 4, preliminary experimental studies and procedure applied upon FBD specimens are conducted to obtain reliable and consistent fracture toughness results. In Chapter 5, experimental results, discussion and comparison about FBD method and BD method's results are presented. Finally, conclusions and recommendations for FBD experiments, FBD and BD methods are given in Chapter 6.

CHAPTER 2

THEORETICAL BACKGROUND OF ROCK FRACTURE MECHANICS

Fracture mechanics is the science of the materials having cracks, defects and flaws. These irregularities may lead structural failures because of high stress concentrations at local points. To prevent these failures and expand focus of this area, many crack-based theoretical studies and definitions were presented until now. Here, some of them were provided.

2.1 Fracture modes

Irwin (1957) firstly described basic fracture modes with respect to loading conditions at the crack tip. In Figure 2.1, three independent movements along x, y, z directions defined in local Cartesian coordinate system are shown. They are expressed as mode I (pure tensile or opening mode), mode II (sliding mode) and mode III (tearing mode) which are respectively in plane and out of plane shear modes based on loading types. According to this, a crack can initiate and propagate in three principal modes (Rossmanith, 1983).
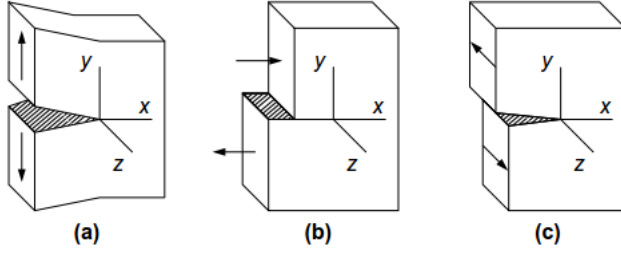
Figure 2. 1 The principal fracture modes with respect to loading type: (a) mode I (opening), (b) mode II (sliding), (c) mode III (tearing). (Chin Teh Sun and Zhihe Jin, 2012)

2.2 Linear elastic fracture mechanics (LEFM)

According to LEFM, the material is presumed to be homogenous, isotropic and linear elastic. More importantly, plastic zone surrounding crack tip is assumed to be very small for brittle rocks. Elastic Modulus (E) and Poisson's Ratio (ϑ) are elastic material properties. Related formulas including these constants are arranged based on elasticity theory.

2.2.1 Stress intensity factors

Irwin also defined the general term of stress intensity factor (SIF), K as a quantity measuring the stress field around the crack tip. The stress intensity factors of K_I, K_{II}, K_{III} were denoted for corresponding loading conditions. The formulas of K_I and K_{II} were given in Equation 2.1. According to them, K changes with crack length (a), far field stress (σ), dimensionless stress intensity factor (Y) depending on crack and specimen geometry.

$$K_I = Y_I \left(\frac{a}{W}\right) * \sigma\sqrt{\pi * a} \qquad K_{II} = Y_{II} \left(\frac{a}{W}\right) * \tau\sqrt{\pi * a}$$

$$(2.1)$$

Where;

K_I: mode I stress intensity factor

10

K_{II}: mode II stress intensity factor

σ = far field stress

τ = shear stress

a= crack length

$Y_I\left(\dfrac{a}{W}\right)$ = mode I dimensionless stress intensity factor

$Y_{II}\left(\dfrac{a}{W}\right)$ = mode II dimensionless stress intensity factor

W= width of the specimen

According to Irwin's criterion, when K_I arrives a critical value at which the material doesn't resist, material failure occurs due to the crack initiation and propagation. This critical stress intensity factor is named as fracture toughness, K_c. It is a material property presumed to be independent from size.

2.2.2 Crack tip stress and displacement solutions

Considering the elastic material assumption, Westergaard (1934) represented the stress and displacement solutions near the crack tip stated below. In Figure 2.2, a stress element is demonstrated. According to this, stress calculations were made in terms of r, the radial distance from crack tip and θ, angle. Stress at crack tip has a square root singularity, $1/\sqrt{r}$.
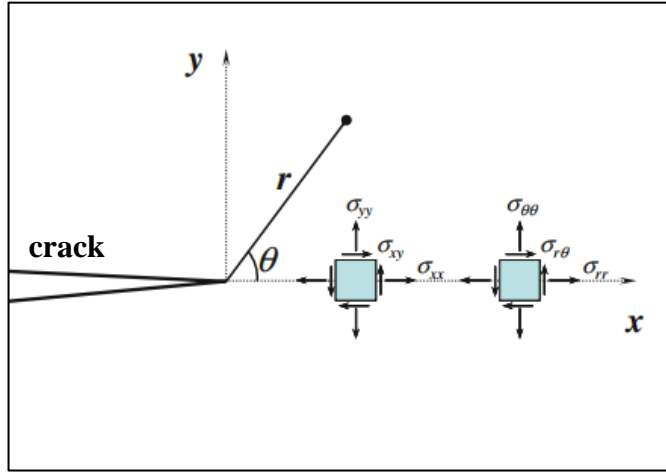
Figure 2. 2 Near crack tip stress configuration (Adapted from Ayatollahi MR, Akbardoost J., 2014)

Stress components near crack tip under mode I loading

$$\sigma_{xx} = \frac{K_I}{\sqrt{2\pi r}} \cos(\tfrac{\theta}{2}) \left[1 - \sin(\tfrac{\theta}{2})\sin(\tfrac{3\theta}{2})\right] \tag{2.2}$$

$$\sigma_{yy} = \frac{K_I}{\sqrt{2\pi r}} \cos(\tfrac{\theta}{2}) \left[1 + \sin(\tfrac{\theta}{2})\sin(\tfrac{3\theta}{2})\right] \tag{2.3}$$

$$\tau_{xy} = \frac{K_I}{\sqrt{2\pi r}} \cos(\tfrac{\theta}{2}) \sin(\tfrac{\theta}{2}) \tag{2.4}$$

$$\sigma_{zz} = 0 \text{ for plane stress} \tag{2.5}$$

$$\sigma_{zz} = \vartheta * \left(\sigma_{xx} + \sigma_{yy}\right) \text{ for plane strain} \tag{2.6}$$

$$\tau_{xz} = 0 \quad \tau_{yz} = 0 \tag{2.7}$$

Displacement components near crack tip under mode I loading

$$u_x = \frac{K_I}{2\mu}\sqrt{\frac{r}{2\pi}}\,\cos(\frac{\theta}{2})[\kappa - 1 + 2sin^2(\theta/2)]$$

(2.8)

$$u_y = \frac{K_I}{2\mu}\sqrt{\frac{r}{2\pi}}\,\sin(\frac{\theta}{2})[\kappa + 1 - 2cos^2(\theta/2)]$$

(2.9)

$$u_z = 0$$ (2.10)

$$\kappa = \frac{3-\vartheta}{1+\vartheta} \quad \text{for plane stress}$$ (2.11)

$$\kappa = 3 - 4\vartheta \quad \text{for plane strain}$$ (2.12)

Stress components near crack tip under mode II loading

$$\sigma_{xx} = -\frac{K_{II}}{\sqrt{2\pi r}}\sin(\frac{\theta}{2})\left[2 + \cos(\frac{\theta}{2})\cos(\frac{3\theta}{2})\right]$$

(2.13)

$$\sigma_{yy} = \frac{K_{II}}{\sqrt{2\pi r}}\sin(\frac{\theta}{2})\cos(\frac{\theta}{2})\cos(\frac{3\theta}{2})$$

(2.14)

$$\tau_{xy} = \frac{K_{II}}{\sqrt{2\pi r}}\left[1 - \sin(\frac{\theta}{2})\sin(\frac{3\theta}{2})\right]$$

(2.15)

$$\sigma_{zz} = 0 \text{ for plane stress} \tag{2.16}$$

$$\sigma_{zz} = \vartheta * (\sigma_{xx} + \sigma_{yy}) \text{ for plane strain} \tag{2.17}$$

$$\tau_{xz} = 0 \ \ \tau_{yz} = 0 \tag{2.18}$$

Displacement components near crack tip under mode II loading

$$u_x = \frac{K_{II}}{2\mu} \sqrt{\frac{r}{2\pi}} \ \sin(\frac{\theta}{2})[\kappa + 1 + 2sin^2(\theta/2)]$$

$$\tag{2.19}$$

$$u_y = \frac{K_{II}}{2\mu} \sqrt{\frac{r}{2\pi}} \ \cos(\frac{\theta}{2})[\kappa - 1 - 2sin^2(\theta/2)]$$

$$\tag{2.20}$$

$$u_z = 0 \tag{2.21}$$

$$\kappa = \frac{3-\vartheta}{1+\vartheta} \ \ \text{for plane stress} \tag{2.22}$$

$$\kappa = 3 - 4\vartheta \ \ \text{for plane strain} \tag{2.23}$$

2.3 Elastic plastic fracture mechanics (EPFM)

Plastic deformation occurs as stress applied surpasses the strength of the material. In some materials like ductile steels, plastic region around the crack tip is not negligibly small and LEFM approach is not applicable for them. Instead of it, elastic plastic fracture mechanics formulas are used for ductile materials. According to EPFM, the material is assumed to be elasto-plastic and isotropic. Here, *J* integral concept is explained as an EPFM criteria.

2.3.1 Path Independent *J* integral

A path independent contour integral denoted as J was discovered by Rice (1968). J integral was used for calculating energy required for creating new crack surfaces. The contour integral theory can be employed for both LEFM and EPFM approaches. In Figure 2.3, the contour surrounding crack tip is depicted through Cartesian coordinates of *x*, *y*.
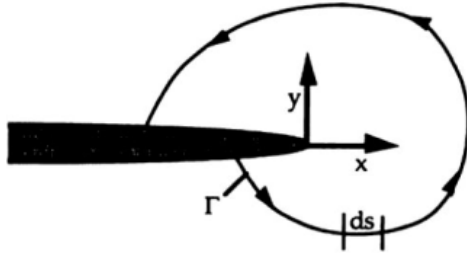
Figure 2. 3 Arbitrary contour around the crack tip

J integral formula is denoted by the Equation 2.24.

$$J = \int_{\Gamma} \left(W \, dy - T * \frac{\partial u}{\partial x} \, ds \right) \tag{2.24}$$

Where;

Γ: arbitrary contour around the crack tip beginning from lower flat notch surface up to upper notch surface in a counterclockwise direction

15

W: strain energy density

$$W = W(x,y) = \int_\Gamma \sigma_{ij} * d\varepsilon_{ij}$$

T_i: components of traction vector based on outward normal along Γ.

T_i: $\sigma_{ij} * n_j$

σ_{ij} : stress tensor

ε_{ij} : strain tensor

u_i: the components of displacement vector

n_j: components of unit outward vector normal to contour defined as Γ

ds: differential arc length of contour Γ

In next section, mode I fracture toughness testing background with different specimen geometries and testing methods is summarized. The specimens used for testing are divided into three types of geometry which are bending, Brazilian disc and pre-cracked Brazilian disc.

2.4 Fracture testing with bending type specimens

Bending tests are commonly used to inspect mode I failure of brittle rocks. For three-point and symmetric four-point bending tests, rectangular beams are used while for semi-circular disc and straight notch disc bending tests, either disc or half disc shaped geometries are necessary. Semi-circular disc and straight-notched disc geometries are rather new geometries loaded by bending until fracturing. In all these specimens, an edge crack at lower boundary is constructed through the center of geometry with a wire saw.

For test set-up, two rollers as support points underneath the specimen are put at the same distance from the crack. Another roller is mounted to the upper center of the specimen.

2.4.1 Three-point bending test

Srawley (1976) proposed the mode I stress intensity factor solution with a polynomial expression in terms of crack length (*a*), width (*W*), span length (*S*), applied concentrated load (*P*). As he stated, this solution is used for many purposes including fatigue crack growth due to broad range of *a/W* ratio from 0 and 1. However, according to ASTM E399 standard, Srawley noted that *a/W* ratio should be within the range of 0.45 and 0.55 to measure more reliable and accurate mode I stress intensity factors. Besides this restriction, this solution becomes valid for the condition of *S/W*=4.

Srawley stated this formula as below

$$\frac{K_I B \sqrt{W} \cdot}{P} = \frac{3 * (\frac{S}{W})\sqrt{a}\,(1.99 - \frac{a}{W}(1 - \frac{a}{W})(2.15 - 3.93.\frac{a}{W} + 2.7\left(\frac{a}{W}\right)^2))}{2\left(1 + 2\frac{a}{W}\right)(1 - \frac{a}{W})^{3/2}}$$

$$(2.25)$$

K_I: mode I stress intensity factor

P: applied concentrated load

Y_I *(a/W)*: mode I dimensionless stress intensity factor

B: thickness of test specimen

W: depth of test specimen

S: span length

a: crack length

a/W: dimensionless crack length

Tada et al. (2000) expressed Srawley's formula with another form.

17

$$K_I = Y_I(a/W) * \sigma * \sqrt{\pi * a}, \quad \sigma = \frac{6M.}{BW^2}, \quad M = \frac{P*S}{4}$$

(2.26)

for $\frac{a}{W} \leq 1$ and $\frac{S}{W} = 4$,

$$Y_I(a/W) = \frac{1.99 - \frac{a}{W}(1-\frac{a}{W})(2.15 - 3.93.\frac{a}{W} + 2.7(\frac{a}{W})^2)}{\sqrt{\pi} \left(1 + 2\frac{a}{W}\right)(1-\frac{a}{W})^{3/2}}$$

(2.27)

$$K_I = \frac{3*P*S}{2*B*W^2} * Y_I\left(\frac{a}{W}\right) * \sqrt{\pi * a}$$

(2.28)

Where;

M: moment

σ: tensile stress

2.4.2 Symmetric four-point bending test

According to ASTM C 1421-16 (2001), four-point bending fixture for fracture test is given under suggested test fixture procedures in the Annex −A1 as seen in Figure 2.4. Stress intensity factor solution (K_I) proposed by ASTM C 1421 (2001) for four-point bending model is presented below. This formula is valid within the range of 0.35 $\leq a/W \leq 0.6$. Moreover, according to ASTM C 1421-16 (2001), outer span length to inner span length ratio (S_O/S_I) must be ideally taken as 2.

18
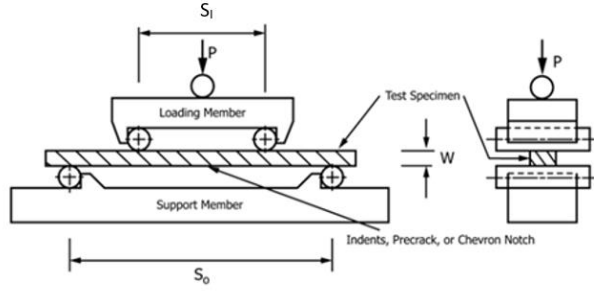
Figure 2. 4 View of four-point bending test set-up

$$K_{IPB} = Y_I * \frac{P*(S_O - S_I)}{B*W^{3/2}} * \frac{3*(\frac{a}{W})^{1/2}}{2*(1-(\frac{a}{W}))^{3/2}}$$

(2.29)

$$Y_I = Y_I\left(\frac{a}{W}\right) = 1.9887 - 1.326 * \left(\frac{a}{W}\right) - \frac{\left(3.49 - 0.68*\left(\frac{a}{W}\right) + 1.35*\left(\frac{a}{W}\right)^2\right)*\left(\frac{a}{W}\right)*(1-\left(\frac{a}{W}\right))}{(1+(\frac{a}{W}))^2}$$

(2.30)

Here,

K_{IPB}: mode I stress intensity factor under four-point bending test

P: applied concentrated load

B: thickness of test specimen

W: depth of test specimen

S_O: outer span length of test specimen

S_I: inner span length of test specimen

a/W: dimensionless crack length

Y_I: mode I dimensionless stress intensity factor

2.4.3 Semi-circular bending test

Semi-circular bending (SCB) method, namely Straight notched semi-circular bending method was suggested by Chong and Kuruppu in 1984. Both load line displacement (Chong and Kuruppu, 1984) and fracture toughness computations (Chong et al., 1987) were provided. They performed finite element analysis for limited range of crack lengths and span lengths. Lim et al. (1993) conducted an extensive numerical analysis for a broad range of crack length, span length and mixed-mode stress intensity factors.

As seen in Figure 2.5, the SCB specimen is subjected to three-point bending loading. SCB disc contains a straight edge notch. It can be machined with a chevron notch instead of straight notch because of the easiness in machining and high stress concentration causing stable crack growth and less fracture process zone (FPZ), (Ayatollahi, 2013).
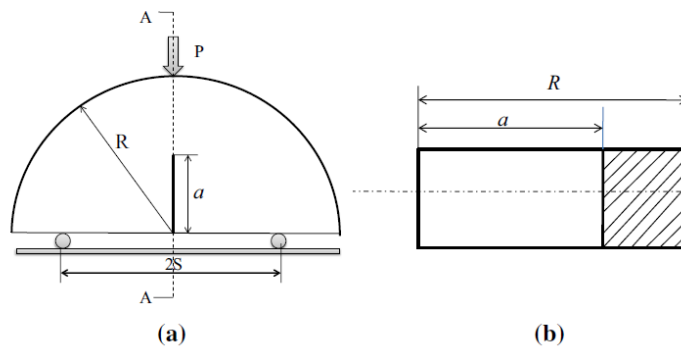
Figure 2. 5 Three-point loading (a) and crack line (b) configuration of semi-circular specimen (Adapted from Ayatollahi et al., 2016)

The SCB method is recommended due to simplicity in preparation of specimen, laboratory set-up, test procedure, only applicability to wide range of rocks, less machining and small size amount of material requirement, (Lim et al., 1994). Moreover, it is proper

for mixed mode, mode I and mode II loading modes. Mode I fracture toughness value can be computed by using the formula in Equation 2.31 (Kuruppu et al., 2015).

$$K_I = \frac{P * \sqrt{\pi a}}{2RB} \ Y_I \ (\frac{a}{R}, \frac{S}{R})$$ (2.31)

Where;

K_I : mode I stress intensity factor

P: applied concentrated load

a: crack length

R: radius of test specimen

B: thickness of test specimen

S: half of span length

Y_I : dimensionless stress intensity factor based on *a/R* and *S/R* (Lim et al., 1994)

a/R: dimensionless crack length

Y_I is given in Equation 2.32 by Lim et al. (1994) below. This formula is valid for $0.1 \leq$ *a/R* ≤ 0.8 and *S/R*=0.8.

$$Y_I = \frac{S}{R} \ (2.91 + 54.39(\frac{a}{R}) - 391.4(\frac{a}{R})^2 + 1210.6(\frac{a}{R})^3 - 1650(\frac{a}{R})^4 + 875.9(\frac{a}{R})^5)$$

(2.32)

Lim et al. (1993) studied the influences of *a*, *S*, θ over SIF evaluation of SCB geometry using the numerical models. In this work, SCB geometry with dimensionless span length varying between 0.5 and 0.8 and dimensionless crack length varying between 0.1 and 0.8 was used. Considering these limits, when half of span length (*S*) to radius ratio decreases, pure mode II SIF becomes dominant. Likewise, Y_I reduces with K_{IC} when the parameters of *a* and θ increase. In addition, numerical results show that shorter crack lengths are preferred because of less variation in K_{IC} values than longer crack lengths.

In Funatsu et al.'s study (2015), Kimachi sandstone located in Japan was tested under three- point loading. These semi-circular specimens with a straight crack had 100 mm diameter and 25 mm thickness. By using diamond saw with the thickness of 0.3 mm, a/R ratio were adjusted for the cases of 0.3, 0.4, 0.5 and span length to radius ratio of 0.8 was kept constant in each specimen.

In Wei et al.'s experiments (2015), test specimens including five granites and five sandstones were tested for S/R =0.8. They were 30 mm in thickness and 36.5 mm in radius. The range of a/R ratio was kept between 0.36 and 0.4 and at S$/R$=0.8. Related mode I fracture toughness values were listed in Table 2.1.

Table 2. 1 Mode I fracture toughness values with SCB testing method

Material Type	K_{IC} (MPa$\sqrt{m}$)	Source
Dazhou Sandstone	0.56	Wei et al. (2015)
Qingdao Granite	0.87	Wei et al. (2015)
Granite	0.68	Chang et al. (2002)
Marble	0.87	Chang et al. (2002)
Limestone	0.68	Khan and Al-Shayea (2000)
Ankara Andesite	0.94	Tutluoglu and Keles (2011)
Johnstone (synthetic mudstone)	0.06	Lim et al. (1994)
Sandstone	0.27	Singh and Sun, 1990

2.4.4 Straight notched disc bending test

Straight notched disc bending (SNDB) method was initially proposed by Tutluoglu and Keles (2011) to measure mode I fracture toughness value of rock materials and concrete, etc. SNDB specimen has a circular plate type geometry with a straight notch subjected to three-point bending loads as seen in Figure 2.6.

This method presents many advantages such as easy specimen preparation, simple test procedure, smaller fracture process zone (FPZ) size, and thickness-based variable stiffness which is an advantage in specimen size effect investigations.
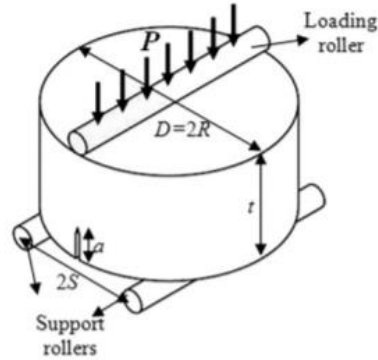
Figure 2. 6 Straight notched disc bending (SNDB) specimen geometry under three-point loading

Tutluoglu and Keles (2011) computed dimensionless stress intensity factors and measured fracture toughness with SNDB method. They were estimated by changing significant geometrical parameters containing dimensionless crack length (*a/t*), dimensionless thickness (*t/R)*, dimensionless span length (*S/R*).

Mode I dimensionless stress intensity factor was represented by the Equation 2.33.

$$Y_I = \frac{K_I}{\sigma_0 \sqrt{\pi a}} \quad \text{and} \quad \sigma_0 = \frac{P}{2Dt} \tag{2.33}$$

Where;

K_I : mode I stress intensity factor

P: applied concentrated load

a: crack length

R: radius of test specimen

t: thickness of test specimen

S: half of span length

σ_0 : tensile stress

Y_I: mode I dimensionless stress intensity factor based on a/t, S/R and t/R

Tutluoglu and Keles (2011) proposed two parametric equations for computation of mode I stress intensity factors for the specimens within the ranges of $0.1 \leq a/t \leq 0.9$, $0.5 \leq t/R \leq 3$ and $0.5 \leq S/R \leq 0.8$.

The linear form of mode I dimensionless stress intensity factor equation strongly depends on S/R ratio. Parameters m and n in the equation are functions of a/t and t/R ratios.

$$Y_I = m\left(\frac{S}{R}\right) + n \qquad (2.34)$$

$$Y_I = C_1\left(\frac{t}{R}\right)^5 + C_2\left(\frac{t}{R}\right)^4 + C_3\left(\frac{t}{R}\right)^3 + C_4\left(\frac{t}{R}\right)^2 + C_5\left(\frac{t}{R}\right) + C_6$$

$$(2.35)$$

Second formula composed of fifth order polynomial function with coefficients was offered for various t/R ratios. It was found that the increase in disc thickness results in higher mode I fracture toughness values.

2.5 Brazilian disc test background

In early 1940s, Akazawa (1943) and Carneiro (1943) proposed Brazilian disc test (BDT), namely split-tension test to measure tensile strength of brittle rocks and concrete. Carneiro worked on a correlation between the uniaxial compressive strength and tensile strength (σ_t). In 1978, ISRM suggested a tensile strength measurement method with a testing configuration formed by inserting two opposite curved jaws for loading cores under compression as seen in Figure 2.7.
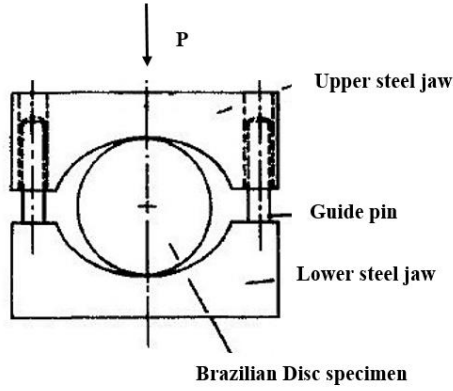
Figure 2. 7 Indirect tensile strength test configuration of Brazilian disc (Improved illustration from ISRM, 1978)

$$\sigma_t = \frac{P}{\pi * R * t} \tag{2.36}$$

Where;

P: failure load

R: disc radius

t: disc thickness

2.5.1 Stress distribution induced by a point load and uniform arc loading

Prior to use of loading device suggested by ISRM (1978), some loading alternatives were evaluated for tensile strength measurement. As seen in Figure 2.8, compressive loading was applied by a concentrated load, P at the upper and lower part of thin circular disc specimen to measure the tensile strength based on the tension generated indirectly at the center of the disc. Related to stress distribution, vertical normal stress, horizontal normal stress and shear stress in Cartesian coordinates are expressed by the symbols of σ_{yy}, σ_{xx}, σ_{xy}, respectively.

According to Timoshenko's theory (1970), there is a linear contact at initial stage of diametric compression test and at the loading point, this causes compressive stress go to infinity along vertical line. On the other hand, based on Hondros' approach (1959), when time elapses, load ascends and linear contact converts into slightly flat contact area with load increase. Although both theories give identical results, slightly flat surface is deformed by increasing load. This means that in extreme points along vertical line, compressive stress is not infinite (Álvarez Fernández et al., 2015).
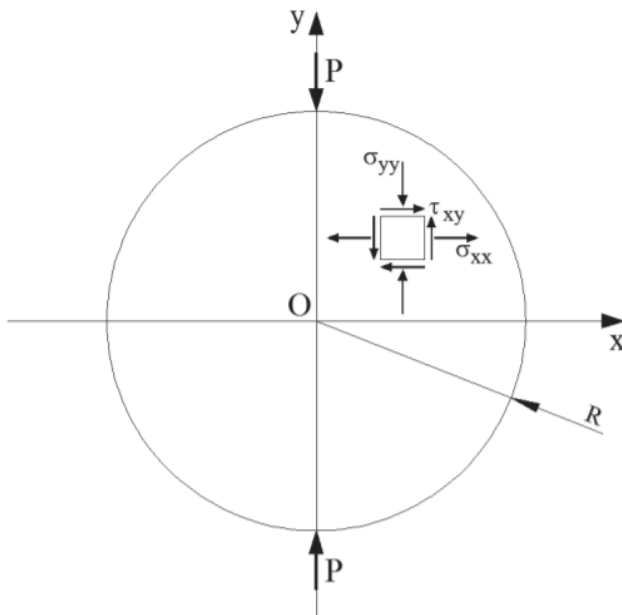
Figure 2. 8 Brazilian disc subjected to concentrated load at upper and lower ends (Álvarez Fernández et al., 2015)

Based on elastic solution, stress distribution at the center $r/R=0$ of the disc were given by Hondros (1959). Maximum tensile stress was reported to be at the center perpendicular to the compressive loading direction; this is where tensile failure occurs. The solution included an angle of 2α and p for circular distribution of concentrated loading at the

26

loaded ends. This was necessary in order to eliminate the effect of crushing problem under the concentrated loading in testing practice (Figure 2.9).
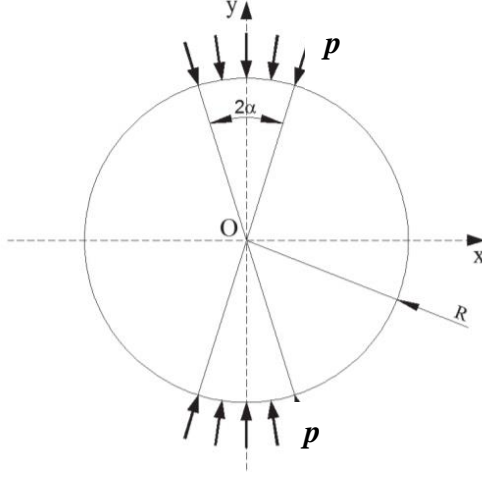
Figure 2. 9 Radially distributed compressive load at loaded ends (Álvarez Fernández et al., 2015).

For the load distribution adjusted geometry, stress distribution transformed into polar coordinates (r, θ) is given by:

$$\sigma_\theta = \frac{P}{\pi R t \alpha} * \left(\frac{(1 - \left(\frac{r}{R}\right)^2) sin2\alpha}{1 - 2\left(\frac{r}{R}\right)^2 cos2\alpha + \left(\frac{r}{R}\right)^4} - arctan(\frac{(1 + \left(\frac{r}{R}\right)^2)}{(1 - \left(\frac{r}{R}\right)^2)} * tan\alpha) \right)$$

(2.37)

$$\sigma_r = - \frac{P}{\pi R t \alpha} * \left(\frac{(1 - \left(\frac{r}{R}\right)^2) sin2\alpha}{1 - 2\left(\frac{r}{R}\right)^2 cos2\alpha + \left(\frac{r}{R}\right)^4} + arctan(\frac{(1 + \left(\frac{r}{R}\right)^2)}{(1 - \left(\frac{r}{R}\right)^2)} * tan\alpha) \right)$$

(2.38)

$$\sigma_\theta = \frac{P}{\pi Rt}\left(\frac{sin2\alpha}{\alpha} - 1\right) \tag{2.39}$$

$$\sigma_r = -\frac{P}{\pi Rt}\left(\frac{sin2\alpha}{\alpha} + 1\right) \tag{2.40}$$

$$p\text{:} \quad \frac{P}{w*t} \tag{2.41}$$

Where;

P: applied concentrated load

p: applied pressure

R: disc radius

t: disc thickness

w: projected width over loaded section

2α: loading angle in degrees

r: radial distance from the center of the disc

θ: angular displacement of a point from the center of the disc

σ_r: radial normal stress

σ_θ: tangential normal stress

Herein, the pressure along projected width which is flat surface was calculated using the parameter of w equal to $Dsin\alpha$ and tangential stress along loaded vertical line was found as $\frac{P}{\pi Rt}$ at the center.

According to these expressions, when half of loading angle approaches to zero, it is found that σ_θ, tangential stress and σ_r, radial stress at the center are found equal to $\frac{P}{\pi Rt}$ and $\frac{-3P}{\pi Rt}$, respectively. In other scenario including half of loading angle tending towards infinity,

28

both of them become $-\frac{P}{\pi R t}$. Coming to another case, while R and t tend to zero, separately, stress becomes zero. For this condition, t/R ratio was taken as 1 to be able to negotiate with the plane strain assumption and simplify the equation by removing the uncertainty about the parameters in the calculation.

After Hondros' (1959) stress solutions, Cauwellaert (1994) derived the approximation displacement formula for the Brazilian disc by applying opposite uniform radial loads over arc length of disc. The idea lying behind this loading is the stress transformation over arc lengths.

Wang et al. (2004) adapted the same formula for flattened Brazilian disc specimen by considering flat ends instead of opposite circular arc lengths and rearranged closed form stress solution of Brazilian disc (BD) by adding $P\cos\theta$ instead of P as seen in Figure 2.10.
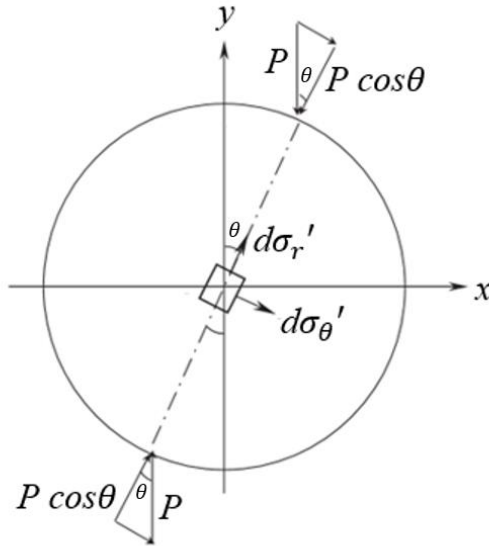
Figure 2. 10 Differential stress and force components in polar coordinates

Where;

$$d\sigma_\theta' = \frac{P\cos\theta}{\pi R} \tag{2.42}$$

29

$$d\sigma_r{}' = \frac{-3P\cos\theta}{\pi R} \tag{2.43}$$

2.5.2 Crack initiation conditions for FBD and BDT methods

The stress distribution changing with disc geometry induces failure conditions to alternate. According to Griffith strength criterion (1924), crack initiation conditions were given based on specimen geometry associated with test type as below.

$$\text{If } 3\sigma_1 + \sigma_3 \geq 0 \ , \ \sigma_1 = \sigma_t \tag{2.44}$$

$$\text{If } 3\sigma_1 + \sigma_3 < 0 \ , \ \sigma_t = \frac{(\sigma_1 - \sigma_3)^2}{-8(\sigma_1 + \sigma_3)} \tag{2.45}$$

When in Brazilian disc method, equalities of $3\sigma_1 + \sigma_3 = 0$ and $\sigma_1 = \sigma_t$ are achieved at the center of the disc, tensile crack initiates at the disc center. In other words, rock fails at which tensile stress surpasses the tensile strength of rock.

On the other hand, in Flattened Brazilian disc method, as the conditions of $3\sigma_1 + \sigma_3 < 0$ and $\sigma_t = \frac{(\sigma_1 - \sigma_3)^2}{-8(\sigma_1 + \sigma_3)}$ are satisfied at the center of the disc, tensile crack initiates from the center.

2.6 Fracture toughness testing with flattened Brazilian disc test method

Guo et al. (1993) suggested a mode I fracture toughness-testing method based on Brazilian tensile strength testing specimen geometry. With this method, mode I fracture toughness (K_{IC}) can be measured without machining a notch or crack.

Guo et al. (1993) studied the relations between SIF parameters and defined a formula between Y_I, dimensionless stress intensity factor and a/R, dimensionless crack length using a numerical integration method. The numerical solution indicated that dimensionless stress intensity factor was a function of dimensionless crack length.

Guo et al. (1993) changed the loading angles from 5° to 50° to display how dimensionless stress intensity factor behaves at different crack lengths. According to this, the dimensionless stress intensity factor decreases due to expansion of contact area when loading angle increases. This causes tensile region narrowing and reducing fracture toughness.

After numerical interpretations, mode I fracture toughness formula for BDT was derived as below (Guo et al., 1993).

$$K_{IC} = B * P_{min} * Y_I\left(\frac{a}{R}\right) \tag{2.46}$$

Where;

K_{IC}: mode I fracture toughness (MPa$\sqrt{m}$)

B: the constant dependent on geometry of the specimen

B:$\dfrac{2}{\sqrt{R}*t*\alpha*\pi\sqrt{\pi}}$

P_{min}: local minimum load

D: disc diameter

R: disc radius

t: disc thickness

$Y_I\left(\frac{a}{R}\right)$: dimensionless stress intensity factor

a: half of crack length

α: half of loading angle (in radians)

a/R: dimensionless crack length

31

σ_r: radial normal stress

σ_θ: tangential normal stress

In Guo et al.'s method (1993), there were a number of discrepancies such as: it did not guarantee crack initiation at the center and crack propagation along vertical axis of diameter and did not explain how loading angle controls where the crack initiates (Wang and Xing, 1999). Uniform arc loading presumed in the calculations was difficult to practice and wrong selection of domain led to inconsistent SIF results for center cracked problems.

In pursuit of a better method, Wang et al. (2004) developed a Flattened Brazilian disc (FBD) method to overcome the shortcomings of Brazilian disc test (BDT) suggested by Guo et al. (1993). In Figure 2.11, the geometry proposed for this method was demonstrated and opposite curved surfaces with the same flattened end width (*2L*) are constructed to maintain easy loading and guarantee crack initiation at the disc center by discarding crushing problem at contact points.
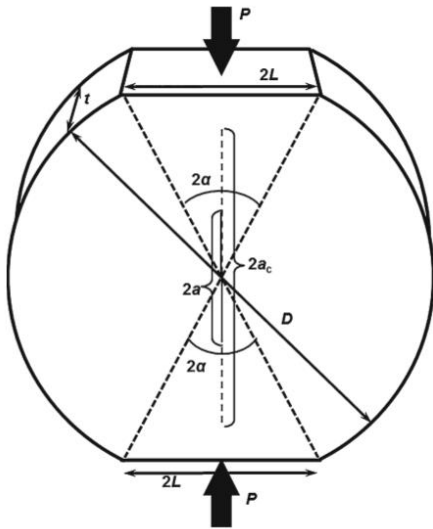
Figure 2. 11 The geometric representation of Flattened Brazilian disc (Keles and Tutluoglu, 2011)

Dashed line in Figure 2.11 shows where the crack formation occurs during loading.

Wang et al. (2004) derived a formula for mode I fracture toughness of FBD geometry as given in equation 2.47.

$$K_{IC} = \frac{Pmin * Y_{max}}{t * \sqrt{R}}$$ (2.47)

Where;

$K_{IC:}$ mode I fracture toughness (MPa$\sqrt{m}$)

P: applied concentrated load (N)

P_{min}: local minimum load (N)

Y_I: dimensionless stress intensity factor

Y_{IMAX} = maximum dimensionless stress intensity factor

R: disc radius (mm)

D: disc diameter (mm)

t: disc thickness (mm)

L: half of flattened end width (mm)

2α: loading angle in radians

a: half of crack length (mm)

a_c: half of critical crack length (mm)

a/R: dimensionless crack length

In Table 2.2, the results of fracture toughness tests applied by Guo et al. (1993) were given. In these tests, six specimens including sandstone, varied colored limestone,

different coarse-grained marbles were used to determine fracture toughness. In addition, chevron test suggested by ISRM and Guo et al.'s BDT results (1993) were found rather close to each other. To illustrate, K_{IC} values of sandstone, grey limestone subjected to chevron bend test resulted in 0.68 MPa$\sqrt{m}$, and 1.85 MPa$\sqrt{m}$, while corresponding values were obtained as 0.67 MPa$\sqrt{m}$ and 1.58 MPa$\sqrt{m}$ under Brazilian disc test.

Table 2. 2 Mode I fracture toughness values with FBD geometry

Material Type	K_{IC} (MPa$\sqrt{m}$)	Source
Sandstone	0.67±0.05	Guo et al. (1993)
White limestone	1.38±0.2	Guo et al. (1993)
Grey limestone	1.58±0.16	Guo et al. (1993)
Fine-grained marble	1.00±0.07	Guo et al. (1993)
Coarse-grained marble	1.12±0.19	Guo et al. (1993)
Basalt	3.01±0.49	Guo et al. (1993)
Chalk	1.15 ± 0.15	Proveti and Michot (2006)
Granite	1.29±0.16	Chang et al. (2002)
Marble	0.99±0.16	Chang et al. (2002)

A valid Brazilian type (FBD) mode I fracture test should have a central crack forming during the load application. Crack is supposed to be in line with the direction of applied boundary loading. Crack presumably propagates in a stable manner with a decrease in the applied concentrated load P and this part is associated with a negative slope of load-displacement plot. Load drop continues for a while. Then, with a positive slope, applied load shows an increase until disc is completely split into two halves. It must be ensured that cracking does not begin under the loading platens.

In experiments conducted by Wang and Xing (1999), the FBD methods were compared with CCNBD suggested by ISRM (Fowell, 1995). According to this, K_{IC} value of Chongqing limestone was found as 1.25 MPa$\sqrt{m}$ for FBD method whereas K_{IC} value of same rock type for CCNBD test was obtained as 1.26 MPa$\sqrt{m}$. It was seen that there was a close relationship between the results of both test types. In extensive study of Tutluoglu and Keles (2011), FBD fracture toughness results were found as 1.40 MPa$\sqrt{m}$ for andesite and 1.12 MPa$\sqrt{m}$ for marble while K_{IC} value of andesite was 1.45 MPa$\sqrt{m}$ for CCNBD tests.

Wang and Xing (1999) made efforts to determine the range of optimum loading angle by applying a boundary element method. Wang and Xing found that the loading angle of 2α required to initiate crack at the center should be greater than 19.5°. Later, Wang and Wu (2004) computed this critical loading angle (2α) as 20° by using finite element method and in Kaklis et al.'s finite element models (2005), this angle was calculated as 15°. Optimum loading angle for mode I fracture toughness was found within the range of 20° and 30° (Huang et al., 2014 and Wang et al., 2004).

In stress analysis conducted by Keles and Tutluoglu (2011), while loading angle of 10° and 12° less than 14° gave normalized equivalent stress higher than 1, the angle more than 14° resulted in smaller than 1. These results emphasize that the crack initiation occurs out of disc center for the angle lower than 14°. According to these findings, too small flattened length is expected to yield unreliable fracture toughness result.

2.7 Fracture toughness testing with cracked Brazilian disc geometry

Tension failure of cracked Brazilian disc type specimens under compressive loading is induced at the tip of central crack. Then, the crack propagates along diametric line parallel to loading direction to initiate mode I failure.

For initial crack, a wire saw is used for central cracks inside disc. The shape, direction, location, sharpness and machining of the crack influence stress concentration developed from the crack tip. Although pre-cracking stage is a critical and demanding operation, these cracked methods are preferred due to simpler test set-up and specimen preparation, compared to those of CB (chevron bend) test and SR (short rod) tests.

2.7.1 Cracked straight through Brazilian disc (CSTBD) test

The cracked straight through Brazilian disc (CSTBD) is a circular specimen containing a central crack subjected to compressive loading to determine mode I, mode II and mixed mode fracture toughness of rocks. Firstly, Libatskii and S.E.Kovchik (1967) developed an analytical solution for CSTBD geometry to investigate the mode I fracture toughness. Secondly, Awaji and Sato (1978) used this specimen to indicate mode I, mode II and mixed mode fracture toughness of graphite, plaster and marble. Later, Atkinson et al. (1982) derived the SIF solutions for Brazilian disc with a straight through crack (STC) aligned at any direction. This method enables different modes of loading on the same test conditions by changing the direction of crack inclination angle.

As illustrated in Figure 2.12, inside a Brazilian disc, a straight through crack is opened from the center by a means of drill bit and wire saw based on crack orientation. This pre-cracked specimen is compressively loaded along its core diameter using the platens.
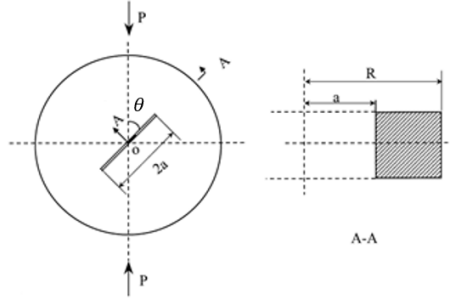
Figure 2. 12 Brazilian disc with a straight through crack (STC) with crack inclination angle

Mode I and mode II stress intensity factors for CSTBD specimens containing both inclined cracks and straight through cracks (STC) were determined by using these equations proposed by Atkinson et al. (1982) as below.

$$K_I = \frac{P\sqrt{a}}{RB\sqrt{\pi}}Y_I \qquad (2.48)$$

$$K_{II} = \frac{P\sqrt{a}}{RB\sqrt{\pi}}Y_{II} \qquad (2.49)$$

Where;

K_I : mode I stress intensity factor

K_{II}: mode II stress intensity factor

P: applied concentrated load (N)

R: disc radius (mm)

B: disc thickness (mm)

$2a$: crack length (mm)

θ : crack inclination angle

α : dimensionless crack length

Y_I: mode I dimensionless stress intensity factor

Y_{II}: mode II dimensionless stress intensity factor

The dimensionless stress intensity factor equations based on α and θ presented below are valid for the condition of $a/R \leq 0.3$. According to this, more reliable fracture toughness results were obtained from Atkinson's experiments upon PMMA specimens at short crack lengths. Also, Krishnan et al. (1998) studied upon crack inclination angle to obtain pure Y_{II} and found it as 29° at $a/R=0.145$ when $Y_I=0$.

$$Y_I: 1 - 4sin^2\theta + 4sin^2\theta(1 - 4cos^2\theta)(\frac{a}{R})^2$$

(2.50)

$$Y_{II}: \left(2 + (8cos^2\theta - 5)\left(\frac{a}{R}\right)^2\right)sin2\theta$$

(2.51)

Fowell and Xu (1993) provided the Y_I solution (Equation 2.52) with a best-fit polynomial function valid for the wide range of $0.05 \leq a/R \leq 0.95$.

$$Y_I: \sqrt{\frac{\pi}{\alpha}}(0.0354 + 2.0394\alpha - 7.0356\alpha^2 + 12.1854\alpha^3 + 8.4111\alpha^4 - 30.7418\alpha^5 -$$
$$29.4959\alpha^6 + 62.9739\alpha^7 + 66.5439\alpha^8 - 82.1339\alpha^9 - 73.6742\alpha^{10} +$$
$$73.8466\alpha^{11})$$

(2.52)

2.7.2 Cracked chevron notched Brazilian disc (CCNBD) test

Shetty et al. (1985) developed a new method called as cracked chevron notched Brazilian disc method (CCNBD) and applied it to determine fracture toughness of three ceramics by adapting SIF's solutions of CSTBD specimen to chevron notched discs. In 1995, ISRM recommended CCNBD specimen as an ideal specimen for fracture toughness measurements under mode I, mode II and mixed mode loadings. Advantages of the proposed test are higher failure loads, larger tolerance against machining error, easier test procedure and less variation in results due to the notch type (ISRM, 1995).

Geometry of CCNBD specimen depicted in Figure 2.13 is transformed into dimensionless parameters represented as below.
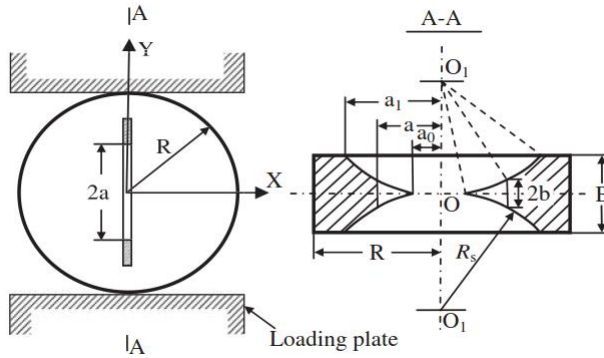
Figure 2. 13 CCNBD specimen and test configuration (Fowell et al., 2006)

Where;

$$\alpha_0 = a_0/R$$

$$\alpha_1 = a_1/R$$

$$\alpha_B = B/R$$

$$\alpha_s = D_s/D$$

39

Restrictions related to geometric parameters of CCNBD test and valid range for α_0, α_1 and α_B parameters were presented below and in Figure 2.14.

$0.2 \leq \alpha_0 \leq 0.3$

$0.4 \leq \alpha_1 \leq 0.8$

$\alpha_1 \geq \alpha_B/2$

$\alpha_B \leq 1.04$

$\alpha_B \geq 1.1729 * \alpha_1^{1.6666}$

$\alpha_B \geq 0.44$
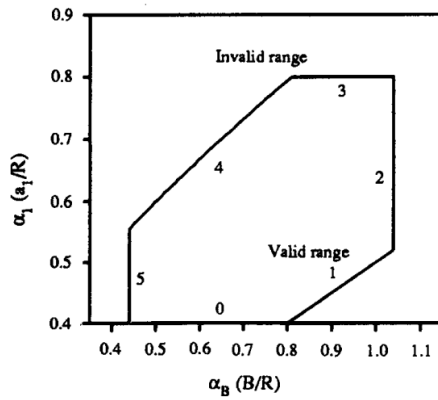
Figure 2. 14 Valid range of α_1 and α_B parameters

Chevron notch is constructed with two circular cuts from symmetric faces at the center of Brazilian disc along the same diametrical cutting plane by using diamond saw. The cutting depth is determined based on radius and the dimensionless geometric parameters such as α_0, α_1 or α_B (Chang et al., 2002). Also, the cutting depth should be identical for both cuts. After specimen preparation, compressive loading is simply applied over the specimen by plate along straight through crack line.

The mode I fracture toughness and minimum dimensionless stress intensity factor solutions were expressed as below (ISRM, 1995).

$$K_{IC} = \frac{P_{max}}{B*\sqrt{D}}*Y_{min} \tag{2.53}$$

$$Y_{min} = u * e^{\vartheta*\alpha_1} \tag{2.54}$$

K_{IC}: mode I fracture toughness (MPa√m)

P_{max}: failure load (N)

B: thickness of disc (mm)

D: diameter of disc (mm)

$Y_{min}*$: minimum dimensionless stress intensity factor

The constants of u and ϑ depend on the values of α_0 and α_B.

In Chang et al.'s work upon granite and marble, CCNBD specimens having 75 mm and 54 mm in diameter and 15-35 mm in thickness were investigated for the size effect on fracture toughness. For specimen preparation, the cutting machine used for opening a chevron notch had a diamond saw with a diameter of 50 mm and a thickness of 0.8 less than 1.5 mm upper limit suggested by ISRM.

K_{IC} results of CCNBD experiments by some researchers are tabulated for various rocks in Table 2.3.

Table 2. 3 Mode I fracture toughness values by CCNBD tests

Material Type	K_{IC} (MPa$\sqrt{m}$)	Source
Barre granite	1.38∓0.06	Iqbal and Mohanty (2006)
Laurentian granite	1.38∓0.03	Iqbal and Mohanty (2006)
Stanstead granite	1.05∓0.07	Iqbal and Mohanty (2006)
Granite	1.35±0.06	Chang et al. (2002)
Marble	1.06±0.08	Chang et al. (2002)
Dolerite	1.43±0.03	Dwivedi et al. (2000)
Agglomerate	1.32±0.05	Dwivedi et al. (2000)
Basalt	1.51±0.06	Dwivedi et al. (2000)
Fine grained Sandstone	0.24±0.01	Dwivedi et al. (2000)
Limestone	0.79±0.01	Dwivedi et al. (2000)
Dolomite	1.09±0.01	Dwivedi et al. (2000)
Quartz-mica Schist	1.27±0.02	Dwivedi et al. (2000)

CHAPTER 3

FINITE ELEMENT PROGRAM AND NUMERICAL MODELLING OF FBD GEOMETRY

The majority of engineering problems is solved by partial differential equations due its complexity (e.g. geometry, boundary conditions, etc.). To find approximate solution of them, finite element method (FEM) is used for different geometries (e.g. stress intensity factors). ABAQUS software licensed to the Middle East Technical University users is a powerful finite element package to handle fracture mechanics applications. This software package is used to compute stress intensity factors of specimen geometries employed in this research. ABAQUS is selected to interpret the models adapted from fracture mechanics problems according to the outputs of stress, strain and displacements. From the numerical models, mode I, mode II and combined mode stress intensity factors of various geometries are computed.

Higher accuracy and convergence for solutions are achieved by increasing number of mesh elements in this program. It is known that as the number of elements and nodes in mesh increase the solution accuracy rises. However, the higher computation time is required based on the problem type and geometry. A detailed mesh optimization work is conducted to increase accuracy of K_I and a_{cn} computations. Overall specimen geometry mesh and special crack tip mesh parameters are varied for the optimization.

3.1 The program structure of ABAQUS

ABAQUS analysis modules are divided into two groups including ABAQUS/Standard and ABAQUS/Explicit which consist of complementary and integrated tools.

- ABAQUS/Standard : general-purpose, FE module
- ABAQUS/Explicit : explicit dynamics, FE module
- ABAQUS/CAE : combination of analysis modules into a complete ABAQUS environment for modelling, managing and monitoring analysis and visualizing its results
- ABAQUS/Viewer: forming output database through the files containing extension .odb to interpret (ABAQUS 6.14-1 Documentation, 2014)

3.1.1 The assignment description of ABAQUS Modules

In this part, some modules such as part, property, etc. are introduced to generate the model in ABAQUS software. Within these modules described below, a logical sequence is followed prior to submit the model into program for being interpreted.

In part module, a new geometry is constructed by selecting proper shape such as rectangle, circle and so on from the related options and in this module, partitions are created. Moreover, number of part can be increased based on the needs.

In property module, necessary material properties of the part are identified. Related module presents many material options listed as elasticity, plasticity, Mohr-Coloumb plasticity, clay plasticity, Drucker Prager and so on. In subsequent step, section should be assigned to the part. In assembly module, parts and instances are defined and entire model including instances is formed by adjusting the location of parts with respect to coordinate system (ABAQUS 6.14-1 Documentation, 2014).

In step module, a sequence of analysis steps is created and can be edited depending on loading, boundary conditions, analysis procedure. Moreover, the specifications about

steps can be changed upon whether analysis is linear or nonlinear. In fact, number of steps and its specifications are influenced by the mechanical behavior of problem.

To get desired outputs related to steps, output requests are obtained from selected output request type. Output requests are divided into two groups which are History Output and Field Output requests. While outputs can be acquired for entire model or specific region from Field Output request, those related to a specified node can be taken from Field Output request.

In load module, a number of loads such as the concentrated and distributed load can be applied with the desired boundary conditions.

In mesh module, mesh elements are created for the parts or instances by using specific mesh techniques. Moreover, element types, shapes, mesh quality and seeding are assigned inside this module.

In interaction module, interactions including surface to point, surface to surface and point to point can be generated. Also, connections are defined between two deformable bodies and between one deformable and rigid body. Other interactions are made by using some constraints such as tie and coupling.

In job module, after essential processes within model are completed, entire model is submitted as a job. Errors and warnings about the job are obtained from monitoring option.

In visualization module, deformation outputs restored to output database are shown by means of contour, vector and X-Y graphics through viewports.

In sketch module, a two dimensional profile is built to form geometry prior to describe a native form of ABAQUS part.

3.1.2 The descriptions of general terms and notation used in ABAQUS

This part identifies common terms and notation utilized in FEM analyses. Basic terms are seeding, partitions and degree of freedoms. The degree of freedoms (dofs) are the number of independent coordinates needed to define location of body and divided into two groups including both rotations and displacements. ABAQUS defines six dofs in terms of displacements as u_1, u_2, u_3 along the directions x, y, z and rotations as ur_1, ur_2, ur_3 around the x, y, z axes, respectively. The restrictions along these components can be applied upon faces, lines and edges.

Partitioning is to divide model region by creating supplementary internal lines, edges and faces. This facilitates to control the movement of the model by implementing necessary loads, boundary conditions and couplings. By this method, meshing quality and solution accuracy is enhanced since it can adjust mesh intensity by focusing on critical regions. Also, partitions can manage the seeding operation in a more qualified. Seeding is to assign nodes depending on discretization of boundary and to adjust the number of nodes upon lines or faces. By increasing number of nodes, mesh refinement is maintained for mesh-sensitive regions. Thus, seeding and partitioning procedure is shown in Figure 3.1.
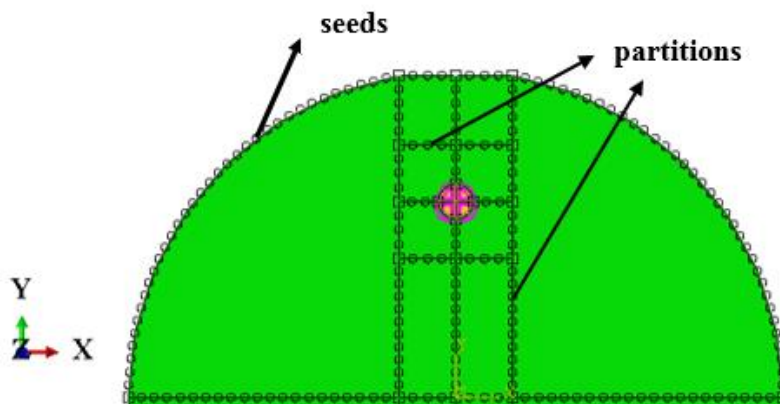
Figure 3. 1 Half of flattened Brazilian disc with partitions and seeds in 2D plane strain

3.1.3 Crack modelling procedure and related terms in ABAQUS Software

ABAQUS software introduces some parameters widely used in the field of linear elastic fracture mechanics. These parameters are denoted as seam crack, crack front or cell, crack tip or line, crack extension direction, singularity elements assigned at crack tip and crack propagation direction in terms of angle (°).

There are two types of cracks defined as seam cracks and notches, namely blunted cracks. Seam crack is represented with a virtual edge and plane having zero thickness as seen in Figure 3.2 and Figure 3.3. This crack type is enclosed by the region; however, it tends to open when loaded. In this study, closed region refers to contour integral region in 2D space. Crack front, crack tip, crack extension direction, singularity elements at crack tip are assigned in this region.
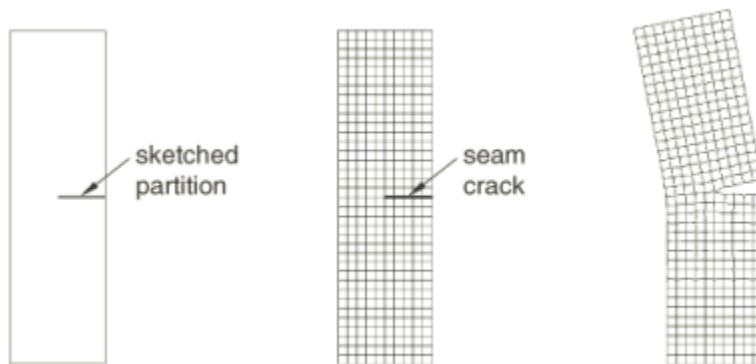
Figure 3. 2 The representation of two-dimensional seam crack (ABAQUS 6.14-1 Documentation, 2014)
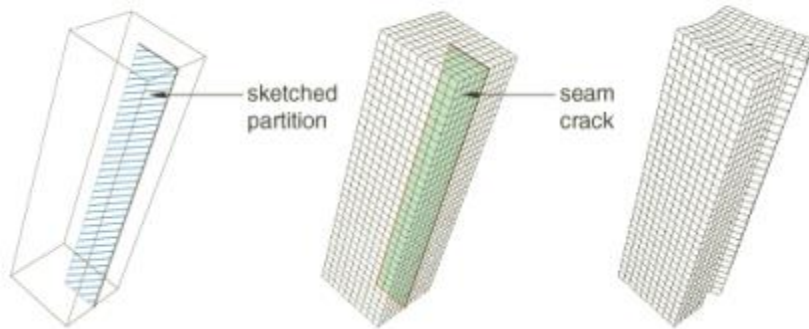
Figure 3. 3 The representation of three-dimensional seam crack (ABAQUS 6.14-1 Documentation, 2014)

After seam crack is indicated, crack front is selected as the first circle surrounding the crack tip. While crack front becomes circular plane in 2D space, the cell replaces in 3D space. Thus, as observed in Figure 3.4 and Figure 3.5, contour integral calculation occurs between the first contour and the outmost contours. Within 3D crack front, contour integral is calculated for each node along the crack line.
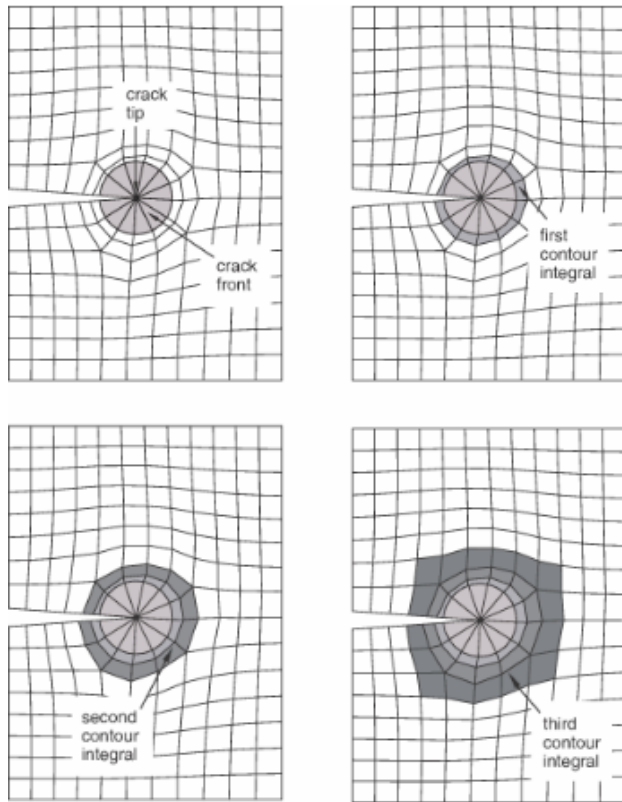
Figure 3. 4 Two-dimensional crack front and successive contour integral regions surrounding the crack tip (ABAQUS 6.14-1 Documentation, 2014)
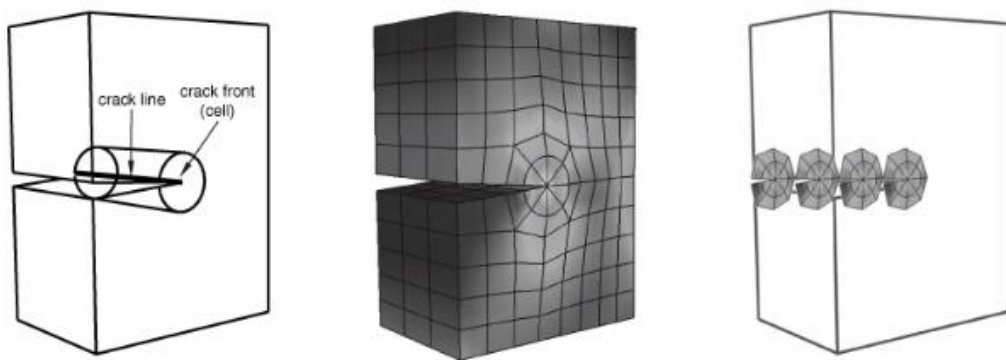
Figure 3. 5 Three-dimensional crack front and contour integral calculation region (ABAQUS 6.14-1 Documentation, 2014)

Crack extension direction shows in which direction the crack starts to propagate during loading. In ABAQUS, it is represented by q vector which is a unit vector parallel to crack extension.

Another issue about the crack modelling is the stress state at the crack tip corresponding to stress singularity. Stress concentration occurs around sharp edges such as cracks, notches due to the influence of far field stresses. At the crack tips, stresses accumulated rise towards infinity and become singular. To calculate it precisely, the relation of square root singularity is used for linear elastic brittle materials. In order to create square root singularity, second-order elements are used at the crack tip since first-order elements ignores the mid-side nodes and so mid-side nodes are preferred for accuracy. In elastic case, mid-side node moves to 0.25 of the distance between native nodes (Figure 3.6). Therefore, these collapsed elements at the singularity are created by eliminating single node or duplicate nodes to be able to extend the crack. The collapsing of 2D elements at the crack tip is illustrated in Figure 3.7.
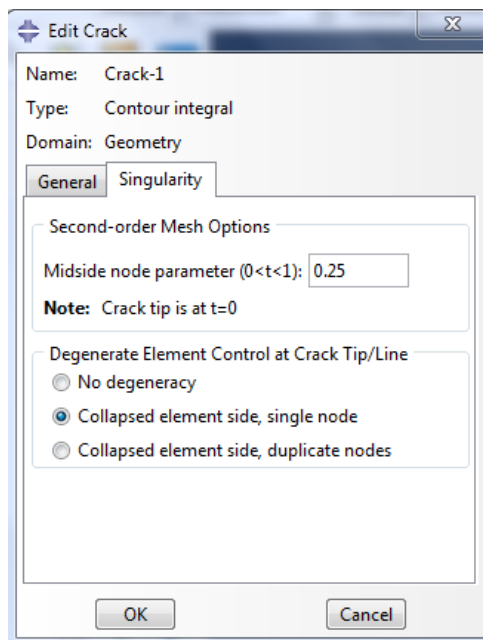
Figure 3. 6 Singularity option at crack tip for 2D and 3D linear elastic region
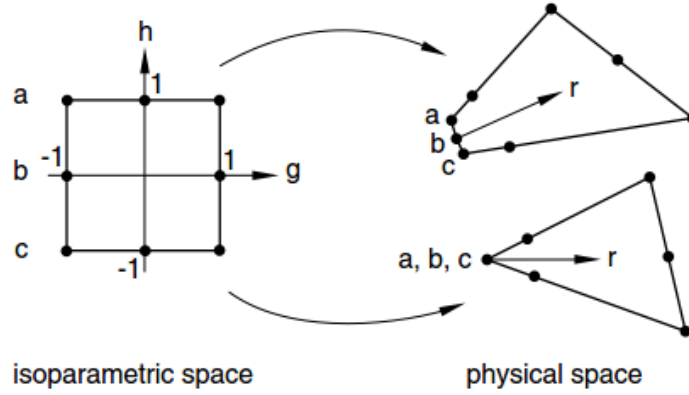
Figure 3. 7 Single-sided collapse of second-order quadrilateral elements at the crack tip (ABAQUS 6.14-1 Documentation, 2014)

After seam crack and contour integral region are specified, stress intensity factors K_I and K_{II} are computed in the contour integral region. The crack propagation direction (CPD) at initial condition is made available as a result of contour integral computation. In this study, maximum tangential stress (MTS) is preferred to compute CPD angle θ. Related formula is given in Equation 3.1.

$$\theta = cos^{-1}(\frac{3K_{II}^2 + \sqrt{K_I^4 + 8K_I^2 K_{II}^2}}{K_I^2 + 9K_{II}^2})$$
(3.1)

CPD angle which makes K_{II} value to be zero. CPD angle is calculated based on crack line. For pure mode I state, K_{II} value is supposed to be zero. In this case, crack propagation is in the straight direction along the crack plane and θ is found as zero. If $K_{II} > 0$, θ becomes less than zero. In contrast, if $K_{II} < 0$, θ becomes greater than zero. This angle is determined from q vector and normal vector n.

3.2 Numerical modelling of FBD geometry

Numerical modeling is performed to compute mode I stress intensity factor and to investigate the characteristic parameters related to the FBD geometry. For the modelling work, ABAQUS v12 package is used to simulate the numerical models of FBD geometries. The variation of K_I value with loading angle and a_{cn}/R value is analyzed.

Mesh convergence study is required to reach the reasonable outcomes for varying loading angles. Approximately 150 models with varying flat loading end widths are run. After completion of mesh convergence study, best fitted equations for K_I and a_{cn}/R based on loading angle are explored. The loading angle range applied is expanded from 2° to 50° to derive a reliable K_I.

3.2.1 Model generation

Two-dimensional plane strain modelling is applied. In the initial trials, diameter and loading angle are selected as 75 mm and 20°, respectively to check the accuracy of the modeling work. This loading angle is chosen since it stays within the optimum range between 20° and 30° (Wang et al, 2004). In addition, accurate boundary conditions with the loading are applied to investigate pure tensile effect upon FBD geometry. The concentrated load of 1000 N is implemented from the bottom layer of the specimen through +y direction. The results are verified at different crack lengths for this angle. Related FBD geometry is shown in Figure 3.8 and related dimensions are listed in Table 3.1. As illustrated in Figure 3.8, the half of crack length (a) is 22.5 mm and the half loading angle (α) is taken as 10°.
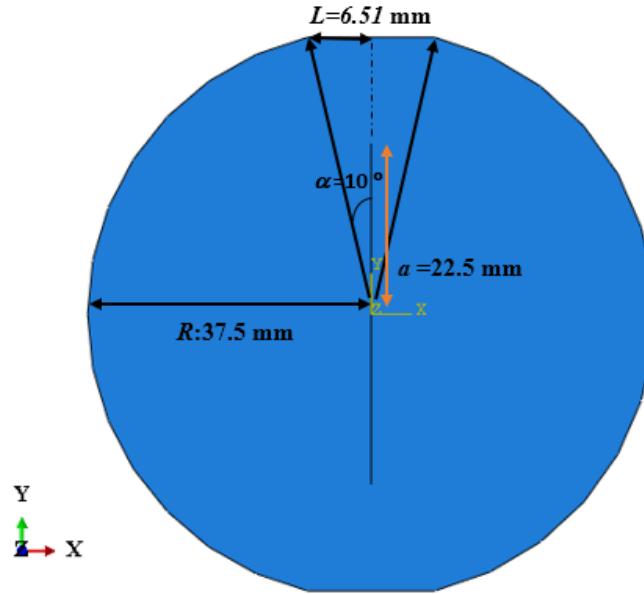
Figure 3. 8 Dimensions of FBD geometry

Table 3. 1 Dimensions of FBD geometry

Dimensions	Value
R	37.5 mm
α	10°
a	22.5 mm
L	6.51 mm

Boundary conditions for FBD modeling are summarized in Table 3.2. FBD model is fixed at the flat top boundary along y-direction. Upper boundary center is fixed in x-direction. The load of 1 kN is applied from the flat bottom boundary along y-direction with a reference point. Reference point transfers concentrated load as an uniformly distributed load along flat bottom boundary and is coupled at +y-direction. There is no displacement constraints applied along the crack plane. Elastic Modulus (E) and Poisson's Ratio (ϑ)

are used as 12 GPa and 0.15, respectively based on the work by Tutluoglu and Keles (2011) on a similar andesite material. These elastic properties do not affect the K_I computations anyway, since Rice J-integral used in contour integral computations of SIFs is a path independent scalar work based entity.

Table 3. 2 Boundary Conditions of FBD test geometry

Boundary Condition	Application Points	Fixed DOF
B.C. 1	Upper central point	$u_1=0$
B.C. 2	Upper flattened length	$u_2=0$
B.C. 3	Lower flattened length	$u_1=0$
B.C. 4	RP1	$u_1=0$, $u_3=0$
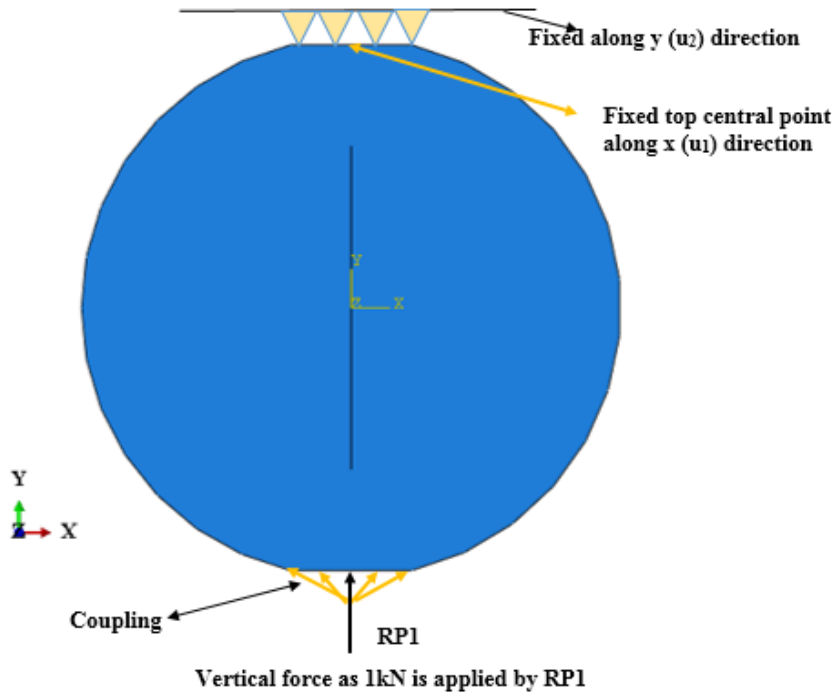
Figure 3. 9 Boundary conditions and loading configuration of FBD geometry

In mesh generation of the model, the most crucial part includes meshing of the whole body. Meshing is the combination of contour integral region surrounding the crack tip and the resting body. According to this, the elements around crack tip are assigned by the singular elements to compute singular stresses accumulated at the tip of crack (Wang et al., 1977). These elements are signified by the factor of $\sigma*\frac{1}{\sqrt{r}}$ as performed in element library of ABAQUS Software.

In models assigned with cracks, meshing process mostly suffers from the size of contour integral region, because extremely large or small size of contour integral region creates wrong SIF values. According to the suggestions made by ABAQUS User's Manual (2014), 16 contour integrals are signified for the outmost contour integral region including the radius of 2 mm. The singular stresses start to be calculated from the innermost contour integral region with the radius of 0.25 mm. Within this region, swept mesh is applied whereas the rest is subjected to structured mesh. During this process, 80000 mesh elements are employed and element type is selected as CPE8R. This element type is expressed as quadratic, plane strain reduced integrated. At each crack tip, 612 quadrilateral elements are found to calculate the mode I stress intensity factor.
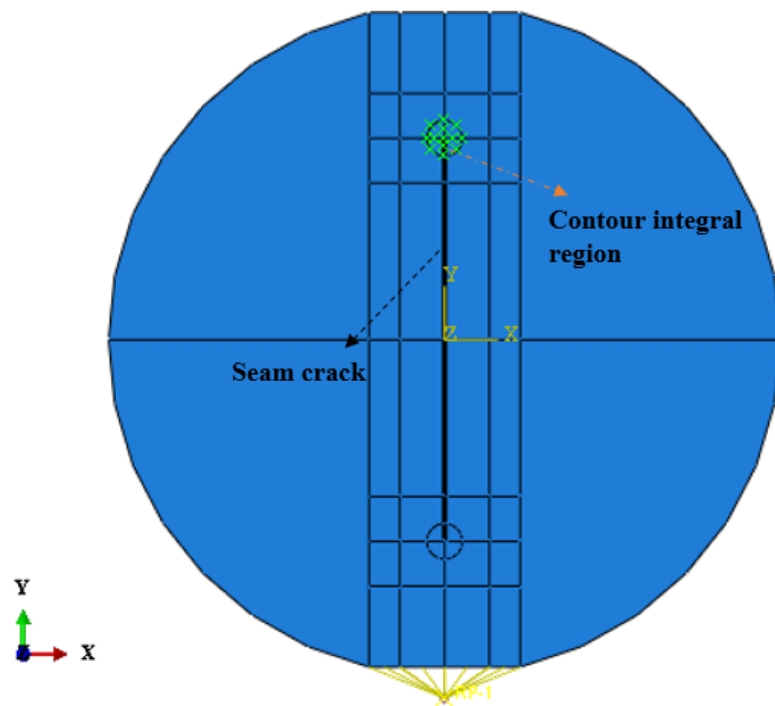
Figure 3. 10 Contour integral region with partitions around the seam crack of FBD geometry
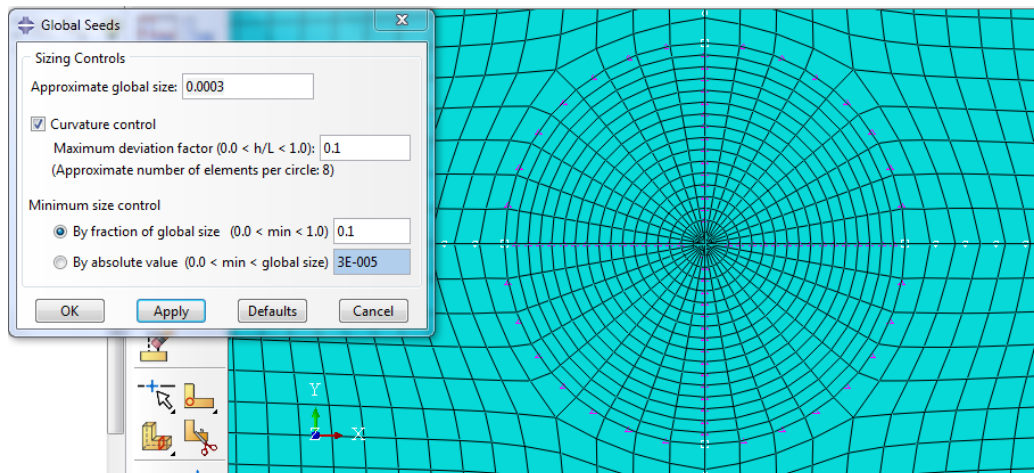
Figure 3. 11 Seeds and meshing surrounding the contour integral region

In Figure 3.12, un-deformed and deformed shape of the overall FBD specimen geometry subjected to symmetric compressive loading at flat ends is illustrated.
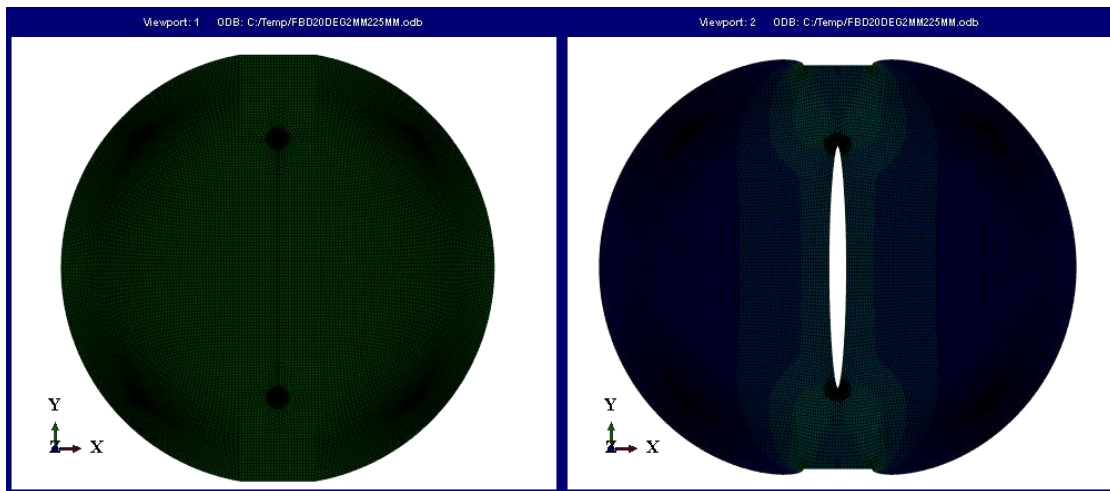
Figure 3. 12 Un-deformed (left view) and deformed (right view) shape of the overall FBD specimen geometry under loading

In Figure 3.13, it is seen that yielding occurs in tension, since Von mises stress values are positive. High stress gradients are seen at the corners under compressive loading and they expand from the crack tip to the flat loading boundary.
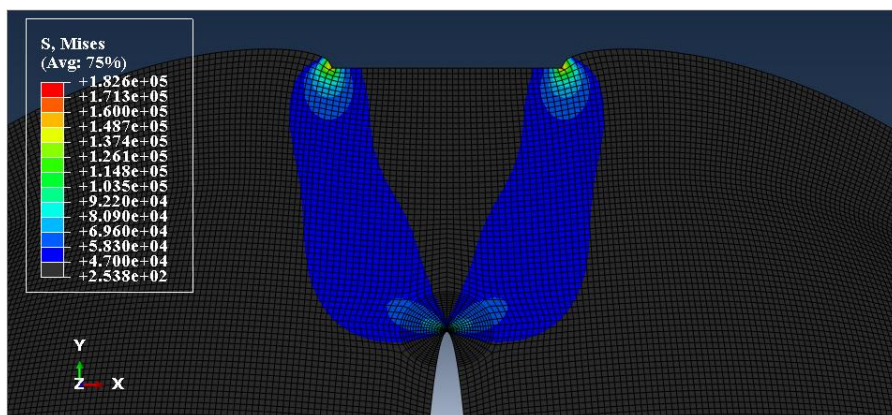
Figure 3. 13 Potential yielding zone developed from crack tip towards the loaded flat boundaries

As loading angle increases, Von Mises stress distribution decreases around the crack tip due to the reduction of compressive zone as loading gets more distributed at the loaded ends.

Besides effect of loading angle, presence of size effect is clarified by comparing Von mises stress distribution at the crack tip. To identify it, FBD geometries with 100 mm and 75 mm diameters are used. According to this, Von mises stress for larger diameter is 7% greater than that of smaller one. Considering this result, it might be said that the size effect exists.
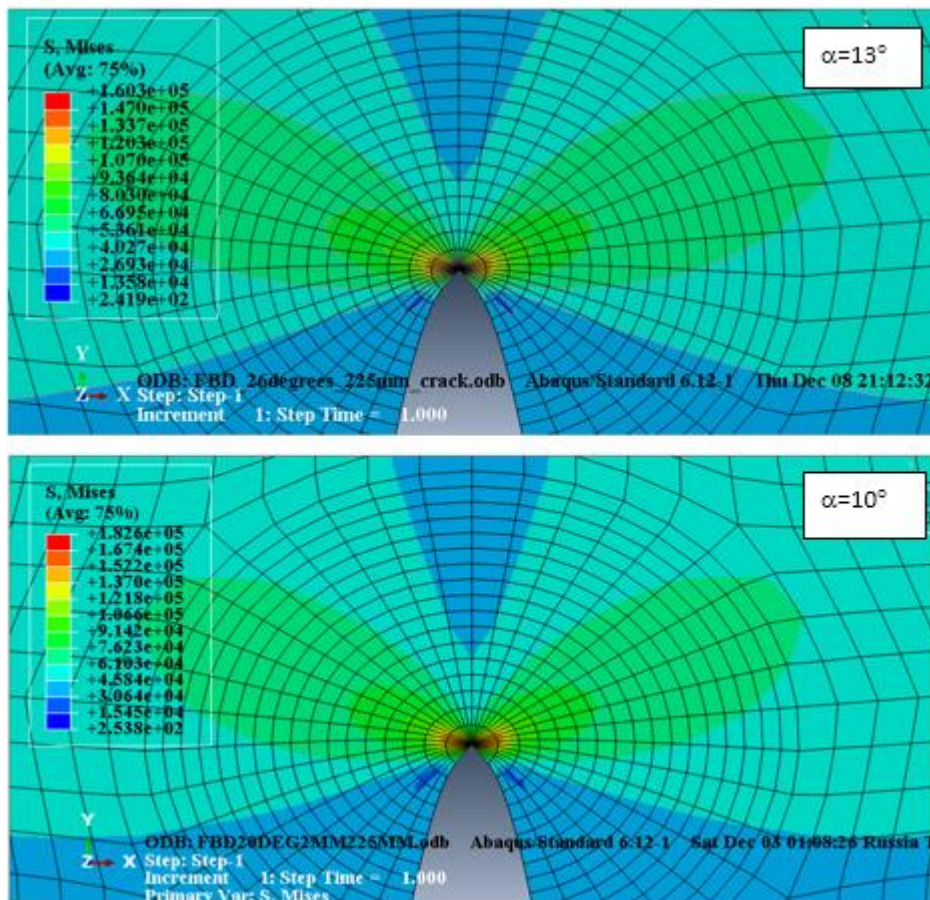
Figure 3. 14 Closer look to Von mises stress distribution around the crack tip for two different loading angles

Although compressive loading is applied upon opposite flat ends, tensile stresses become dominant at the crack tip as seen in Figures 3.15 and 3.16.
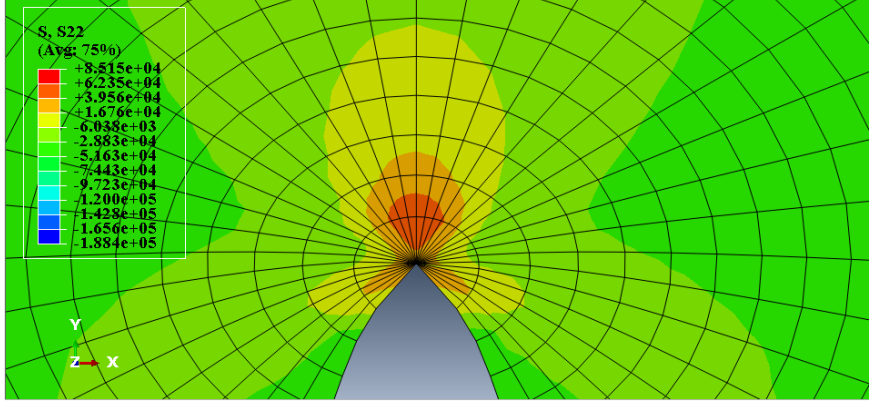
Figure 3. 15 Vertical (s_{22}) stress distribution of FBD geometry
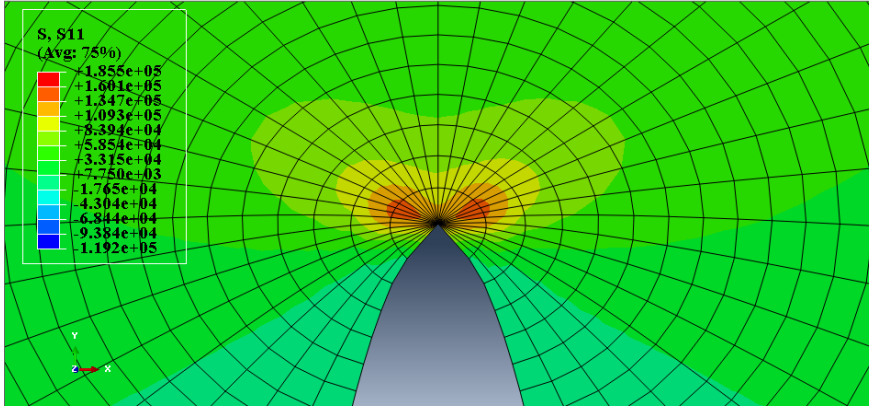
Figure 3. 16 Horizontal (s_{11}) stress distribution of FBD geometry

3.2.2 Mesh convergence study

This analysis is interested in obtaining best accurate stress intensity factors surrounding crack tip. In this work, two important considerations are investigated because of restricting the contour integral region and defined as half of flattened length (*L*) and contour integral radius (r_c). The half of flattened length (*L*) is computed by the multiplication of *sinα* and r_c. However, the relationship between *L* and r_c are not simply

adjusted to each other at each case. When the crack length increases, main area enclosing contour integral radius is enforced to decrease because of reduced distance to the outer boundary. This narrowing area needs to be controlled to get best trend of K_I for various crack lengths. For this reason, optimum contour integral radius is separately determined at each loading angle (2α).

During this calculation, it is distinguished that main mistake in stress intensity factor calculation is caused by the shape of area circumscribing the contour integral region. According to the models created, this region should be square at each crack length to get best fit results.

Another error reveals due to the difficulty of indicating a common contour integral radius peculiar to the size of mesh window (A). Term of A is determined by smallest length surrounding the quarter of contour integral circle. It is found by comparing magnitude of the distance from crack tip to outer boundary and half of flattened length (L). This distance from crack tip to outer boundary is defined by the measurement $(d_f = \cos \alpha *R - a)$. To make the exact radius clear, the possibilities including various contour integral radii are evaluated at each size of square mesh window seen in Figure 3.17.
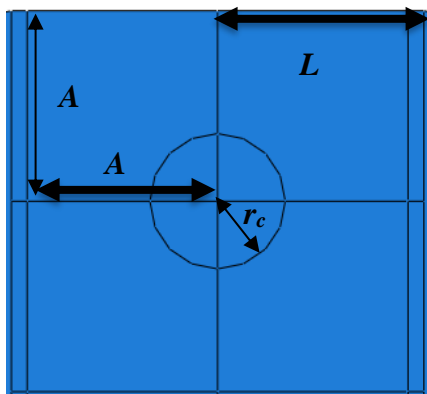
Figure 3. 17 Detailed view to the mesh window

For the narrowed regions, two cases are represented to find the optimum r_c value. First one is FBD geometry with loading angle of 14° at crack length of 33 mm and second one is FBD geometry with loading angle of 20° and crack length of 30 mm. For the first case, mesh size is calculated as 3.22 mm. Considering this, the models with r_c values from 1 mm to 2 mm are run. Thus, optimum contour integral radius of 1.5 mm is indicated at the point where K_I value reaches to a stabile value. Moreover, the model having this radius gives the least K_{II} result. Related stress intensity factors are listed in Table 3.3. In Figure 3.18, K_I values against different r_c values are depicted. In Figure 3.19, detailed view of contour integral region is shown.

Table 3. 3 *K_I and K_{II}* values with respect to r_c values for 14° at crack length of 33 mm

Contour radius (r_c) (mm)	K_I (Pa$\sqrt{m}$)	K_{II} (Pa$\sqrt{m}$)
1	3779.94	-0.08
1.25	3780.98	-0.48
1.5	3780.97	-0.01
1.75	3780.92	0.03
2	3780.59	-0.05
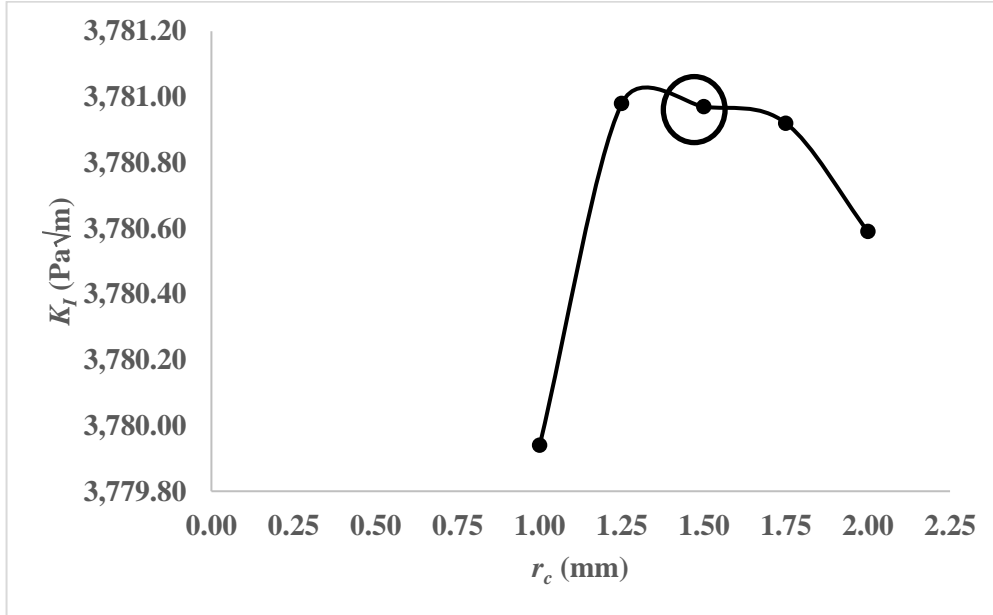
Figure 3. 18 The graph of K_I against r_c for 14° at the crack length of 33 mm
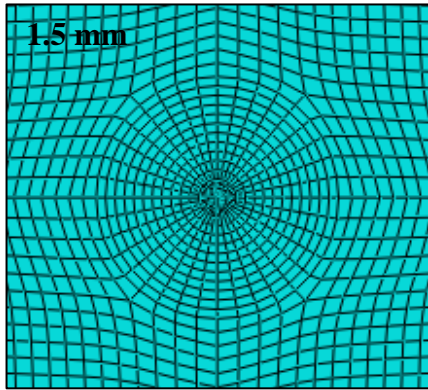
Figure 3. 19 A closer look at contour integral region

For the second case, mesh size is obtained as 6.51 mm. The optimum contour integral radius is indicated as 2 mm considering K_I and K_{II} results. Mode I and mode II stress

intensity factors are listed in Table 3.4. In Figure 3.20, K_I values against different r_c values are shown. In Figure 3.21, detailed view of contour integral region is demonstrated.

Table 3. 4 K_I and K_{II} values with respect to r_c values for 20° at crack length of 30 mm

Contour integral radius (r_c) (mm)	K_I (Pa$\sqrt{m}$)	K_{II} (Pa$\sqrt{m}$)
1.25	3205.94	0.00
1.5	3206.68	0.08
1.75	3206.72	-0.07
2	3206.64	0.02
2.25	3206.31	2.30
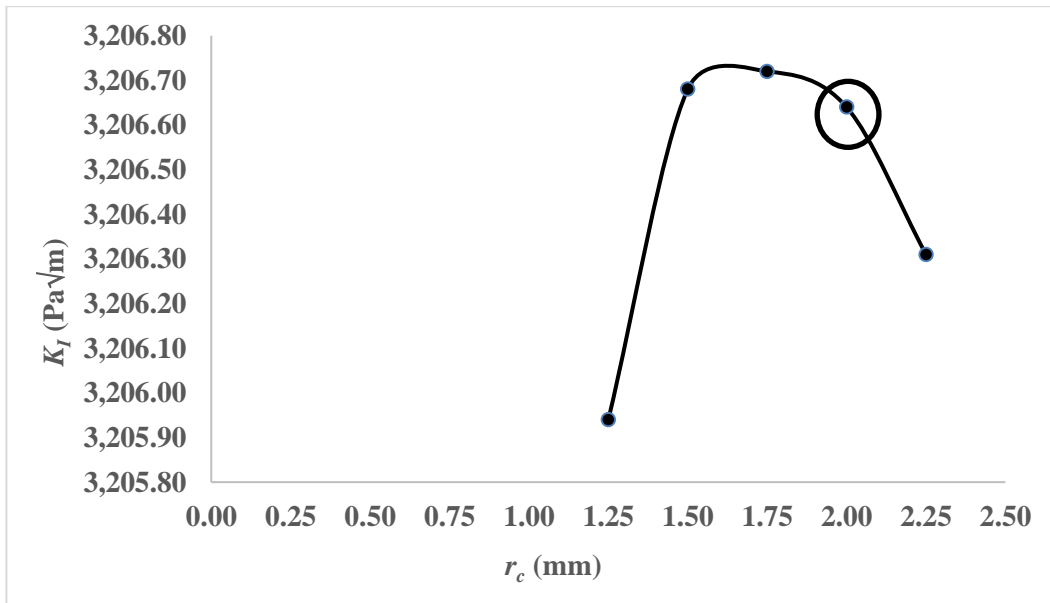
Figure 3. 20 The graph of K_I and r_c for 20° at the crack length of 30 mm
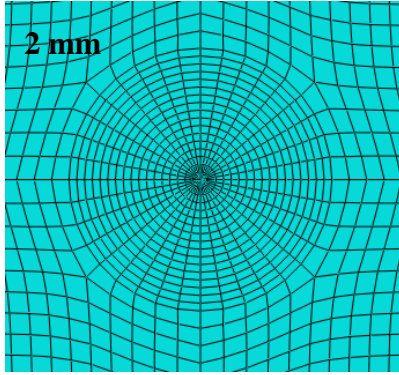
Figure 3. 21 A closer look at contour integral region

Therefore, optimum contour integral radius is found as 1.5 mm for the mesh size between 3 mm and 5 mm whereas related radius is determined as 2 mm for the mesh size between 5 mm and 7 mm.

3.2.3 The formula generation related to FBD geometry

In this mathematical study, two kinds of equations are generated by using statistical program of TableCurve 2D 5.01 version. First one is to determine K_{IC} value required for the rocks with different loading angles tested in laboratory. Second one is to estimate the numerical critical crack lengths based on various loading angles.

In the process of K_{IC} equation generation, numerical FBD models are developed based on different dimensionless crack lengths (a/R) for each loading angle in order to find K_I values. In other words, the K_I values obtained from these models are converted into Y_I values by using the Equation 3.2. Thus, only one fitted graph of Y_I depending on different a/R's is created for each loading angle. Afterwards, from fitted graph, Y_{Imax} value is found as an output of program. In Table 3.5, the results of Y_I and a/R values for 75 mm disc diameter at loading angle of 14° are given. In Figure 3.22, the trend of Y_I against various a/R's is shown.

$$Y_I = \frac{K_I * t * \sqrt{R}}{P} \tag{3.2}$$

$$Y_{Imax} = \frac{K_{Imax} * t * \sqrt{R}}{P} \tag{3.3}$$

Table 3. 5 The values of *a*, *a/R* and Y_I

a (mm)	*a/R*	Y_I
5.0	0.13	0.204
7.5	0.20	0.258
10.0	0.27	0.310
18.8	0.50	0.518
22.5	0.60	0.628
26.3	0.70	0.747
28.8	0.77	0.814
30.0	0.80	0.832
31.5	0.84	0.818
33.0	0.88	0.732
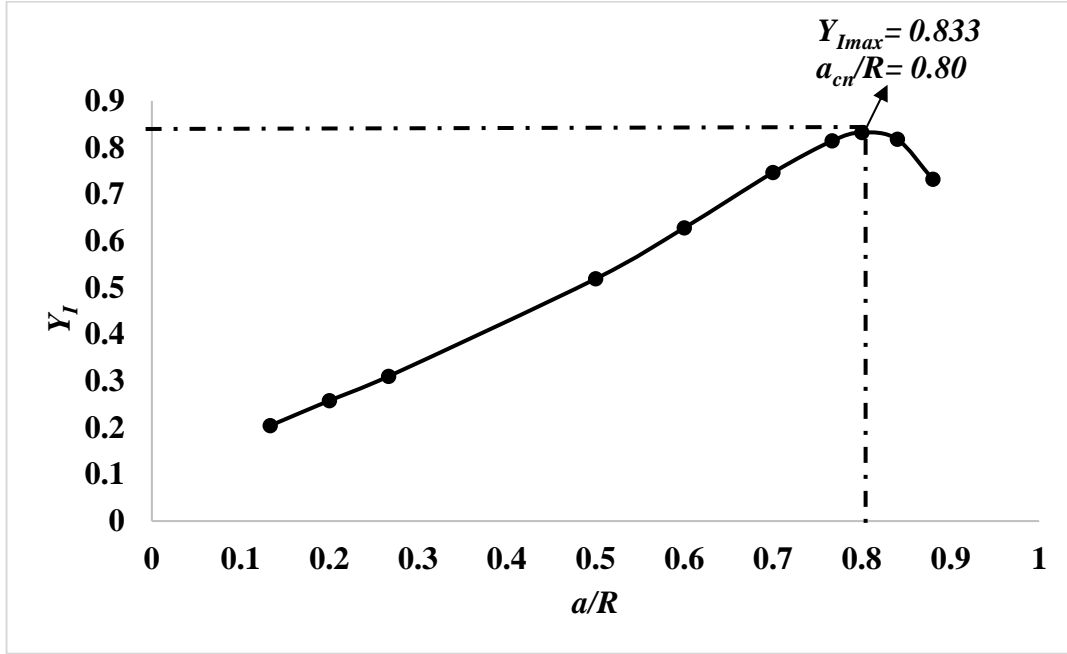
Figure 3. 22 Dimensionless stress intensity factor versus dimensionless crack length at loading angle of 14°

By repeating this procedure for the loading angles ranging from 2° to 50°, Y_{Imax} values depending upon loading angles are obtained and shown in Figure 3.23. In addition, the relation between Y_{Imax} values and loading angles is settled via a fitted equation found from Figure 3.24. The calculated regression is 0.99992 and it demonstrates that this equation given below shows the best fit among produced possible trends. As seen from the Figure 3.24, fitted Y_{Imax} values decrease when loading angle increases. Considering this inverse relationship in an exponential form, limits of this equation are checked to ensure the accuracy of the equation. According to Figure 3.24, loading angle in radians can change from zero to $\frac{22}{7}$ and when 2α in radians goes to utmost limit, Y_{Imax} result becomes zero. Moreover, considering the range of loading angle, optimal angle used as a design parameter in experiments is tried to be detected. In Figure 3.25 (Tutluoglu and Keles, 2011), experimentally measured and numerically computed critical crack lengths are

66

compared and very slight difference is observed between a_{ce} and a_{cn} at the loading angle more than nearly 23°. Thus, optimal loading angle of 26° is found out for FBD specimen since they are consistent. Here, the optimal loading angle is circumscribed in Figure 3.23.
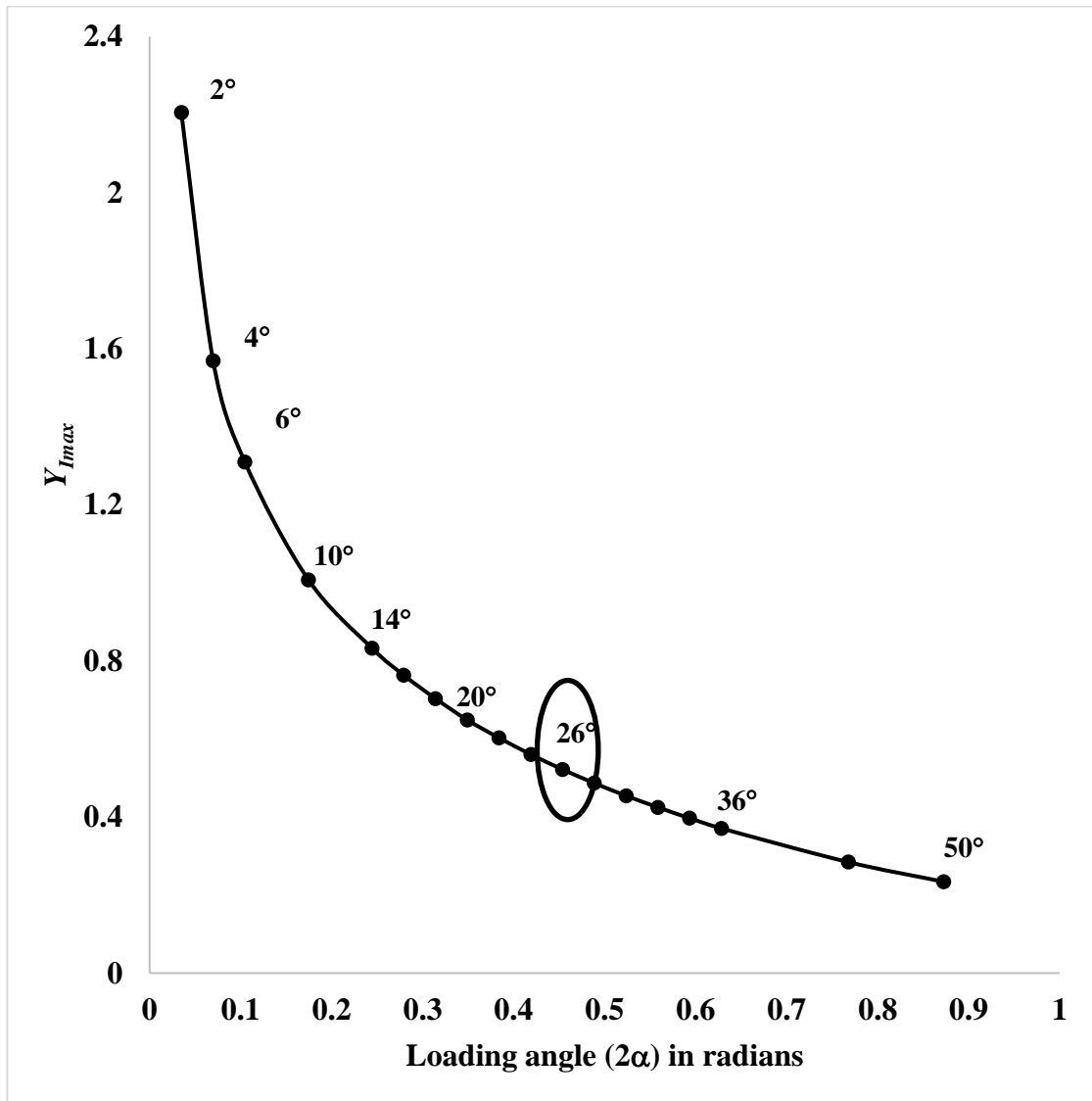
Figure 3. 23 The graph of Y_{Imax} vs loading angle in radians
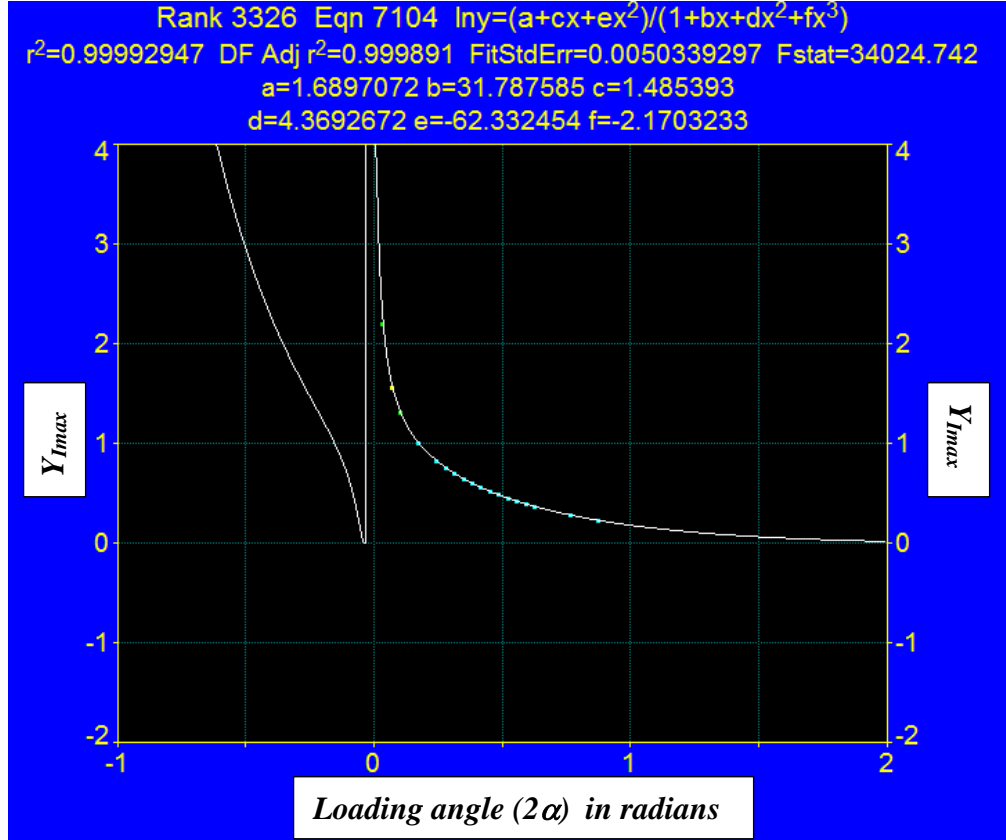
Figure 3. 24 The fitted graph of Y_{Imax} vs loading angle in radians

$$Y_{IMAX} = e^{\frac{1.6897 + 1.4854*(2\alpha) - 62.3324*(2\alpha)^2}{1 + 31.7876*(2\alpha) + 4.3693*(2\alpha)^2 - 2.1703*(2\alpha)^3}}$$

(3.4)
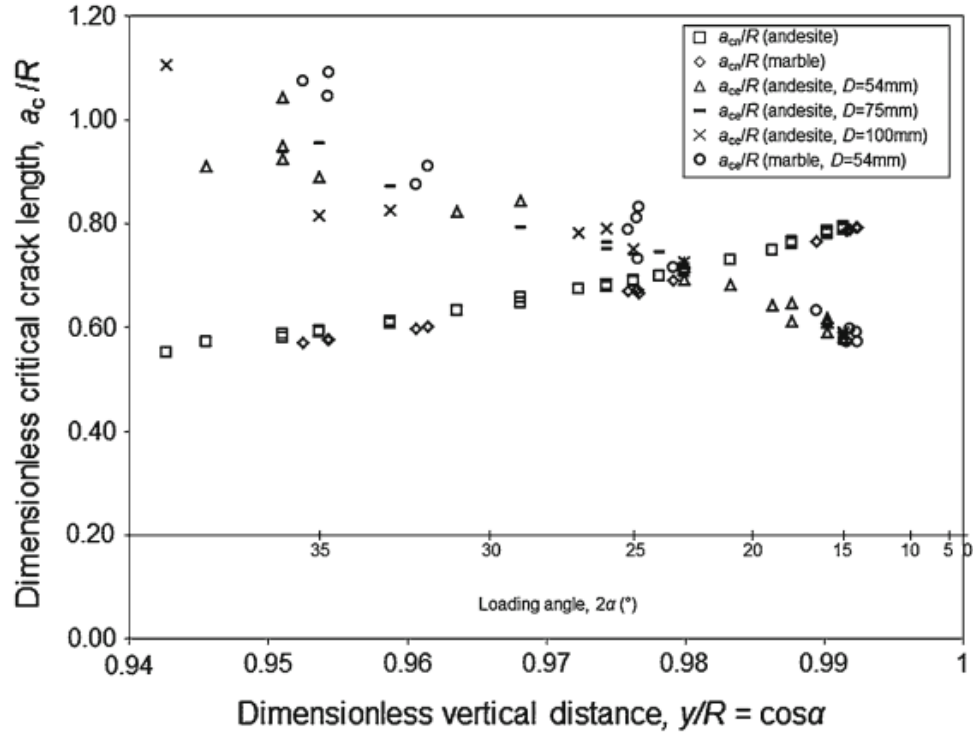
Figure 3. 25 The relation of dimensionless critical crack length corresponding to loading angle in degrees/dimensionless vertical distance (Tutluoglu and Keles , 2011)

In a_{cn} calculation, dimensionless crack length corresponding to the maximum value of Y_I becomes a_{cn}/R. In Figure 3.26, the fitted values of a_{cn}/R's taken from related FBD models are illustrated. According to this, increasing loading angle (2α) in radians leads a_{cn}/R to decrease. Moreover, without any loading angle, numerical critical crack length is limited to be equal or nearly R value. In contrast, when loading angle arrives to π value, a_{cn}/R becomes zero due to the absence of material.

To reach an optimal a_{cn}/R equation, the limits of the equations obtained from Excel and TableCurve 2D programs are compared and equation fitted by Excel program is found more appropriate. The a_{cn}/R equation in terms of loading angle is given by the Equation

3.5. According to the relation obtained from fitted graph, trendline regression is calculated as 0.9994.

$$a_{cn}/R = 0.9974 * e^{-0.844*(2\alpha)} \tag{3.5}$$

Considering the equation, a_{cn}/R intercepts at 0.07 along y direction when 2α in radians reaches to $\frac{22}{7}$. Furthermore, while selecting right equation, whether a_{cn}/R is positive or not along y direction is checked. These results meets the limits of a_{cn}/R equation based on loading angle in radians.
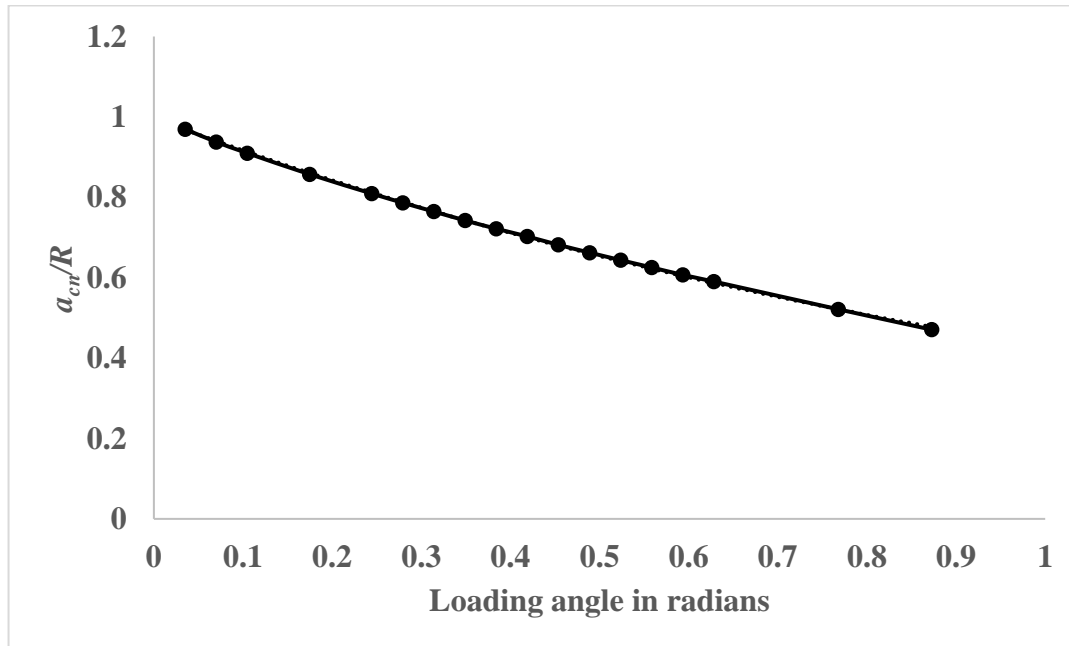
Figure 3. 26 The fitted graph of a_{cn}/R vs loading angle in radians

CHAPTER 4

TESTING FOR MECHANICAL PROPERTIES AND MODE I

FRACTURE TOUGHNESS

In testing work, core specimens prepared from pink-colored Ankara andesite and Afyon marble blocks were used. Core pieces were screened and chosen to minimize the effect of heterogeneities on experimental results. Deformability tests were conducted on both rock types to measure Elastic Modulus and Poisson's ratio to be used as input in modelling work. By breaking these specimens under uniaxial loading, unconfined compressive strengths were evaluated. Brazilian disc tests (BDT) were conducted to obtain rock tensile strength. For mode I fracture toughness testing, FBD core specimens with two different diameters for both rock types were prepared. MTS 815 testing system was used for all tests.

4.1 Servo-hydraulic MTS 815 rock testing system

MTS 815 testing frame is used for all testing work. The main components of this machine are listed below:

- rigid load frame with fixed crossheads (stiffness value= $9 \times 10^9 \text{N/m}$)
- single-ended actuator
- servo-hydraulic service manifold (SHSM)

- directional valve

- hydraulic power unit (HPU)

Servo-hydraulic service manifold and servo-controlled directional valve assure the precise control upon actuator of the machine. Control can be in terms of displacement (stroke) or load. Internal LVDT (linear variable displacement transducer) measures the stroke movement of the actuator piston. Internal differential pressure transducer (ΔP) measures the pressures in the hydraulic circuit. Data acquisition system is calibrated in terms of load in kN based on the signals generated by the pressure transducer. Output signal sent by differential pressure transducer is transmitted to servo-system and control unit. After comparison of feedback signal with desired signal, the required amount of hydraulic fluid is maintained in the hydraulic circuit to keep the pressure steadily at 21 MPa.

Data acquisition system and controller unit are located in the box called as MTS FlexTest 40 controller. This unit contains four channels attached to servo-hydraulic service manifold, differential pressure (ΔP) transducer, extensional and circumferential extensometer, internal linear variable differential transformer and the external load-cell. FlexTest 40 controller provides real-time closed-loop control, with transducer conditioning and function generation to drive various types of servo-actuators (MTS Series 793 Controller Overview, 2011). This device can move the actuator by controlling from load, displacement and strain modules available in function generation segment. Force readings are obtained from externally attached MTS 500kN$\pm$ 0.25 load cell for more precise load readings. Displacement measured by LVDT plugged inside the actuator changes from -50 mm to +50 mm, as limited by the stroke movement.

Total data acquisition rate is up to 4096 Hz from four channels. In deformability tests, data acquisition rate is applied as 8 Hz. The rate in the first initial loading stage of fracture toughness tests is adjusted as 4 Hz. For the maximum load and load drop stage, applied

rate is increased to 32 Hz to catch sudden jumps occur in the load-displacement records at these critical stages of toughness measurements.

4.2 Laboratory work

Laboratory work included mechanical property tests and mode I fracture toughness tests on andesite and marble samples. MTS 815 Rock testing system avaliable in METU Rock Mechanics Laboratory was used in overall testing program.

4.2.1 Deformability tests on andesite and marble

Deformability tests and Brazilian disc tests were performed on andesite and marble specimens. In deformability tests, Elastic Modulus and Poisson's ratio of andesite and marble were found whereas in Brazilian disc tests, tensile strength was measured.

Following the ISRM suggested methods (1978), deformability tests were realized upon NX ($\cong$ 54 mm) andesite and marble core specimens. In these tests, three andesite and six marble specimens were used. Length of cores was around 130 mm for andesite and between 118-128 mm for marble specimens, satisfying the requirement of Length/Diameter$\geq$2. During test procedure run by MTS 815 Rock Testing Machine, axial deformation within gage length of 50 mm was measured via Dual MTS series 632.94F-20 model axial extensometers and circumferential deformation was determined via Epsilon model circumferential extensometer. Using these extensometers, Poisson's ratio ϑ and Elastic Modulus (E) were found. Uniaxial Compressive Strength (UCS), failure load and stiffness at initial loading stage were obtained.

The andesite specimen prepared for deformability test with axial and lateral extensometers is illustrated in Figure 4.1. An example force-displacement graph for a deformability test is given in Figure 4.2.

Figure 4. 1 A typical andesite specimen ready for the deformability test with axial and lateral extensometers
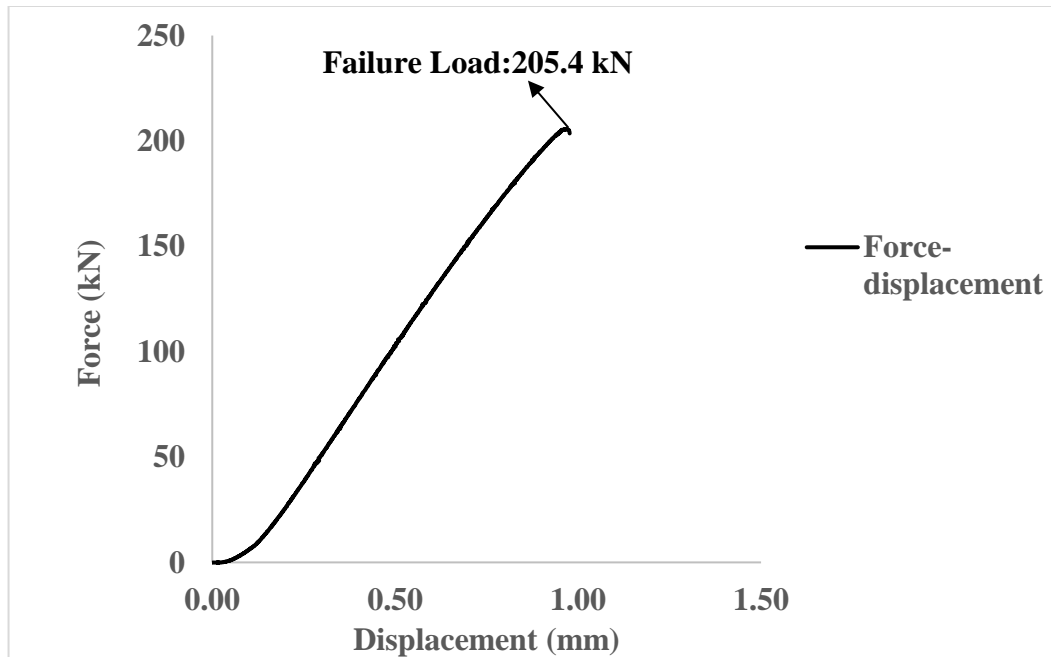
Figure 4. 2 A typical force-displacement curve (Specimen AD2)

The deformability test data and results for andesite were tabulated in Table 1. As seen in Table 4.1, average Elastic modulus of 21.9 GPa and Poisson's ratio of 0.15 were obtained for Ankara andesite material. Failure load, Uniaxial Compressive Strength (UCS), stiffness at the initial loading stage were calculated as 189.7 kN, 84.7 MPa and 250 kN/mm, respectively. As seen from Table 4.1, deformability test results of andesite show less variation compared to those of marble.

Table 4. 1 Deformability test data and results of Ankara andesite specimens

Specimen Id	Stiffness (kN/mm)	Failure Load (kN)	Elastic Modulus (GPa)	Poisson's Ratio	Uniaxial Compressive Strength (MPa)
AD1	250	177.4	23.2	0.16	79.0
AD2	256	205.4	21.1	0.16	91.8
AD3	244	186.4	21.3	0.14	83.2
Average	250±6.0	189.7±15.7	21.9±1.3	0.15±0.01	84.7±7.1

A typical stress-strain curve representing a deformability test on andesite is presented in Figure 4.3.
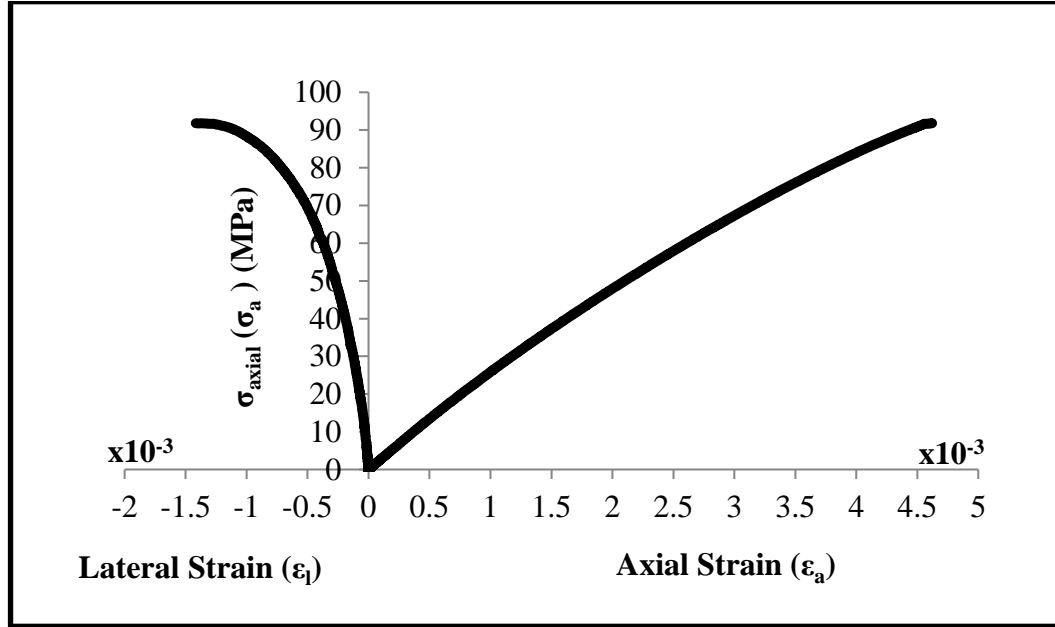
Figure 4. 3 A typical stress-strain curve (Specimen AD2)

Deformability test data and results for marble are shown in Table 4.2. Average values of UCS, Elastic Modulus and Poisson's ratio associated with six marbles are evaluated as 95.2±38.4 MPa, 78.8±6.7 GPa, 0.18±0.07, respectively. Average failure load and average stiffness at initial loading stage of marble are recorded as 213.2 kN and 503 kN/mm. As seen from Table 4.2, average failure load, UCS, stiffness, Elastic Modulus and Poisson's ratio values of marble include much greater variation than those of andesite. This happens due to random initial cracks, fillings and crystal structures in marble.

.

Table 4. 2 Deformability test data and results of marble specimens

Specimen Id	Stifffness (kN/mm)	Failure Load (kN)	Elastic Modulus (GPa)	Poisson's Ratio	UCS (MPa)
M1	442	127.3	79.1	0.20	56.8
M2	531	275.6	76.4	0.21	123.2
M3	534	301.8	72.1	0.20	134.7
M4	471	163.5	82.9	0.13	73.0
M5	542	237.2	81.8	0.11	105.7
M6	499	173.7	80.2	0.24	77.6
Average	503±62	213.2±88.6	78.8±6.7	0.18±0.07	95.2±38.4

The relation between force and displacement is avaliable for a typical marble specimen in Figure 4.4. Related stress-strain curve is shown in Figure 4.5.
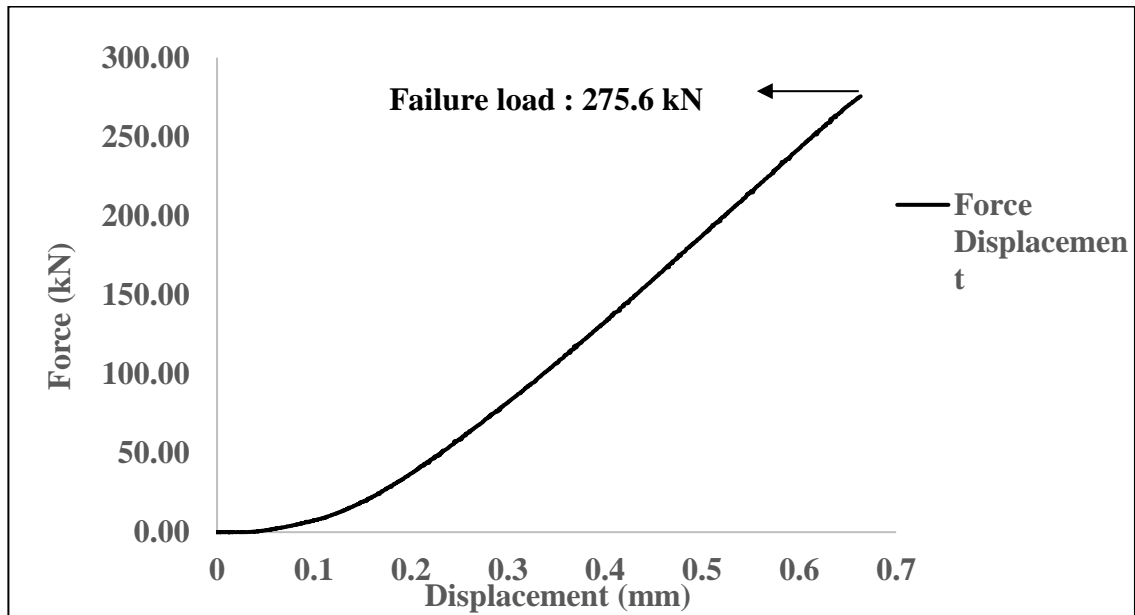
Figure 4. 4 A typical force-displacement curve (Specimen M2)
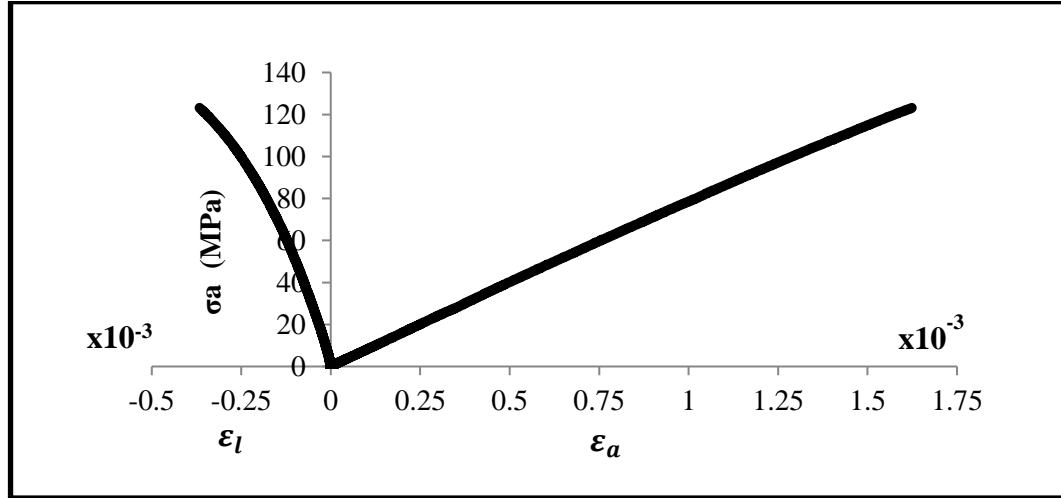
Figure 4. 5 A typical stress-strain curve (Specimen M2)

4.2.2 Brazilian (Indirect Tensile) disc test

In Brazilian disc test (BDT), three andesite and three marble specimens were used to evaluate tensile strength. Andesite and marble specimens were approximately 33 mm in length and around 53 mm in diameter. From Table 4.3, stiffness at the initial loading stage, peak load, and average tensile strength for andesite were calculated as 106 kN/mm, 26.1 kN, and 9.57 MPa, respectively.

Table 4. 3 Brazilian disc test results of Ankara andesite specimens

Specimen Id	Stiffness (kN/mm)	Peak Load (kN)	Tensile Strength (MPa)
ADB1	106	24.1	9.02
ADB2	85	22.8	8.35
ADB3	126	31.3	11.35
Average	106±21	26.1±5.3	9.57±1.78

In Figure 4.6, force-displacement curve for a typical andesite specimen under BDT is shown. This is not a FBD specimen under tensile loading; however, P_{min} can be observed

under concentrated compressive loading of 16.8 kN. For two andesite specimens, this load drop and P_{min} is observed too. The average of P_{min} values for andesite is computed and included in overall processing of FBD test results in Chapter 5. This critical point is marked as P_{min} in Figure 4.6.

.
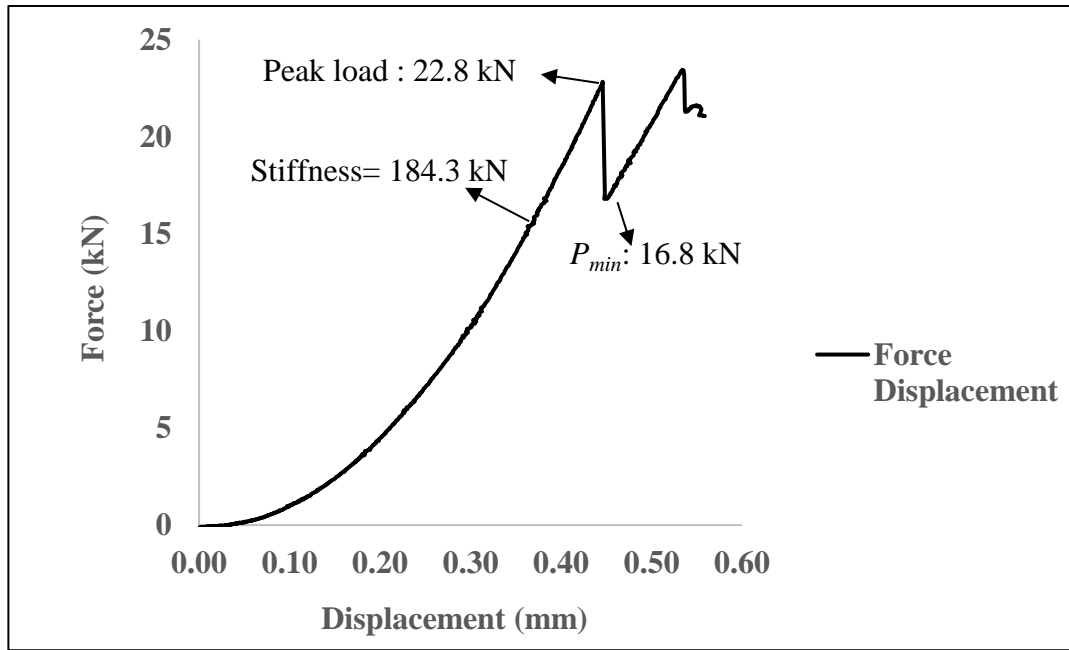
Figure 4. 6 A typical force-displacement curve for Brazilian tensile strength test on andesite (Specimen ADB2)

The stiffness at initial loading stage, peak load, and average tensile strength for BDT tests on marble are calculated as 198 kN/mm, 28.8 kN, and 10.83 MPa, respectively. Results are summarized in Table 4.4.

Table 4. 4 Brazilian disc test results of marble specimens

Specimen Id	Stiffness (kN/mm)	Peak Load (kN)	Tensile Strength (MPa)
MB1	185	24.7	9.21
MB2	224	32.5	11.88
MB3	184	29.2	11.40
Average	198±26	28.8±4.1	10.83±1.06

In Figure 4.7, force-displacement curve related to a typical marble specimen under BDT is illustrated. As in andesite specimens, P_{min} values are clearly detected for BDT tests on marble. From Figure 4.7, P_{min} is obtained as 22.6 kN. For the two other marble specimens, this behavior is observed and the average of P_{min} values for marble is included in fracture toughness evaluations as zero loading angle entry.
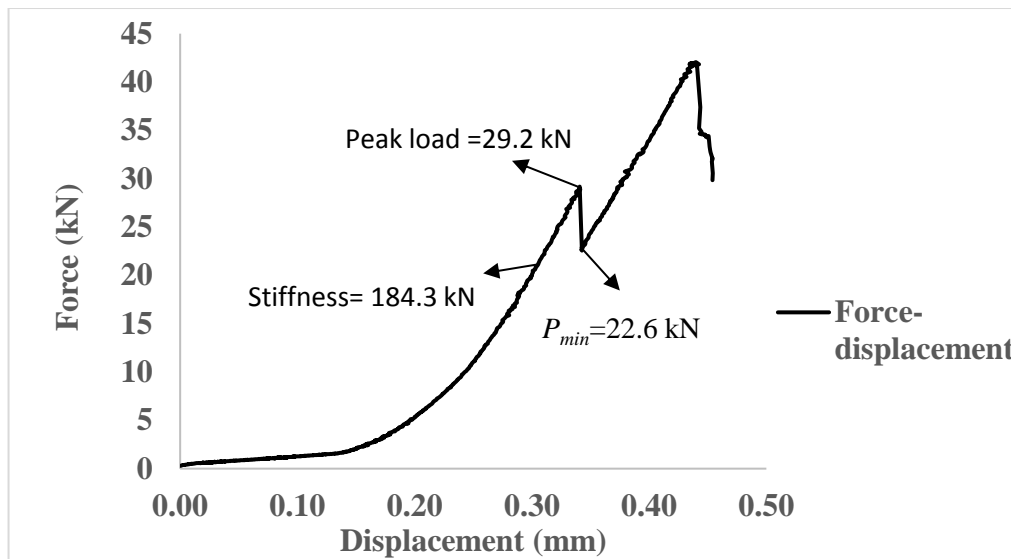
Figure 4. 7 A typical force-displacement curve for Brazilian tensile strength test on marble (Specimen MB3)

4.3 Fracture toughness tests for Ankara andesite and marble

FBD test method is mostly preferred due to simple loading configuration without special testing pieces such as steel jaw. Requirement of pre-notching is not needed resulting in easy preparation of samples. This section includes FBD specimen preparation, specimen coding, MTS loading system procedure, and crack length measurement technique.

4.3.1 FBD specimen preparation

Cores with 75 mm and 100 mm diameters were drilled from big blocks and machined into proper sample dimensions. To reduce thicknesses into desired dimensions and to create flat surfaces, a milling machine with a diamond impregnated milling cutter was used.

At initial stage of FBD specimen preparation, core specimens are positioned properly for thickness adjustment as observed in Figure 4.8. The thickness is decreased to 67.5 mm and 37.5 mm for FBD specimens with diameters of 100 mm and 75 mm, respectively.

Figure 4. 8 Adjustment of thickness in diametral position

As seen in Figure 4.9, the flattened ends were constructed for the optimum loading angle aimed to be around 26°.
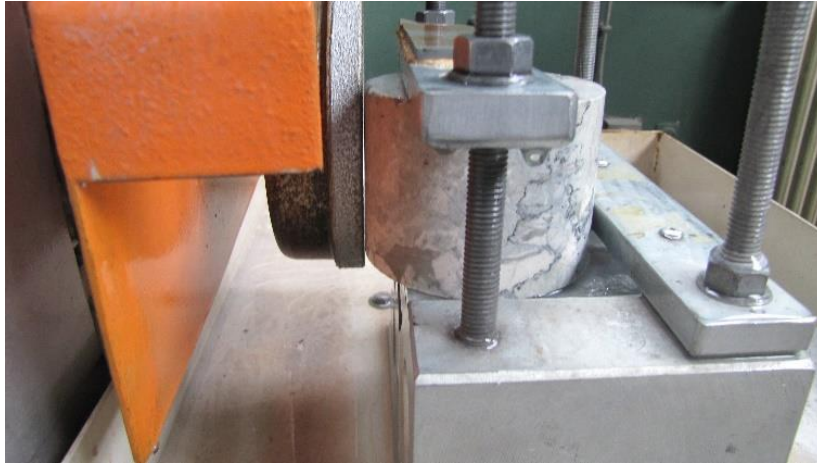
Figure 4. 9 Constructing parallel flat surfaces from curved ones

At the next step of specimen preparation, core specimen was axially positioned and screws were tightened to avoid any movement during grinding. In addition, horizontal set screw down to flat plate was held behind the specimen to provide parallelism for the upper and lower surfaces as illustrated in Figure 4.10.

Figure 4. 10 Constructing parallel flat surfaces with a horizontal set (axially positioned)

After FBD specimen preparation, specimen coding was done as shown in Figure 4.11.
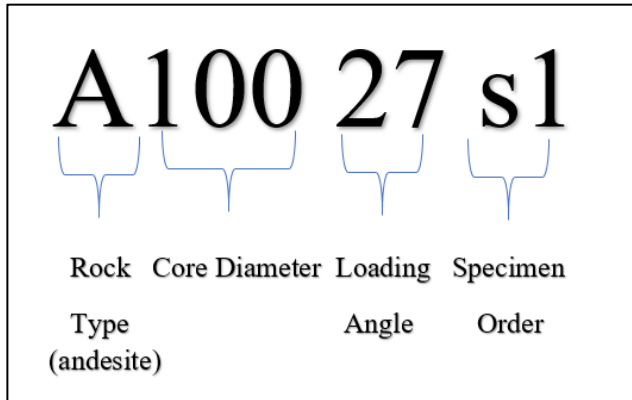
Figure 4. 11 Specimen coding for FBD specimen

In labelling, rock types are specified by the initial letters of *A* and *M*, respectively for Ankara andesite and marble. The core diameters for 75 mm and 100 mm samples are represented as 75 and 100. Then, loading angles controlling the width of the flat ends and varing from 25° to 29° are indicated. Specimen number order started from first digit of 1 and changed as subsequent numbers of 2, 3 and so on.

4.3.2 MTS displacement-controlled loading procedure for FBD testing

In MTS FlexTest 40 electronic controller console, programmed procedure is prepared for loading FBD specimens. When procedure is initiated, failure detector and data acquisition steps join in the action of data acquisition. Procedure starts with high rate loading rate running at displacement rate of 0.4 micron/s. The step of high rate loading continues until first failure detector reaches a point at which applied force is 90% of estimated first fracturing load. Low rate loading step takes over later around fracturing and load drop stages. Experimental critical crack length might not be observed with a low loading rate. Loading rate has to be lowered and data sampling rate has to be increased in order to catch the load drop and experimental crack length clearly and precisely.

In first data acquisition step, continuous data storage frequency is adjusted as 4 Hz. After initial failure detector finishes, within the step of low rate loading, displacement rate is decreased from 0.4 micron/s to 0.01 micron/s to gain extra time to take photos for experimental critical crack length during crack growth keeping up until load reaches to minimum value. In addition, during that stage, since more data storage is needed to prevent data loss, data frequency is kept at 32 Hz. This loading step carries on until the displacement of 2.4 micron is achieved and so duration of 240 seconds (4 minutes) is gained for photos. After, low loading rate is replaced with a higher loading rate of 0.4 micron/s. This loading rate switch provides saves time in testing. Second failure detector starts when first failure detector step is completed and it continues to the end of second high rate loading. It is limited to the 60% of maximum applied force and finishes at that value. In final step, when it reaches to 60% of maximum force, the stroke goes down at the displacement rate of 1 mm/s along 5 mm. A typical displacement rate curve for FBD testing is illustrated in Figure 4.12.
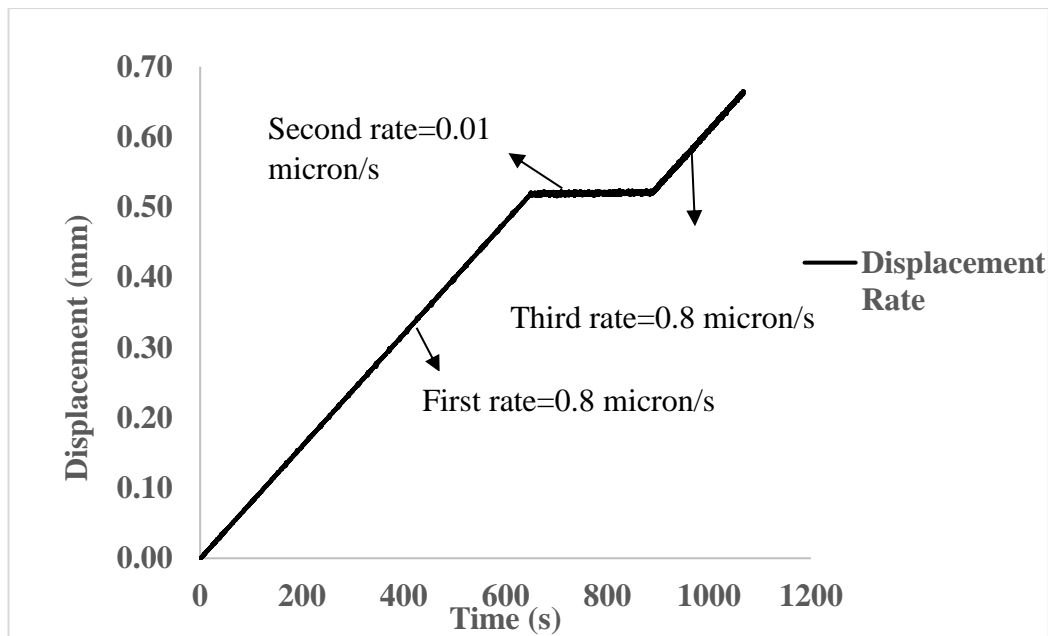

Figure 4. 12 A typical displacement versus time curve for FBD testing (Specimen A10027s1)

In testing marble samples, displacement rate is applied as around 0.3 micron/s. This rate results in rapid breakage of the marble. Under fast displacement rate, early crack growth happens, even in elastic region of the samples, crack formation can occur. In other words, without reaching peak load, micro cracks begin to develop. Another reason behind this type of crack formation is inherent fractures and preexisting cracks such as micro cracks inside the material. Blocks used in preparation of marble samples included arbitrarily oriented fractures and weaknesses. Efforts were made to adjust the weakness plane and loading direction properly in a way that weakness planes were not aligned with the expected cracking path as seen in Figure 4.13. The orientation of discontinuities is seen to be nearly parallel to the loading direction and more photos related to this issue are available in Appendix C. In the experiments, marbles containing inherent fractures and discontinuities showed more variation in toughness results compared to test results of more homogenous andesite.

Figure 4. 13 Typical 75 mm diameter marbles with discontinuities parallel to loading direction

These features may facilitate to break the samples into two halves and reduce the minimum load (P_{min}) carried by specimen due to early loss of material. Moreover, since fast loading does not allow adequate time for stress redistribution surrounding the crack tip, stress does not find a path to escape and yielding occurs earlier than expected levels.

To eliminate early fracturing, current recommendation for first and third ramping loading rates in procedure is to change it with the lower rates of 0.2 micron/s or 0.3 micron/s.

4.3.3 Photographic a_{ce} calculation procedure

Crack surface observations after the splitting of specimens indicated pure tensile separation. No indication of shearing movement was observed along the crack surfaces after tensile splitting of the specimens. Crack propagation was seen to be along loading direction with minimum deviation from the expected path towards the center of the loaded flat external boundaries.

After the first initiation, there is a drop in the load records and crack propagates a while in a stable manner. Then, a load increase is observed in the test record until a load level is reached at which crack extends to a state called critical crack length. At this state close up shots were made to photograph the stable crack in samples. From the photos, experimental critical crack lengths were measured by means of digital image processing software. A steady compatibility was achieved between experimentally measured and numerically computed critical crack lengths. Difference percentage was below 1% for the critical crack lengths of overall testing program.

In Figure 4.14, FBD andesite specimen of 100 mm diameter under loading is seen before crack formation.
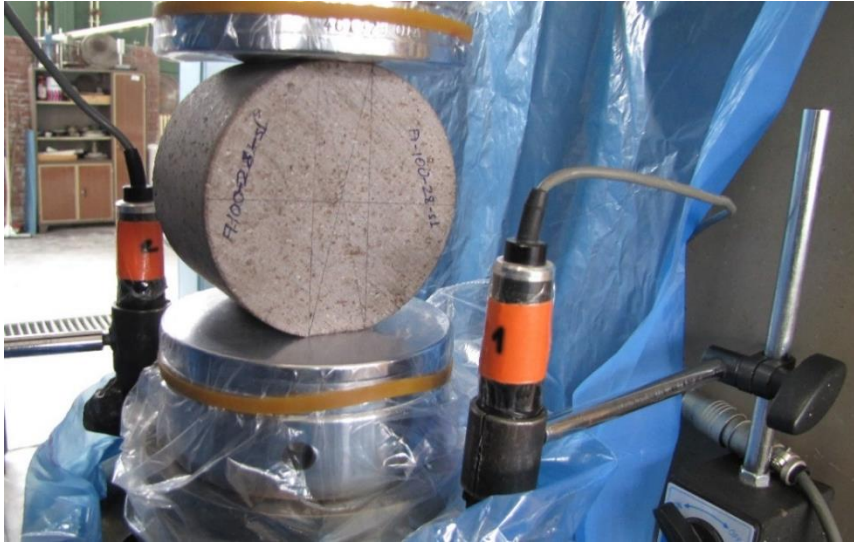
Figure 4. 14 Andesite specimen subjected to FBD testing before crack formation

When force drops to local minimum P_{min}, initial crack formation referred as critical crack length can be observed as in Figure 4.15.

Figure 4. 15 Experimental critical crack length formation at minimum load

Initial crack exposure trials included dye-penetrant spray application to make the experimental crack length more visible. Although this technique functions well for cracks inside metals, this spray did not penetrate sufficiently into the crack and and dark color caused by spray made a_{ce} detection difficult, (Figure 4.17). Because of this, spray was applied only once and in proceeding experiments, this wasn't implemented. Instead of using spray, measurement of a_{ce} was performed by Photoshop software as shown in Figure 4.16.
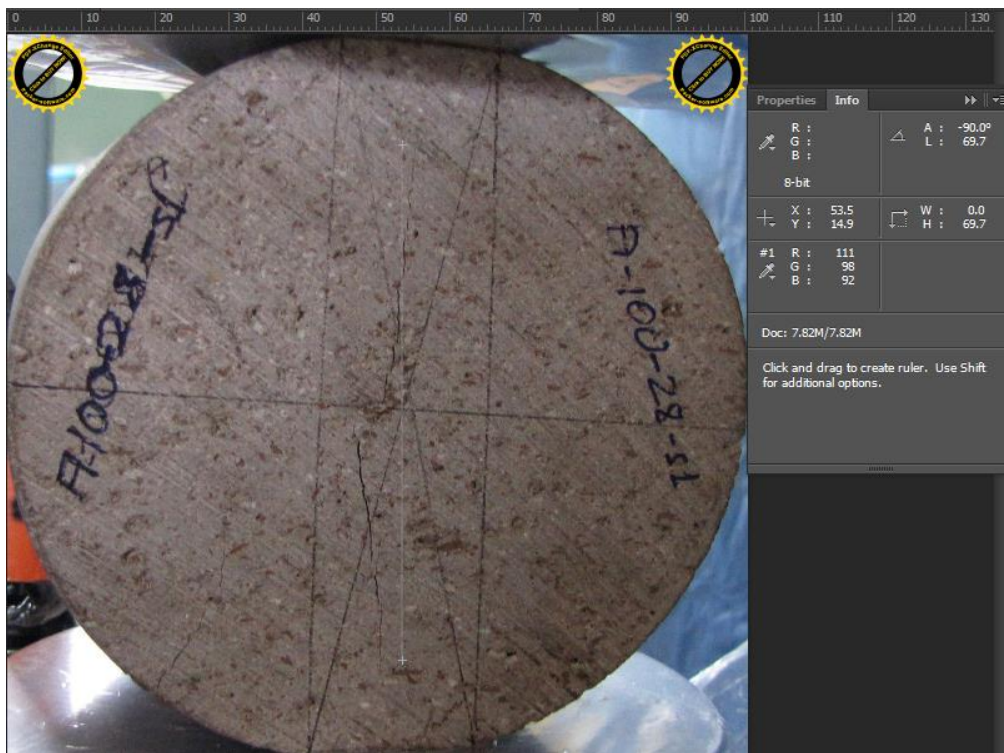

Figure 4. 16 FBD specimen of A10028s1 with $2a_{ce}$ = 69.7 mm scaled by Photoshop

As a means of checking, critical crack length measurements can be confirmed manually by a ruler (Figure 4.17).

Figure 4. 17 Experimental critical crack length measurement by ruler after fracturing and dye penetrant spray application
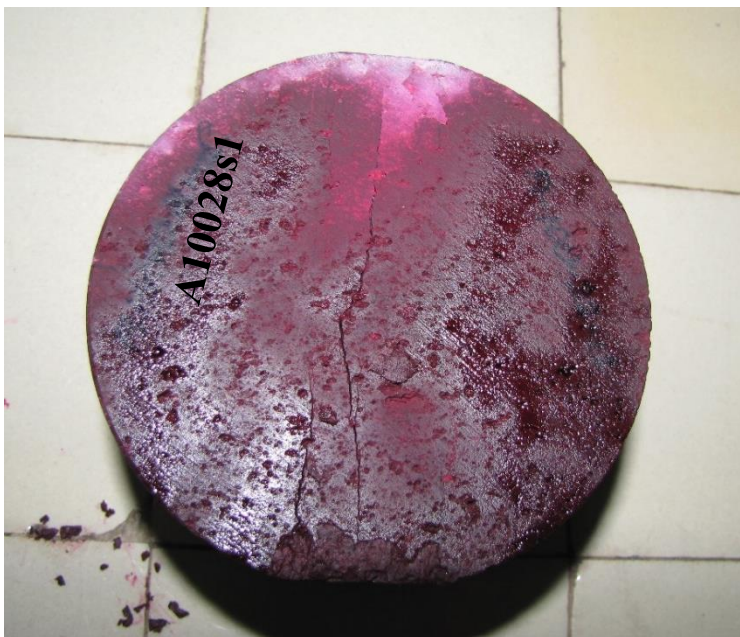

Figure 4. 18 Andesite specimen after fracturing

CHAPTER 5

EXPERIMENTAL RESULTS AND DISCUSSION

Fracture toughness tests were conducted on Ankara andesite and marble core samples by using MTS 815 Rock Testing Machine. Specimens of 75 mm and 100 mm in diameter were subjected to tensile mode fracture toughness testing. Specimen loading ends were flattened to achieve a specimen geometry with the optimum loading angle. In all, nineteen experiments were carried out. Brazilian disc test findings were integrated into fracture toughness evaluations to get an idea about how compressive loading and loading angle influence fracture toughness values.

5.1 Fracture toughness test results for Ankara andesite with a diameter of 75 mm

Three 75 mm diameter andesite specimens were included in FBD testing. Its thickness was reduced to about 37.4 mm and flattened boundaries were constructed for loading angles between 0.44 (25°)-0.50 (29°) radians. The sketch below illustrates some geometric characteristics of FBD geometry. The flattened length ($2L$), radius (R), half of experimental critical crack length (a_{ce}) and distance of crack tip to central load application point (d_e) are approximately 17.5 mm, 37.5 mm, 24.6 mm and 11.9 mm for a typical 75 mm diameter andesite specimen, respectively. The photos concerning with all FBD specimens are found in Appendix B.
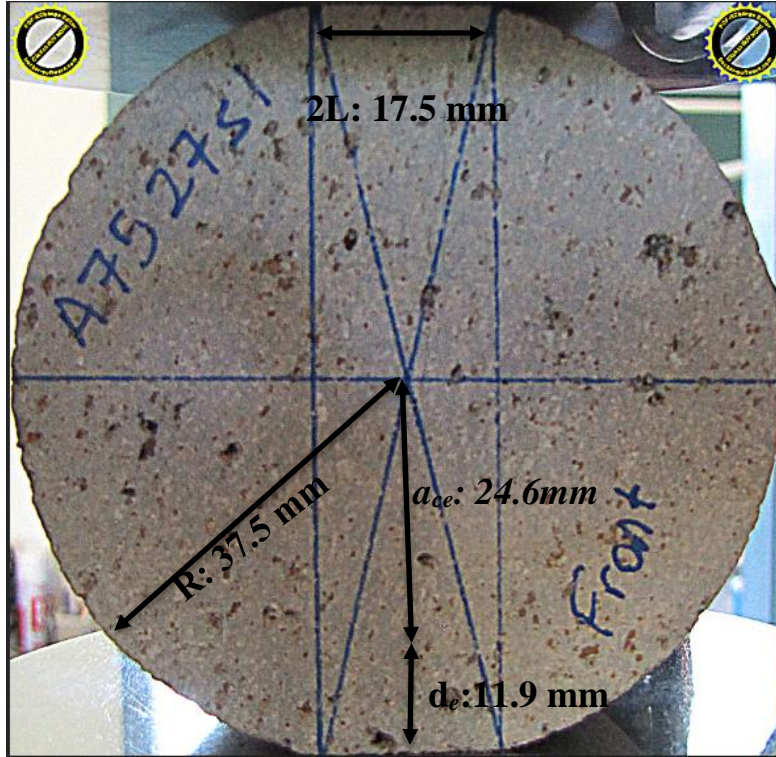
Figure 5. 1 A typical 75 mm diameter andesite specimen with the dimensions (A7527s1)

Stiffness values and critical crack lengths measured according to loading angles are shown in Table 5.1. Also, related loading angles, corresponding Y_{max} values, critical loads and computed fracture toughness results are presented in Table 5.2. According to this, Y_{max} values change between 0.480 and 0.532. The average values of K_{IC} is found as 2.58 MPa$\sqrt{m}$. The photographic a_{ce} measurement procedure is seen in Figure 5.2. The photos showing a_{ce} measurements for all FBD specimens are available in Appendix D.

Table 5. 1 Critical crack length comparison and stiffness values for 75 mm diameter FBD andesite specimens

Specimen Id	a_{cn} (mm)	a_{ce} (mm)	a_{cn}/R	a_{ce}/R	$k_{initial}$ (kN/mm)	k_{drop} (kN/mm)	k_{crack} (kN/mm)
A7528s1	24.6	24.4	0.66	0.65	215	4313	191
A7527s1	25.0	24.6	0.67	0.66	221	3376	163
A7525s1	25.7	27.6	0.69	0.74	208	6299	112
Average	**25.1±0.6**	**25.5±2.1**	**0.67±0.02**	**0.68±0.06**	**215±7**	**4663±1636**	**155±36**

Table 5. 2 Loading angle, Y_{max}, P_{min}, K_{IC} values of 75 mm diameter FBD andesite specimens

Specimen Id	2α (radians)	Y_{max}	P_{min} (kN)	K_{IC} (MPa $\sqrt{m}$)
A7528s1	0.496 (28°)	0.480	42.7	2.83
A7527s1	0.478 (27°)	0.498	38.9	2.68
A7525s1	0.445 (25°)	0.532	30.4	2.24
Average	**0.473±0.028**	**0.503±0.029**	**37.3±6.9**	**2.58±0.34**

According to this characteristic force-displacement curve (Figure 5.3 (a)), loading is separated into three steps. In first step of loading (oa), elastic behavior is seen in specimen. When load attains a peak load, crack starts to form at the center. In second step (ab), as soon as crack initiates, load tends to decrease. The unstable crack growth occurs until load value arrives at minimum. P_{min} replacing the peak load is the critical turning point (b) which transforms crack growth from unstable region into stable region. Unstable crack ceases to proceed because of loading decreases. In third step (bc), after P_{min} is reached, since load increases, crack propagates in a stable manner by forming secondary

cracks. As a result of ongoing load increase, specimen is broken. The fluctuations on load levels ensued from subcracks don't modify results of the test after breakage is complete.

To perform a successful test, P_{min} should be seen when unstable crack grows and after primary crack is formed, secondary cracks can be seen. It means that after P_{min} is detected, stable crack growth occurs. Also, another remark is that the successive peak load can surpass previous peak load since the confining pressure is taken out because of the voids and secondary cracks.
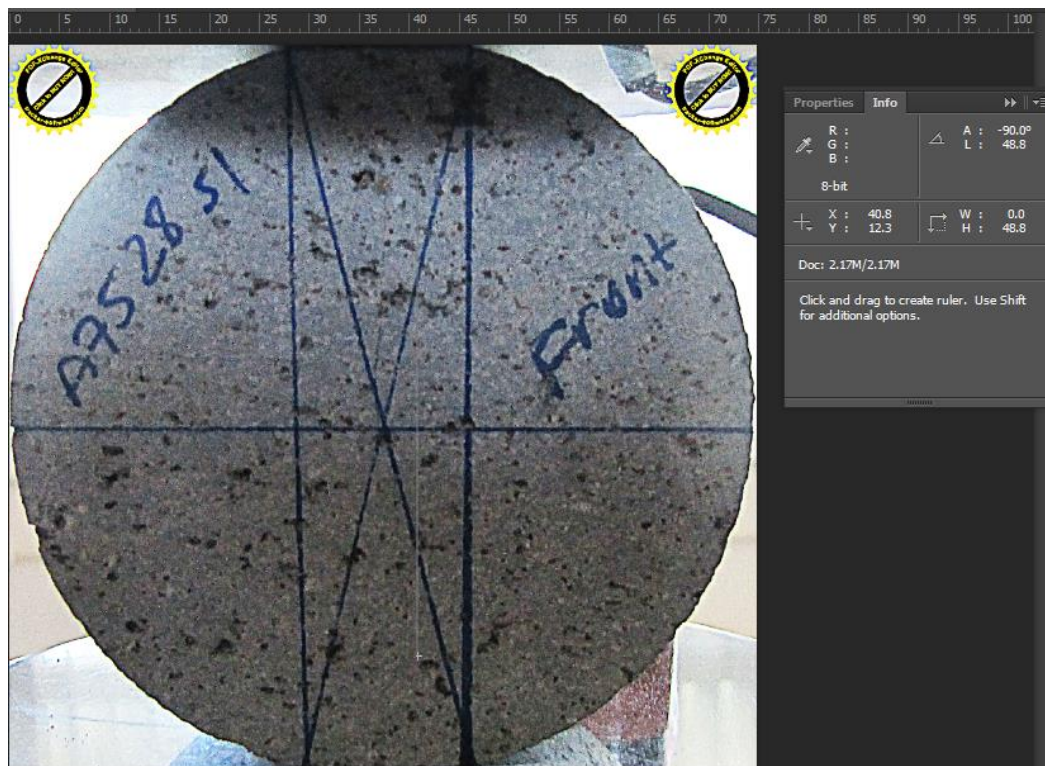

Figure 5. 2 Front view of FBD A7528s1 specimen with $2a_{ce}$=48.8 mm

5.2 Fracture toughness test results for Ankara andesite with a diameter of 100 mm

Six andesite core specimens of 100 mm diameter were prepared with a thickness around 67 mm. In machining the flat loading boundaries of the disks, loading angle was around 27° (0.471 in radians).

From FBD testing, P_{min},, K_{Ic}, stiffness values and critical crack lengths corresponding to loading angle were acquired. Stiffness values obtained from three different stages (Figure 5.3) , numerically evaluated and experimentally measured critical crack lengths are listed in Table 5.3. As seen in Table 5.3, the very slight difference between numerical and experimental critical crack length measurements occur. While the average a_{cn} value become 33.7 mm, the average a_{ce} measurement is 34.4 mm. Loading angle, Y_{max}, P_{min}, and K_{Ic} values are tabulated on Table 5.4. Due to the slight variations of the width of the flat loading ends and loading angle, Y_{max} parameter varies between 0.487 and 0.522.

Table 5. 3 Critical crack length comparison and stiffness values for 100 mm diameter FBD andesite specimens

Specimen Id	a_{cn} (mm)	a_{ce} (mm)	a_{cn}/R	a_{ce}/R	$k_{initial}$ (kN/mm)	k_{drop} (kN/mm)	k_{crack} (kN/mm)
A10028s1	33.2	34.9	0.66	0.69	297	465	76
A10028s2	33.2	33.0	0.66	0.66	394	6294	252
A10027s1	33.7	34.7	0.67	0.69	336	15983	246
A10027s2	33.7	34.5	0.67	0.69	374	6770	212
A10026s1	34.2	33.6	0.68	0.67	362	6286	256
A10026s2	34.2	35.7	0.68	0.71	341	12323	271
Average	**33.7±0.5**	**34.4±1.4**	**0.67±0.10**	**0.69±0.03**	**351±54**	**8718±7265**	**219±143**

Table 5. 4 Loading angle, Y_{max}, P_{min} and K_{IC} values of 100 mm diameter FBD andesite specimens

Specimen Id	2α (radians)	Y_{max}	P_{min} (kN)	K_{IC} (MPa $\sqrt{m}$)
A10028s1	0.489 (28°)	0.487	101.2	3.31
A10028s2	0.489 (28°)	0.487	106.4	3.45
A10027s1	0.471 (27°)	0.504	99.4	3.32
A10027s2	0.471 (27°)	0.504	104.0	3.50
A10026s1	0.454 (26°)	0.522	93.2	3.23
A10026s2	0.454 (26°)	0.522	93.8	3.25
Average	**0.471±0.0175**	**0.504±0.017**	**99.7±6.7**	**3.34±0.16**

Stiffness measured from the slope of load-displacement records of the tests can provide information about effect of brittleness on fracture energy or toughness for the rock types used in testing. Stiffness measured at initial loading stage, load drop stage, and stable crack propagation stage were obtained from the relevant slopes of force-displacement curves as seen in Figure 5.3 (a). The detailed view of stiffness values is illustrated for the cracking stage in Figure 5.3 (b).
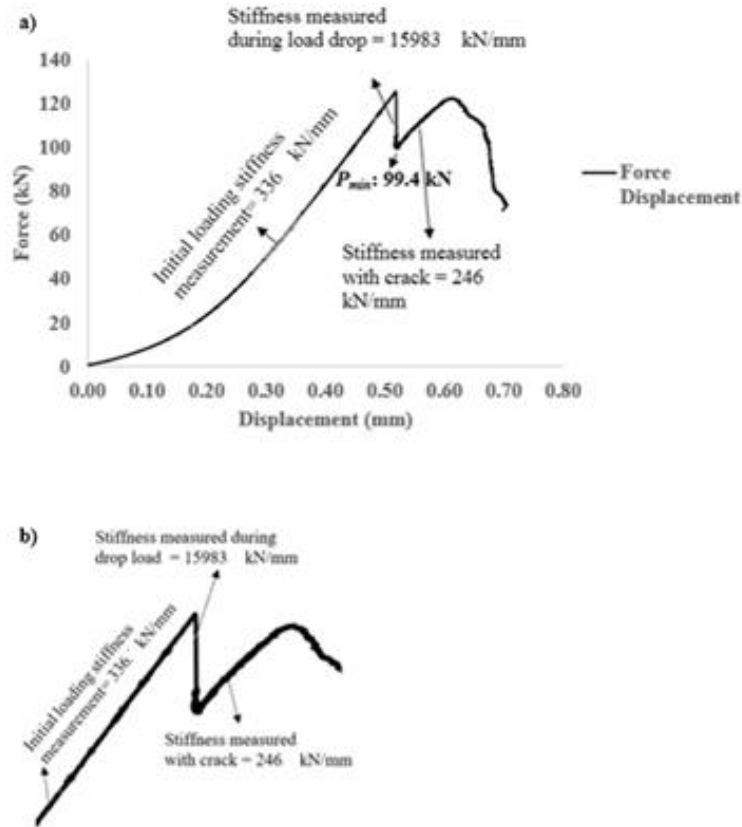
Figure 5. 3 (a) Force-displacement curve of a typical FBD test (b) detailed stiffness measurements at cracking stage (Specimen A10027s1)

The stiffness of 336 kN/mm at initial loading stage, stiffness of 15983 kN/mm in transition period from unstable crack growth to stable crack growth, namely when attained to minimum load and stiffness of 246 kN/mm measured with crack were illustrated in Figure 5.3(b). The highest amount of stiffness occurs when there is no crack after yielding. In other words, during first main crack formation, highest amount of energy releases in order to open new crack surfaces as related to stiffness matrix. After first crack formation, crack propagation and another new crack initiation happen at lower stiffness. Loss of stiffness with respect to initial loading can be explained by little cracks near

boundary or heterogeneity caused by void and crack growth during second raising within stable crack growth.

5.3 Fracture toughness test results for Afyon marble with a diameter of 75 mm

Four marble core specimens with a diameter of 75 mm were used in FBD testing. Its thickness was decreased to nearly 37.7 mm and loading angle in radians was set between 0.471 (27°) and 0.489 (28°). In Table 5.5, stiffness values, both numerical and experimental critical crack lengths are presented. The stiffness at load drop involves more variation than those at initial loading and cracking stages. Moreover, compared to andesite specimens, stiffness values are found more varied in marbles due to weakness, discontinuities. In Table 5.6, the fracture toughness value in average is obtained as 3.43 MPa$\sqrt{m}$. As shown in Figure 5.4, the photographic a_{ce} is calculated as 50.6 mm.

Table 5. 5 Critical crack length comparison and stiffness values for 75 mm diameter FBD marble specimens

Specimen Id	a_{cn} (mm)	a_{ce} (mm)	a_{cn}/R	a_{ce}/R	$k_{initial}$ (kN/mm)	k_{drop} (kN/mm)	k_{crack} (kN/mm)
M7528s1	24.7	25.3	0.66	0.68	359	7310	321
M7528s2	24.9	25.6	0.67	0.68	376	93602	330
*M7528s3	24.9	25.7	0.66	0.70	328	11131	295
M7528s4	25.0	26.3	0.67	0.68	323	20541	376
M7527s1	25.1	25.5	0.67	0.68	369	1421	351
M7527s2	25.1	26.3	0.67	0.70	361	24363	336
Average	**25.0±0.3**	**25.8±0.5**	**0.67±0.01**	**0.69±0.02**	**358±18**	**29448±64154**	**343±33**

Table 5. 6 Loading angle, Y_{max}, P_{min} and K_{IC} values of 75 mm diameter FBD marble specimens (* symbol represents the specimen with discontinuities and its results are not considered in calculation)

Specimen Id	2α (radians)	Y_{max}	P_{min} (kN)	K_{IC} (MPa $\sqrt{m}$)
M7528s1	0.489 (28°)	0.487	47.1	3.16
M7528s2	0.480 (28°)	0.495	49.6	3.39
*M7528s3	0.483 (28°)	0.492	34.5	2.32
M7528s4	0.477 (28°)	0.498	50.7	3.45
M7527s1	0.471 (27°)	0.504	51.6	3.55
M7527s2	0.471 (27°)	0.504	52.2	3.60
Average	**0.477±0.012**	**0.498±0.011**	**50.2±3.1**	**3.43±0.27**

According to fracture test results, fracture toughness values for both andesite and marble change with loading angle. At lower loading angle, P_{min} value and the material resistance against the crack propagation is greater.
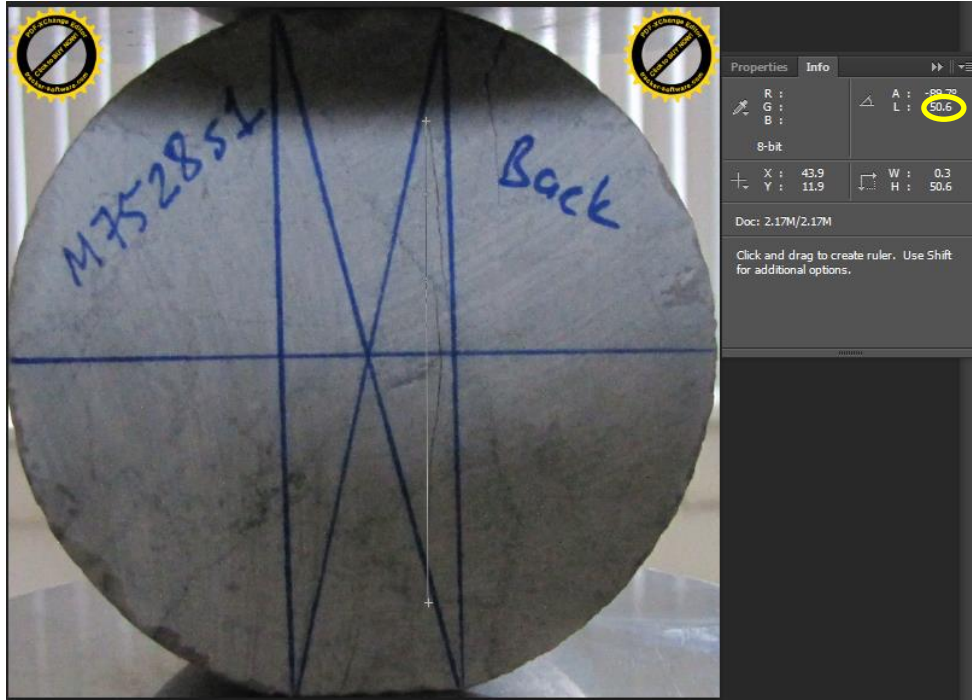
Figure 5. 4 Back view of FBD M7528s1 specimen with $2a_{ce}$=50.6 mm

5.4 Fracture toughness test results for Afyon marble with a diameter of 100 mm

Before testing of four marble core specimens having 100 mm in diameter, its thickness was restricted to approximately 67 mm. The loading angles in radians were kept between 0.460 (26°) to 0.513 (29°). This leads Y_{max} values to be held between 0.464 and 0.516. As seen in Table 5.8, the average value of K_{IC} is found as 3.04 MPa$\sqrt{m}$ and photographic $2a_{ce}$ of 66.5 mm is measured as shown in Figure 5.5.

Table 5. 7 Critical crack length comparison and stiffness values for 100 mm diameter FBD marble specimens

Specimen Id	a_{cn} (mm)	a_{ce} (mm)	a_{cn}/R	a_{ce}/R	$k_{initial}$ (kN/mm)	k_{drop} (kN/mm)	k_{crack} (kN/mm)
M10029s1	32.5	34.4	0.65	0.68	397	2894	544
M10028s1	33.1	34.1	0.66	0.68	476	7104	544
M10027s1	33.5	33.3	0.67	0.66	421	6584	512
M10026s1	34.0	34.0	0.68	0.68	513	69396	495
Average	33.3± 0.8	34.0± 0.7	0.66± 0.02	0.68±0 .02	452±62	21494±47902	524±29

Table 5. 8 Loading angle, Y_{max}, P_{min} and K_{IC} values of 100 mm diameter FBD marble specimens

Specimen Id	2α (radians)	Y_{max}	P_{min} (kN)	K_{IC} (MPa $\sqrt{m}$)
M10029s1	0.513 (29°)	0.464	75.5	2.34
M10028s1	0.493 (28°)	0.483	106.8	3.41
M10027s1	0.478 (27°)	0.497	83.6	2.74
M10026s1	0.460 (26°)	0.516	107.4	3.66
Average	0.486±0.027	0.490±0.026	93.3±17.8	3.04±0.70
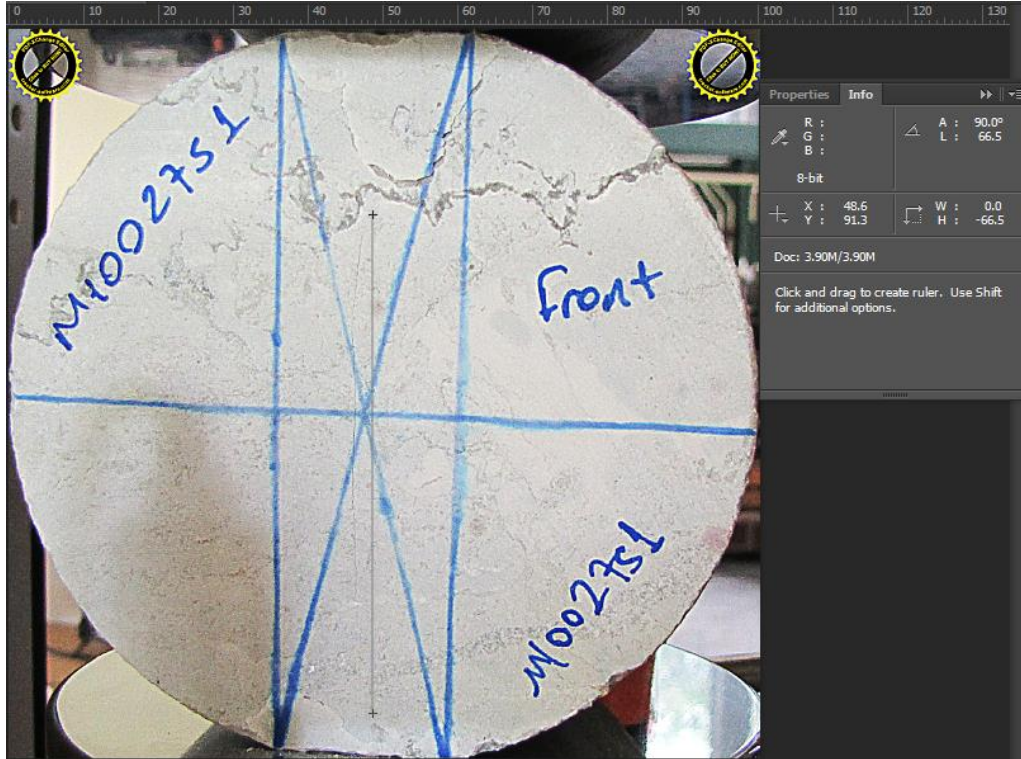
Figure 5. 5 Front view of FBD M10027s1 specimen with $2a_{ce}$=66.5 mm

5.5 Comparison of overall results

Results of FBD tests are collected in Table 5.9 for both andesite and marble together. Mode I fracture toughness K_{IC} results are tabulated for two different core sizes of 75 mm and 100 mm for both rocks.

According to Table 5.9, average mode I fracture toughness values for andesite and marble with a diameter of 75 mm are found as 2.58±0.34 MPa√m and 3.43±0.27 MPa√m while corresponding values for a larger diameter of 100 mm are acquired as 3.34±0.15 MPa√m in andesite and 3.04±0.70 MPa√m in marble. This shows that while a significant difference is available in andesite having 75 mm and 100 mm diameters, no visible change for both diameters is seen in marble.

Stiffness values at initial loading, load drop and crack growth in andesite are less than the corresponding values in marble. Considering stiffness, it can be said that marble is stiffer than andesite and when size gets larger, stiffness increases with a significant rate. This happens due to increase in energy release caused by crack growth.

At the optimal loading angle of 26°, experimentally measured and numerically computed critical crack lengths are around 25 mm for andesite and marble having 75 mm diameter while they are nearly 34 mm for both rocks with a diameter of 100 mm. Dimensionless experimental and numerical crack lengths at critical stage is found to be around 0.67 for andesite and marble having 75 mm and 100 mm in diameter. The results reveals that the consistency in measurements of critical crack length is provided, successfully.

Table 5. 9 Fracture test results for andesite and marble having 75 mm and 100 mm diameters

Core size	75 mm				100 mm			
Rock Type	K_{IC} (MPa $\sqrt{m}$)	$k_{initial}$ (kN/mm)	k_{drop} (kN/mm)	k_{crack} (kN/mm)	K_{IC} (MPa $\sqrt{m}$)	$k_{initial}$ (kN/mm)	k_{drop} (kN/mm)	k_{crack} (kN/mm)
Andesite	2.58± 0.34	215±7	4663±1636	155±36	3.34±0.15	351±54	8718±7265	219±143
Marble	3.43± 0.27	358±18	29448±64154	343±33	3.04±0.70	452±62	21494±47902	524±29
	a_{cn} (mm)	a_{ce} (mm)	a_{cn}/R	a_{ce}/R	a_{cn} (mm)	a_{ce} (mm)	a_{cn}/R	a_{ce}/R
Andesite	25.1± 0.6	25.5±2.1	0.67±0.02	0.68±0.06	33.7±0.5	34.4±1.4	0.67±0.10	0.69±0.03
Marble	25.0± 0.3	25.8±0.5	0.67±0.01	0.69±0.02	33.3±0.8	34.0±0.7	0.66±0.02	0.68±0.02

5.6 The discussion of size effect

In the past, Bazant et al. (1991) discussed the presence of size effect in tensile test upon splitting cylinder (Brazilian) concrete specimens. According to this experimental study, size effect existed and up to a definite critical diameter, failure stress agreed with the size effect law suggested by Bazant due to energy release induced by fracture growth. In Bazant's study, the size effect occured when crack length expanded with increasing specimen size and lower failure stress became adequate for breaking the material. In other words, strain softening around crack tip stimulated larger fracture process zone to form due to aggregate size of concrete. On the other hand, the size of process zone relative to specimen diameter diminishes for brittle specimens with a larger diameter as in the present study.

Size effect issue is disputed here over two rock types having 100 mm and 75 mm in diameter with FBD geometry. As seen from Table 5.10, the size effect on mode I fracture toughness is observed to be about 30% (3.34/2.58=1.295) for Ankara andesite in current study. When compared to Tutluoglu and Keles' results (2011), the size effect was observed to be about 36% (2.61/1.92=1.36) for Ankara andesite having 100 mm and 75 mm in diameter. It was realized that the compliance between both works is maintained for the similar andesite same material. The fracture toughness ratio (2.58/1.92=1.34) for 75 mm in diameter is highly close to counterpart (3.34/2.61=1.28) for 100 mm in diameter. This closeness proves the consistency within the homogeneity and geometry of material. In addition, these test results point out that the major reason of this is generated from the difference of Elastic Modulus between two distinct andesites, Based on this, while Elastic Modulus of andesite was obtained as 12 GPa from Tutluoglu and Keles' study (2011), corresponding value used in present study is 21.9 GPa.

On the other hand, fracture toughness values of marbles with two different diameters of 75 mm and 100 mm result in being rather similar and size effect wasn't observed as

104

expected due to the direction of discontinuities intervening or deflecting the loading conditions.

Also, the fracture toughness variation in marble with a large diameter was about 0.7 $MPa\sqrt{m}$ relatively higher than the variation of 0.15 $MPa\sqrt{m}$ in more homogenous andesite material. It might be said that when the size grows, more variation is encountered in materials exposed to large discontinuities allowing material matrix differentiation and color changes seen in even naked eye.

Table 5. 10 Mode I fracture toughness results of FBD test method for different diameters and similar rock types such as marble and andesite

Material Type	Number of tests	D (mm)	K_{IC} (MPa$\sqrt{m}$)	Source
Andesite	10	54	1.76±0.37	Tutluoglu and Keles (2011)
Marble	10	54	1.29±0.41	Tutluoglu and Keles (2011)
Andesite	5	75	1.92±0.42	Tutluoglu and Keles (2011)
Andesite	3	75	2.58±0.34	Present study
Marble	5	75	3.43±0.27	Present study
Andesite	6	100	3.34±0.15	Present study
Marble	4	100	3.04±0.70	Present study
Andesite	11	100	2.61±0.88	Tutluoglu and Keles (2011)

5.7 Investigation about BDT and FBD methods

In addition to the K_{IC} results of FBD specimens, an extensive investigation about K_{IC} value is conducted about BDT ones. For BDT tests, both andesite and marble having approximately 54 mm in diameter and 33 mm in thickness are used. The loading angle of these test specimens is taken as 0° and Y_{max} value is obtained as 5.418 for all Brazilian discs with a diameter of 54 mm as seen in Table 5.11. In this work, similar force-displacement curves are acquired on both rocks. According to Table 5.11, the average of P_{min} values becomes 18.46 kN for andesite whereas for marble, corresponding value is 22.55 kN. In accordance with this, average of K_{IC} values for both andesite and marble are 18.64 MPa$\sqrt{m}$ and 23.59 MPa$\sqrt{m}$, respectively. The $2a_{cn}$ is calculated as almost diameter value.

Table 5. 11 P_{min} and K_{IC} values of BDT specimens including both rocks under $2\alpha = 0°$.

Specimen Id	P_{min} (kN)	K_{IC} (MPa$\sqrt{m}$)
ADB1	17.5	18.21
ADB2	16.8	17.05
ADB3	21.1	20.67
Average	18.5	18.64
MB1	19.3	20.01
MB2	25.8	26.23
MB3	22.6	24.53
Average	22.6	23.59

According to the results of FBD specimens pertained to Tutluoglu and Keles' study (2011), loading angle affects fracture toughness values, greatly. While the average of K_{IC} values are 18.64 MPa$\sqrt{m}$ and 1.96 MPa$\sqrt{m}$ at loading angles of 0° and 19.3° for andesite in respective order, 23.59 MPa$\sqrt{m}$ and 1.29 MPa$\sqrt{m}$ at loading angles of 0° and 20.1°. This excessive amount of difference is the sign of the fact that existence of loading angle causes much lower stress redistribution around the crack tip than its absence. Another point of view is that since the loading device is used during indirect tensile loading, loading angle is taken as approximately 10° (ISRM, 1978). In this scenario, the average values of K_{IC} attain to 3.47 MPa$\sqrt{m}$ for andesite and 4.39 MPa$\sqrt{m}$ for marble. These comparative results indicate that loading angle is a major element for the steps of crack initiation and propagation.

CHAPTER 6

CONCLUSION

Flattened Brazilian disc testing method presents a straightforward, simple and accurate approach to measure mode I fracture toughness of rock. With compression applied at flat ends of core specimens, a tensile central crack is forced to initiate and propagate to the loaded flat ends. Shear effect along the crack might cause considerable variation in mode I fracture toughness. Mode II shearing effect is minimum along the crack at the center of the specimen geometry. Machining symmetric flattened lengths of equal length leads to crack initiation at the core of disc and minimizes shear effect, which might emerge due to irregular surfaces.

Considering the inverse relationship between crack formation and stiffness, stiffness computation was attained at two stages to exhibit the loss of strength. The trend of stiffness value measured at the instant of first central crack formation and sudden drop of load showed brittle fracturing. After primary crack formation, ductile fractures started to be visible.

When the stiffness values of both andesite and marble are evaluated, marble becomes stiffer than andesite. While interpreting fracture toughness results of both rocks and whether size effect is available or not, the relation between P_{min} and stiffness is taken into account.

Displacement controlled loading rate had to be adjusted properly to a slow level, especially around the critical state. Sampling rate of the data acquisition system was limited and the system was to catch sudden decreases and increases in the load and load-displacement slopes. Due to the rather high load increments in the early tests, invalid fracturing and uncertain load peaks occurred and experiments were repeated.

The fracture toughness results obtained from BDT and FBD tests showed that loading angle plays important role for a clear identification of crack initiation and propagation steps. In machining and preparing the flat loading boundaries, loading angle was applied around 26° resulted in relatively consistent mode I fracture toughness results. This loading angle was chosen as 26° (2α), because it was claimed that experimental and numerical critical crack lengths was agreed, well (Tutluoglu and Keles, 2011).

An improved SIF equation was generated to determine mode I fracture toughness of rocks having FBD geometry. This equation included wider range of loading angle (from 2° to 50°) than previous work did.

In mesh convergence study used for exploring an improved SIF equation, the optimum contour integral radius is found as 1.5 mm for the mesh size (A) between 3 mm and 5 mm whereas related radius is determined as 2 mm for the mesh size between 5 mm and 7 mm. This analysis provided a better SIF equation with a very high fitting quality.

In FBD testing, K_{IC} value related to andesite with a diameter of 100 mm was found as 3.34 MPa$\sqrt{m}$ whereas K_{IC} value pertained to andesite with a diameter of 75 mm was obtained as 2.58 MPa$\sqrt{m}$. The size effect is observed to be about 30% (3.34/2.58=1.295) for andesite. Size effect is caused by boundary influence on the crack tip fracture process zone. The closer the loaded boundary the lower the fracture toughness due to a larger plastic or process zone at the crack tip. Obviously, loaded boundary is closer to the central crack for 75 mm diameter specimens.

Fracture toughness values of marble having 100 and 75 mm diameters were 3.04 MPa$\sqrt{m}$ and 3.43 MPa$\sqrt{m}$, respectively. Standard deviations in the K_{IC} results were around 0.7 MPa$\sqrt{m}$ for 75 and 100 mm diameter marble samples. It was relatively higher than the variation of 0.15 MPa$\sqrt{m}$ compared to 100 mm andesite samples. It might be concluded that when the size grows, more variation is encountered in materials including discontinuities like marble samples used in this work.

For marble material, matrix ingredients differentiation and color changes can be seen in even with naked eye. Regarding the size effect, this causes contradictory difference in K_{IC} values of marble having 100 mm and 75 mm diameters. Therefore, no size effect can be identified due to random weaknesses and discontinuities intervening or deflecting the loading conditions.

6.1 Recommendations

An emprical equation or approach should be developed for the experimental critical crack length measurement of FBD specimen which is previously investigated. Also, experimental critical crack length for BDT test should be calculated at the point of local minimum load by following photographic procedure, so the question on the assurance about crack initiation from loading points is solved.

To reach a common point for FBD geometries, those with a wide spectrum of diameters should be subjected to compressive loading. These specimens should include the diameters of 42, 54, 125 mm for both andesite and marble. Moreover, more different rock types including sedimentary rocks like limestone and volcano-sedimentary tuff should be used to expand observations and evaluations about fracture behavior of them.

Apart from this, using similar numerical method, mode I fracture toughness formula should be derived for Brazilian disc. Furthermore, by conducting more experiments, the accuracy of this method can be controlled.

In further study, the size of fracture process zone should be investigated for these rock types under both BDT and FBD tests.

REFERENCES

ABAQUS Analysis User's Manual, Version 6.14 Documentation.

ABAQUS/CAE User's Manual, Version 6.14 Documentation.

ABAQUS, Inc., "*Modeling Fracture and Failure with ABAQUS*", 2006.

Akazawa, T., 1943. *New test method for evaluating internal stress due to compression of concrete (the splitting tension test) (Part 1)*. J. Japan Soc. Civil Eng.

Alvarez-Fernández M. I., González-Nicieza C., Prendes-Gero M.B., García-Menéndez J. R., Peñas-Espinosa J. C., Suárez-Domínguez F. J. *"Numerical analysis of the influence of sample stiffness and plate shape in the Brazilian test"*. DYNA, Vol. 82, Núm. 194, 2015.

Anderson TL (2005) *Fracture mechanics: fundamentals and applications*. CRC Taylor & Francis, New York

ASTM C 1421, "*Standard Test Method for Determination of Fracture Toughness of Advanced Ceramics at Ambient Temperatures*" Annual Book of Standards, Vol. 15.01 (American Society for Testing and Materials, West Conshohocken, PA, 2001) pp. 641-672.

Atkinson, C., Smelser, R.E. and Sanchez, J., "*Combined Mode Fracture via Cracked Brazilian Disk Test*", Int. J. Fracture, Vol. 18, No. 4, pp. 279-291, 1982.

Awaji, H. and Sato, S., "*Combined Mode Fracture Toughness Measurements by the Disk Test*", J. Eng. Mater. Tech. Trans. ASME, Vol. 100, No. 4, pp. 175-182, 1978.

Ayatollahi M.R., Alborzi M.J. "*Rock fracture toughness testing using SCB specimen*". In: 13th International Conference on Fracture; Beijing, China, 2013.

Ayatollahi MR, Akbardoost J. "*Size and geometry effects on rock fracture toughness: mode I fracture*". Rock Mech Rock Eng 2014; 47: 677–687.

Ayatollahi MR, Mahdavi E, Alborzi MJ, Obara Y. "*Stress intensity factors of semi-circular bend specimens with straight-through and chevron notches*". Rock Mech Rock Eng 2016;49 (4):1161–72.

Bazant, Z.P. and Pfeiffer P.A., "*Determination of Fracture Energy from Size Effect and Brittleness Number*", ACI, Materials Journal, vol.84, pp. 463-480, 1987.

Bazant, Z.P., and Kazemi M.T., "*Size Effect of Fracture in Ceramics and Its Use to Determine Fracture Energy and Effective Process Zone Length*", Journal of American Ceramic Society, vol. 77, no. 7, pp.1841-1853, 1990.

Bazant, Z. P.; Kazemi, M. T.; Hasegawa, T. y Mazars, J.: "*Size effect in Brazilian split-cylinder test. Measurement and analysis*", ACI Material Journal, vol. 88 (1991), pp. 325-332.

Bazant, Z.P., Daniel, I., and Li, Z., "*Size Effect and Fracture Characteristics of Fiber-Composite Laminates*", Report Civil Engng Northwestern University, Evanson, 1995.

Bažant, Z.P., Daniel, I.M., and Li, Zhengzhi (1996). *Size effect and fracture characteristics of composite laminates*. ASME Journal of Engineering. Materials and Technology 118(3), 317–324.

Carneiro, F.L.L.B., 1943. *A new method to determine the tensile strength of concrete*. In: Proceedings of the 5th Meeting of the Brazilian Association for Technical Rules, 3d. Section, 16 September 1943, pp. 126–129 (in Portuguese).

Chang, S. H., Chung-In Lee, Jeon, S., "*Measurement of rock fracture toughness under modes I and II and mixed-mode conditions by using disc-type specimens*", Engineering Geology, Vol. 66, pp. 79–97, 2002.

Chin-Teh Sun, Zhihe Jin, 2012. "*Fracture Mechanics*". Academic Press.

Chong, K.P. and Kuruppu, M. D., "*New Specimen for Fracture Toughness Determination of Rock and Other Materials*", Int.J. Frac. Vol.26, pp. 59 − 62, 1984.

Chong, K.P, Kuruppu, M.D. and Kuszmaul, J.S., "Fracture toughness determination of layered materials", Eng. Fract. Mech., Vol. 28, pp. 55-65, 1987.

Dwivedi, R.D., Soni, A.K., Goel, R.K. and Dube A.K., "*Fracture Toughness of Rocks Under Sub-Zero Temperature Conditions*", Int. J. Rock Mech. Min. Sci., Technical Note, Vol. 37, pp. 1267-1275, 2000.

Inglis, C.E., "*Stresses in A Plate Due to The Presence of Cracks and Sharp Corners*", Trans. Inst. Naval Archit., Vol.55, pp.219-230, 1913.

Irwin GR. *Fracture dynamics. Fracturing of metals*. Cleveland, OH: American Society for Metals; 1948. p. 147–66.

Iqbal, M.J. and Mohanty, B., "*Experimental Calibration of Stress Intensity Factors of the ISRM Suggested Cracked Chevron-Notched Brazilian Disc Specimen Used for Determination of Mode-I Fracture Toughness*", Int. J. Rock Mech. Min. Sci., Technical Note, Vol. 43, pp. 1270–1276, 2006.

Fowell, R.J. and Xu, C., "*The cracked Chevron Notched Brazilian Disk Test-Geometrical Considerations for Practical Rock Fracture Toughness Measurement*", Preprint Proc. 34th U.S. Rock Mech. Symp., pp. 657-660, 1993.

Fowell, R.J., "*ISRM Commission on Testing Methods: Suggested Method for Determining Mode I Fracture Toughness Using Cracked Chevron Notched Brazilian Disc (CCNBD) Specimens*", Int. J. Rock Mech. Min. Sci. and Geomech. Abstr., Vol. 32, No. 1, pp. 57-64, 1995.

Fowell, R.J., Xu, C. and Dowd, P.A., "*An Update on the Fracture Toughness Testing Methods Related to the Cracked Chevron-Notched Brazilian Disk (CCNBD) Specimen*", Pure and Applied Geophysics, Vol. 163, pp. 1047-1057, 2006.

Funatsu T, Shimizu N, Kuruppu M, Matsui K. "*Evaluation of mode I fracture toughness assisted by the numerical determination of K-resistance*". Rock Mech Rock Eng 2015;48: 143–57.

Griffith, A.A., "*The Phenomena of Rapture and Flow in Solids*", Phil. Trans. Roy. Soc. of London, Vol. A221, pp. 163-198, 1920/1921.

Griffith, A.A., "*The Theory of Rupture*", Proc. of First Int. Cong. Appl. Mech., pp. 53-64, 1924.

Guo, H., Aziz, N.I. and Schmidt, L.C., "*Rock Fracture-Toughness Determination by the Brazilian Test*", Engineering Geology, Vol. 33, pp. 177-188, 1993.

Hondros, G., 1959. *The evaluation of Poisson's ratio and the modulus of materials of a low tensile resistance by the Brazilian (indirect tensile) test with particular reference to concrete*. Aust. J. Appl. Sci. 10, 243–268.

H.P. Rossmanith, "*Rock Fracture Mechanics*", Springer-Verlag, Wien, New York (1983)

Huang, Y. G., Wang, L. G., Lu, Y. L., Chen, J. R., & Zhang, J. H. (2014). *Semi-analytical and numerical studies on the flattened Brazilian splitting test used for measuring the indirect tensile strength of rocks. Rock Mechanics and Rock Engineering*. doi:10.1007/s00603-014-0676-8

ISRM, "*Suggested Methods for Determining Tensile Strength of Rock Materials*", Int. J. Rock Mech. Min. Sci. & Geomech. Abstr., Vol. 15, pp. 99-103, 1978.

Kaklis, K.N., Agioutantis, Z., Sarris, E. and Pateli, A., "*A Theoretical and Numerical Study of Discs with Flat Edges under Diametral Compression (Flat Brazilian Test)*", 5th GRACM International Congress on Computational Mechanics, Limassol, 2005.

Keles C, Tutluoglu L (2011). *Investigation of proper specimen geometry for mode I fracture toughness testing with flattened Brazilian disc method*. Int. J. Fract. 169(1):61-75.

Khan, K. and Al-Shayea, N. A., "*Effect of Specimen Geometry and Testing Method on Mixed Mode I-II Fracture Toughness of a Limestone Rock from Saudi Arabia*", Rock Mech. Rock Engng., Vol. 33, pp. 179-206, 2000.

Kobayashi, Hideo, Onoue, Hisahiro, Brittle Fracture of Liberty Ships, March,1943.

Krishnan, G.R., Zhao, X.L., Zaman, M. and Roegiers, J.C., "*Fracture Toughness of a Soft Sandstone*", Int. J. of Rock Mech. Min. Sci., Vol. 35, pp. 695-710, 1998.

Kuruppu, M. D., Obara, Y., Ayatollahi, M.R., Chong, K.P.,& Funatsu, T. (2015) *ISRM-suggested method for determining the mode I static fracture toughness using semi-circular bend specimen. In the ISRM Suggested Methods for Rock Characterization, Testing and Monitoring* : 2007-2014, 107-114. Springer International Publishing

Libatskii, L.L. and Kovichik, S.E., "*Fracture of Discs Containing Cracks*", Soviet Materials Science, Vol. 3, pp. 334-339, 1967.

Lim, I.L., Johnston, I.W., Choi, S.K., "*Stress Intensity Factors for Semi-circular Specimens Under Three-Point Bending*", Eng. Fract. Mech., Vol.44 pp.363-382, 1993.

Lim, I.L., Johnston, I.W., Choi, S.K., Boland, J.N., "*Fracture Testing of A Soft Rock with Semi-circular Specimens under Three-point Bending*", Part 1-2, Int. J. Rock Mech. & Min. Sci. and Geomech. Abstr., Vol.31, pp.185-212, 1994.

MTS Series 793 Controller Overview, 2011

Ouchterlony, F., "*ISRM Commission on Testing methods; Suggested Methods for determining fracture toughness of rock*", Int. J. Rock Mech. Min. Sci. & Geomech. Abstr., Vol. 25, pp. 71-96, 1988.

Proveti, J.R.C. and Michot, G., "*The Brazilian Test: A Tool for Measuring the Toughness of a Material and Its Brittle to Ductile Transition*", Int. J. Fract., Vol.139, pp. 455-460, 2006.

Rice, J.R., "*A path independent integral and the approximate analysis of strain concentration by notches and cracks*", J. App. Mech., Vol. 35, pp. 379-386, 1968.

Shetty, D.K., Rosenfield, A.R. and Duckworth, W.H., "*Fracture Toughness of Ceramics Measured By A Chevron Notched Diametral Compression Test*", J. Am. Ceram.Soc., Vol. 68, pp. c325-c443, 1985.

Shukla, A. (2005). *Practical Fracture Mechanics in Design. Second Edition.* Marcel Dekker.

Singh R.N. and Sun G.X., "*An investigation into factors affecting fracture toughness of coal measures sandstone*", J. Mines, Metals & Fuels, pp. 11I-118, 1990.

Srawley, J.E., "*Wide Range Stress Intensity Factor Expressions for ASTM E399 Standard Fracture Toughness Specimens*", Int. J. Fract., Vol.12, pp. 475 – 476, 1976.

Wang Ke Jen, Hsu Chi Lin and Kao Hua, "*Calculation Of Stress Intensity Factors For Combined Mode Bend Specimens*", Advances in Research on the Strength and Fracture of Materials, Editor D:M.R. Taplin, vol 4 Fracture and Society, ICF4, Canada, Waterloo, 1977.

Wang, Q.Z. and Xing, L., "*Determination of Fracture Toughness KIC by Using the Flattened Brazilian Disk Specimen for Rocks*", Eng. Fract. Mech., Vol. 64, pp. 193-201, 1999.

Wang, Q.Z., Jia, X.M., Kou, S.Q., Zhang, Z.X. and Lindqvist, P.A., "*The Flattened Brazilian Disc Specimen Used for Testing Elastic Modulus, Tensile Strength and Fracture Toughness of Brittle Rocks: Analytical and Numerical Results*", Int. J. of Rock Mech. Min. Sci., Vol. 41, pp. 245-253, 2004.

Wang, Q.Z. and Wu, L.Z., "*The Flattened Brazilian Disc Specimen Used For Determining Elastic Modulus, Tensile Strength and Fracture Toughness of Brittle Rocks: Experimental Results*", Int. J. Rock Mech. Min. Sci., Vol. 41, No. 3, pp. 1-5, 2004.

Tada, H., Paris, P.C. and George, R.I., "*The Stress Analysis of Cracks Handbook*", ASME Press, New York, 2000.

Timoshenko, S.P. and Goodier, J.N., "*Theory of Elasticity*". 3rd Edition, Mc Graw-Hill, New York, 1970.

Tutluoglu T and Keles C., *"Mode I Fracture Toughness Determination with Straight Notched Disk Bending Method"*, Int.J.Rock.Mech. & Min.Sci., Vol.48, pp. 1248 – 1261, 2011.

Westergaard. H.M., "*Stresses at a crack, size of the crack and the bending of reinforced concrete*", Prov. American Concrete Institute, Vol.30, pp. 93-102, 1934.

Whittaker, B.N., Singh, R.N., Sun, G., "*Rock Fracture Mechanics-Principles, Design and Applications*", Elsevier, Amsterdam, 1992.

APPENDIX A

FORCE-DISPLACEMENT CURVES
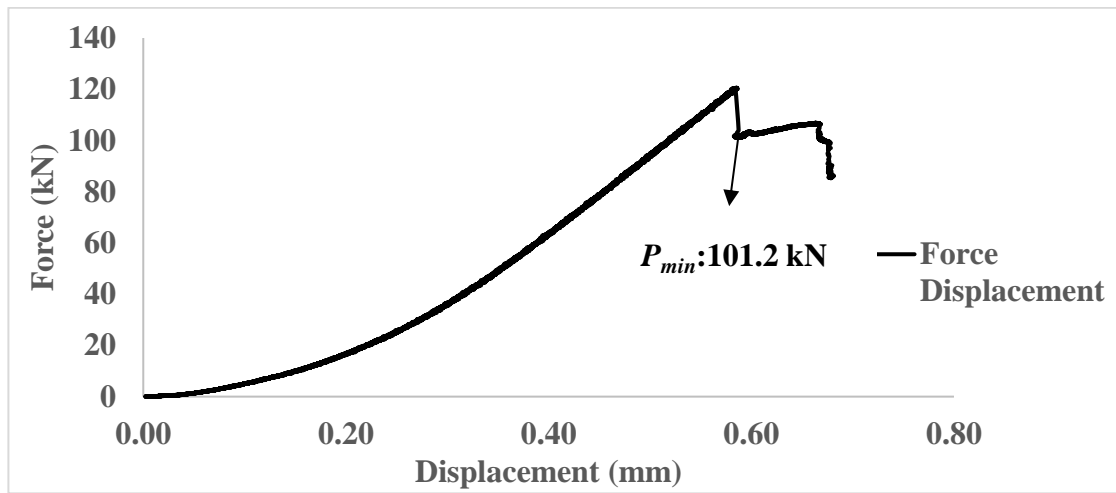
Figure A. 1 Force-displacement curve of A10028s1specimen
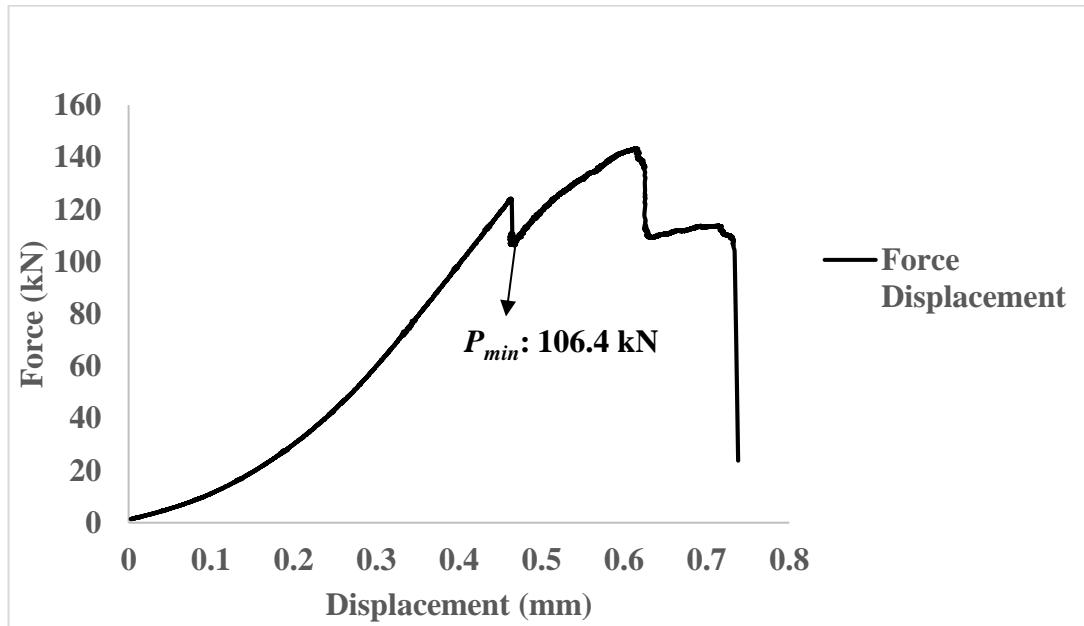
Figure A. 2 Force-displacement curve of A10028s2specimen
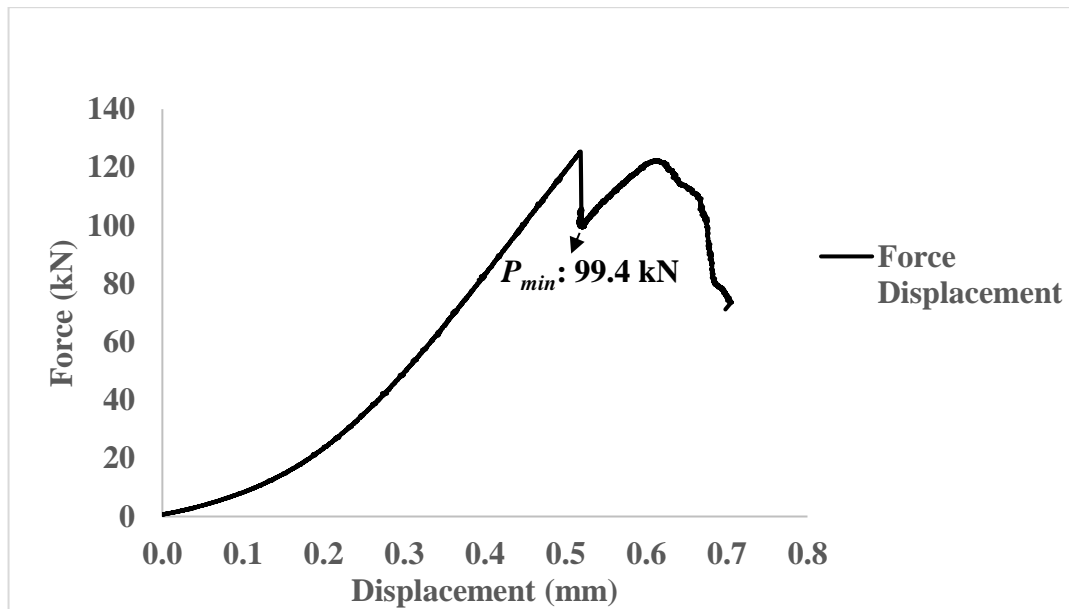
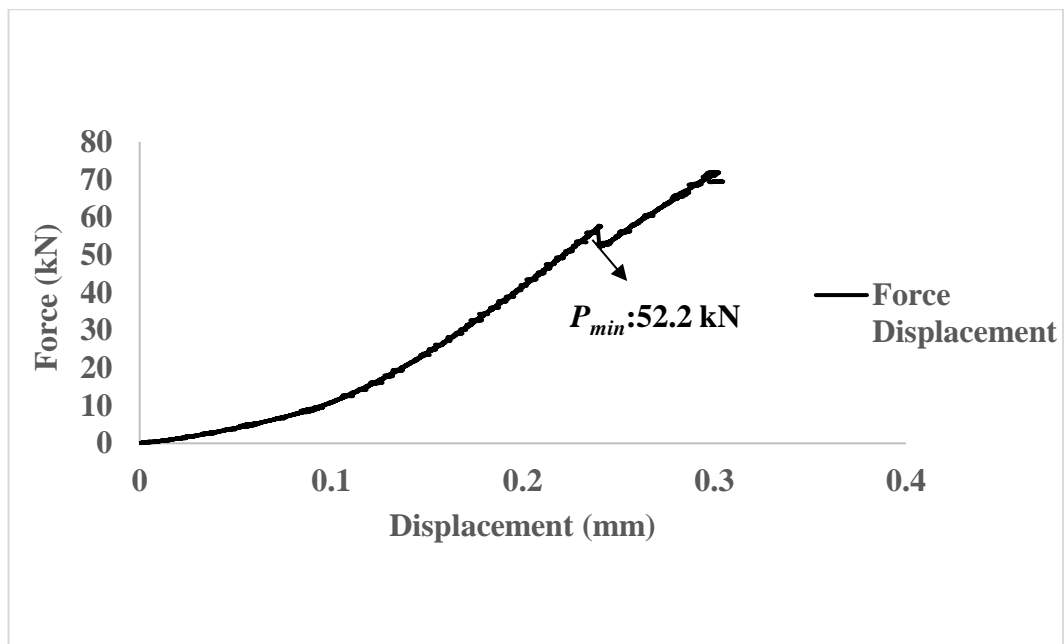

Figure A. 3 Force-displacement curve of A10027s1 specimen
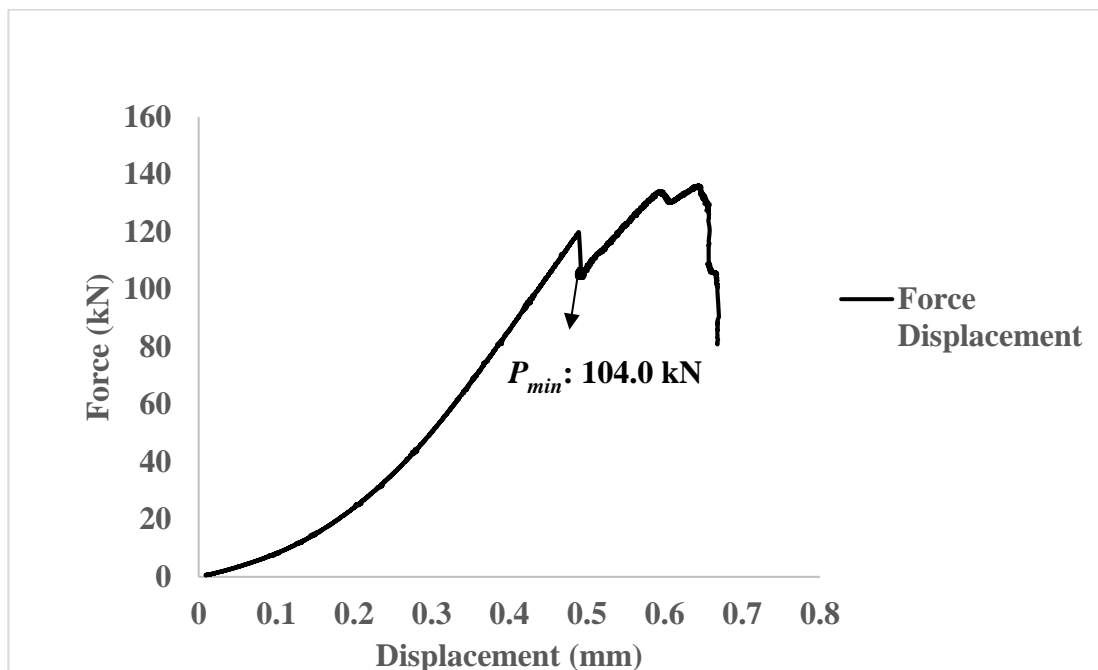
Figure A. 4 Force-displacement curve of A10027s2 specimen
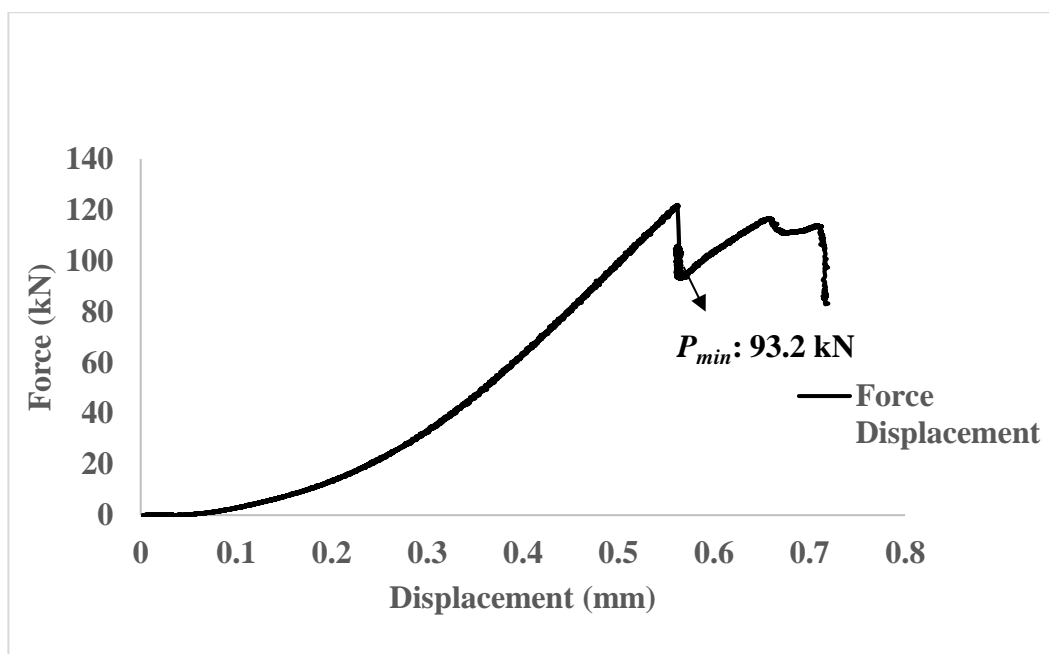
Figure A. 5 Force-displacement curve of A10026s1 specimen
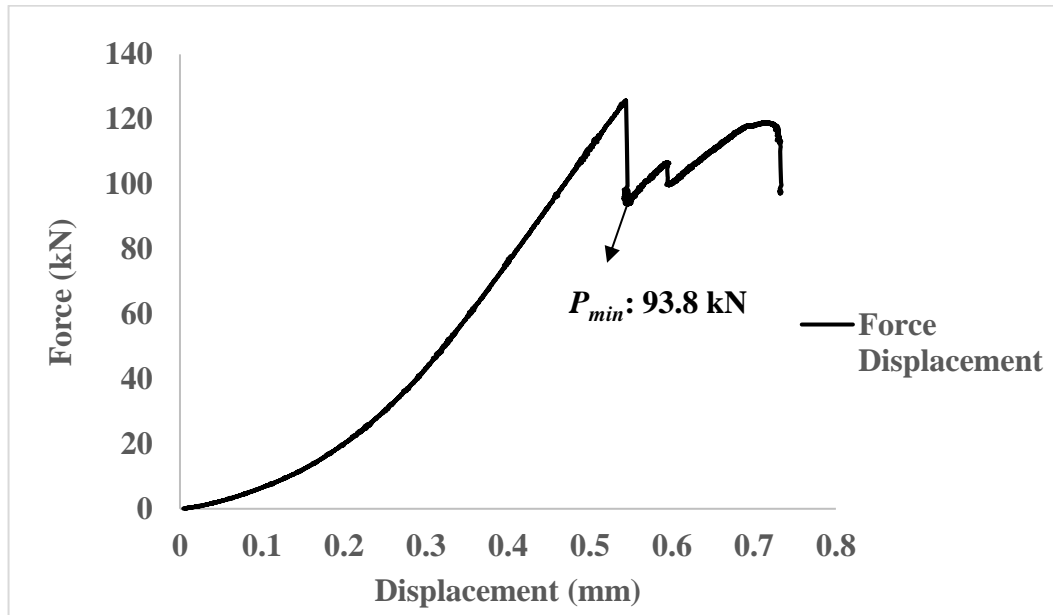
Figure A. 6 Force-displacement curve of A10026s2 specimen
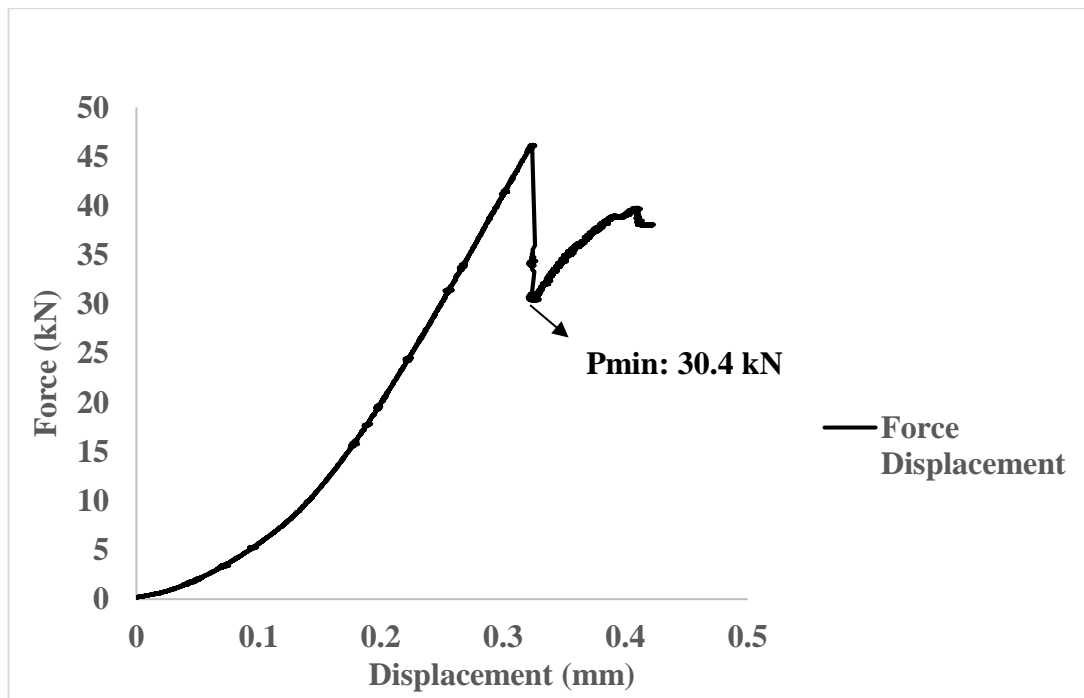
Figure A. 7 Force-displacement curve of A7525s1 specimen
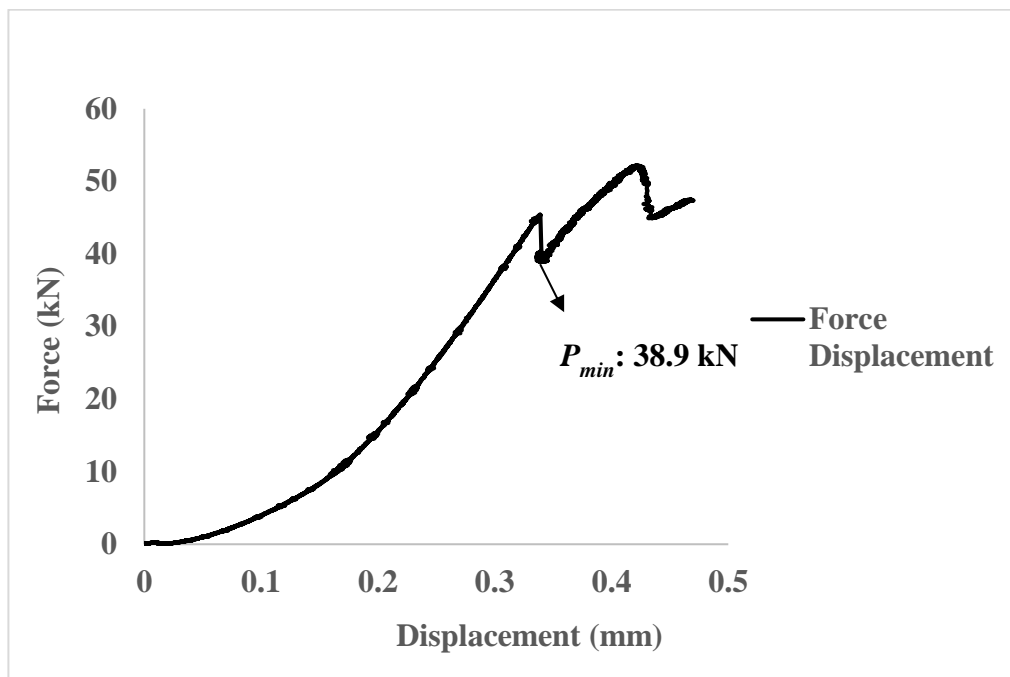
Figure A. 8 Force-displacement curve of A7527s1 specimen
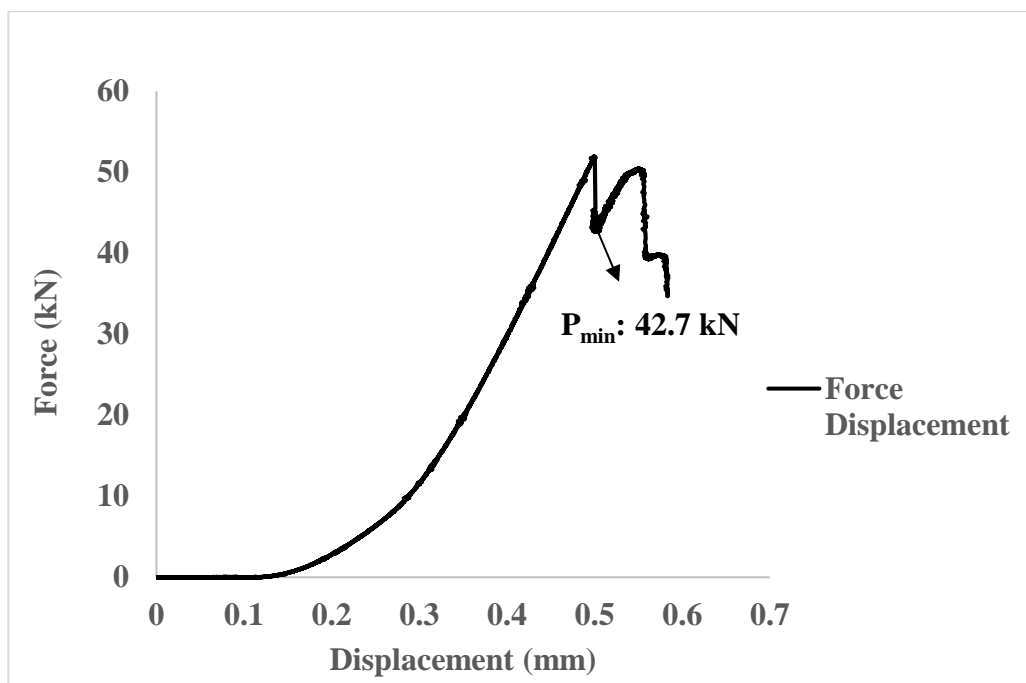
Figure A. 9 Force-displacement curve of A7528s1 specimen
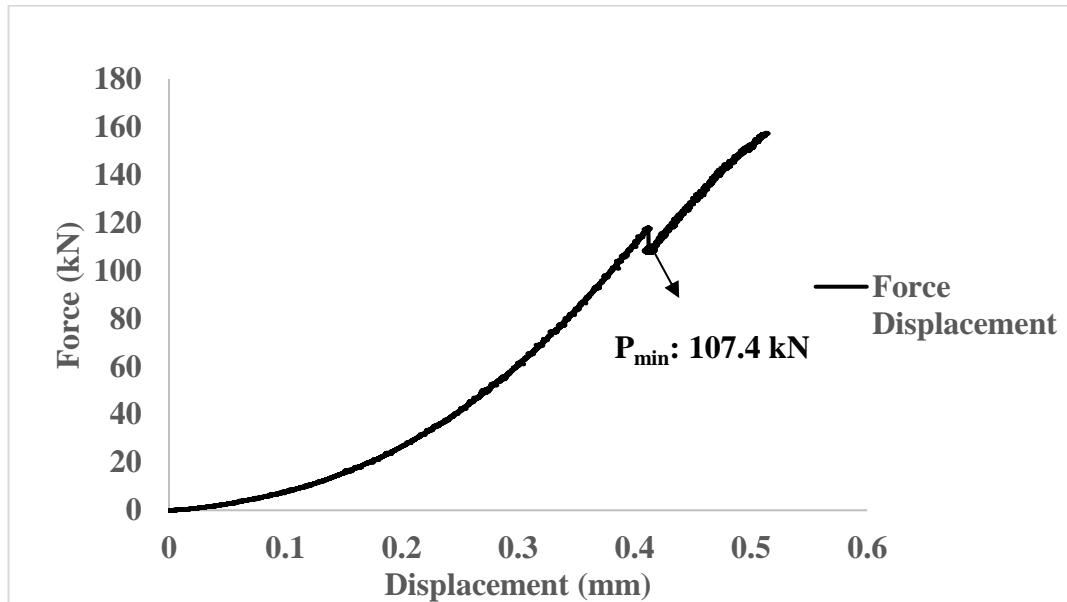
Figure A. 10 Force-displacement curve of M10026s1 specimen
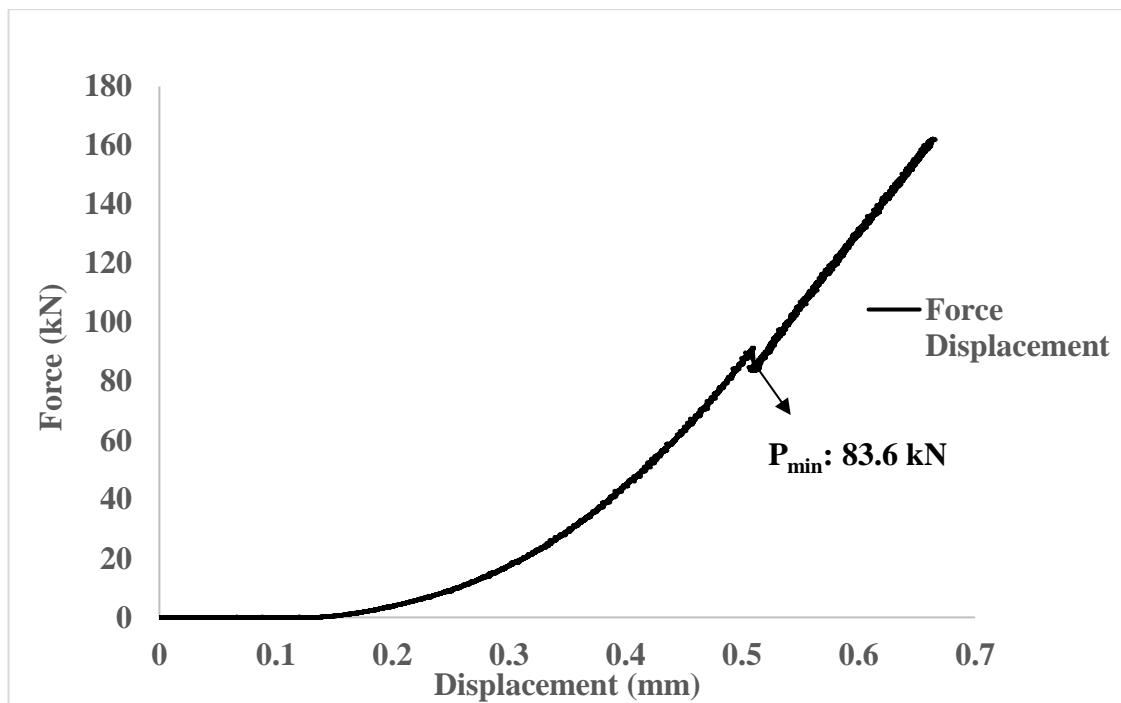
Figure A. 11 Force-displacement curve of M10027s1 specimen
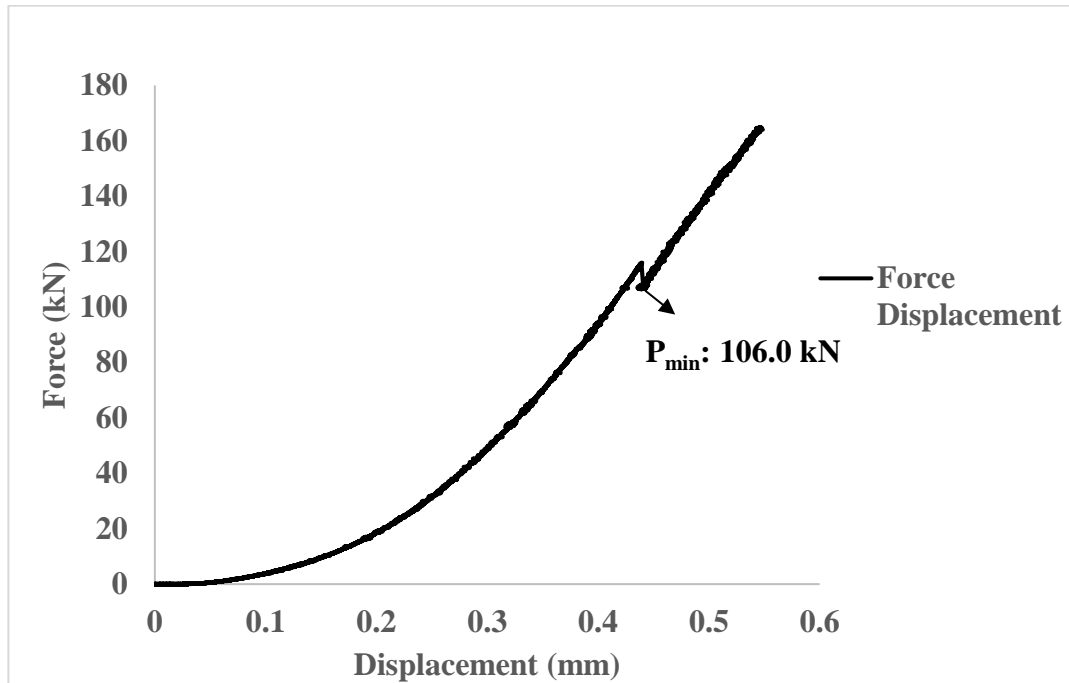
Figure A. 12 Force-displacement curve of M10028s1 specimen
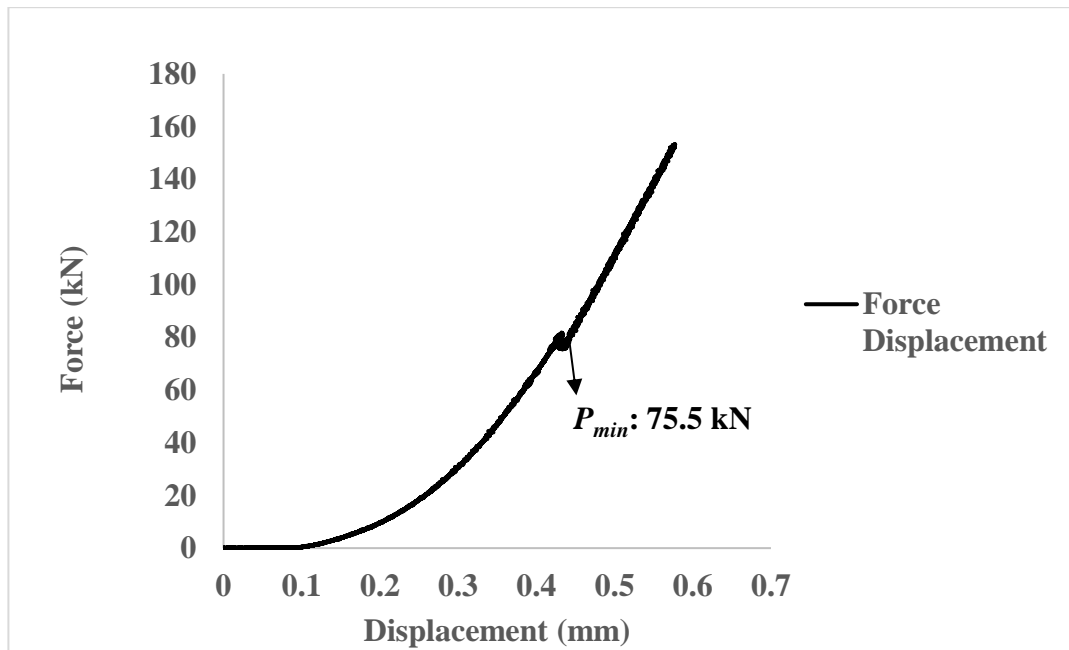
Figure A. 13 Force-displacement curve of M10029s1 specimen
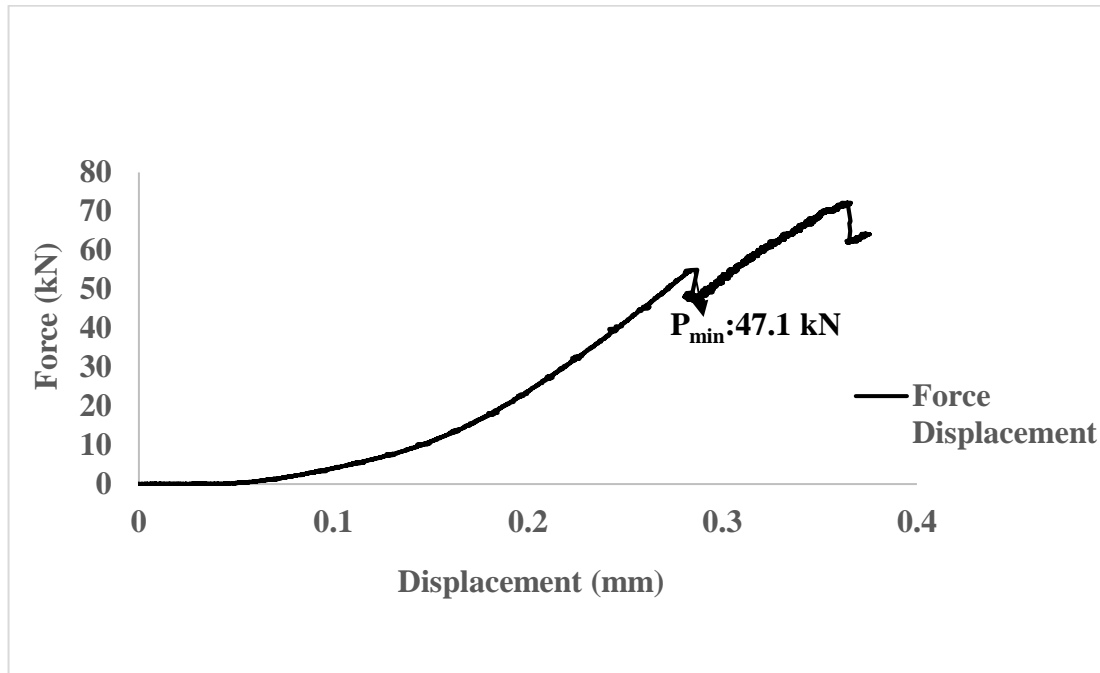
Figure A. 14 Force-displacement curve of M7528s1 specimen
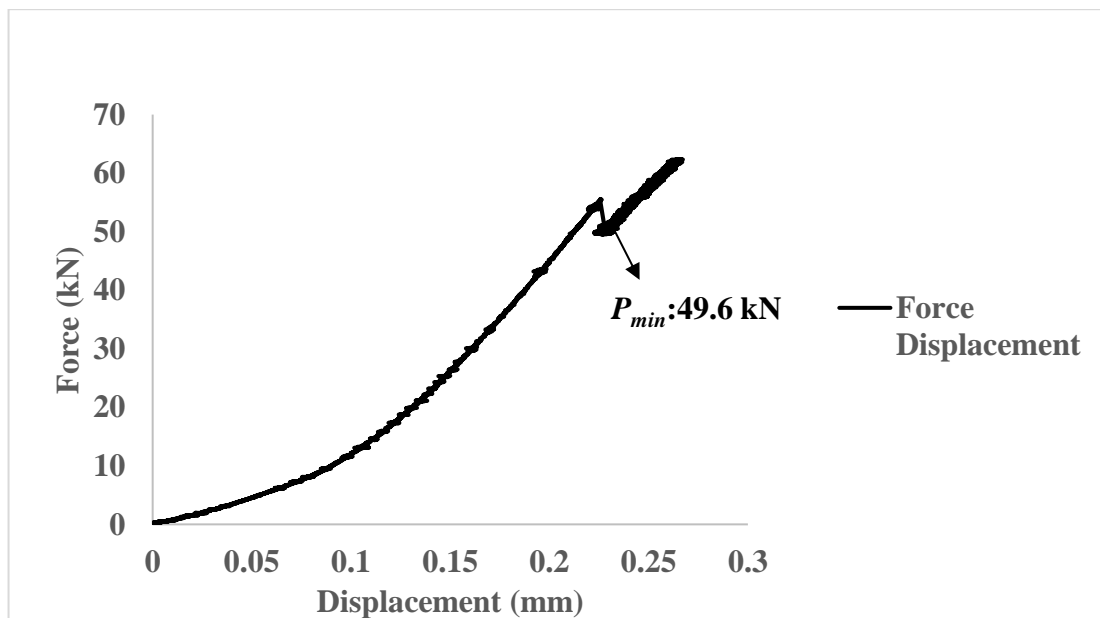
Figure A. 15 Force-displacement curve of M7528s2 specimen
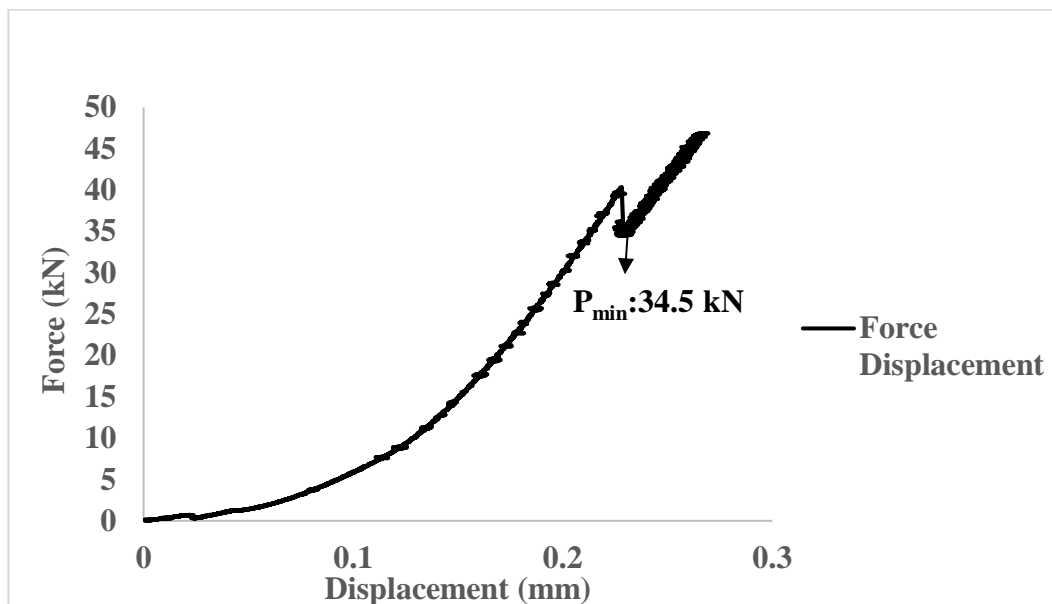
Figure A. 16 Force-displacement curve of *M7528s3 specimen
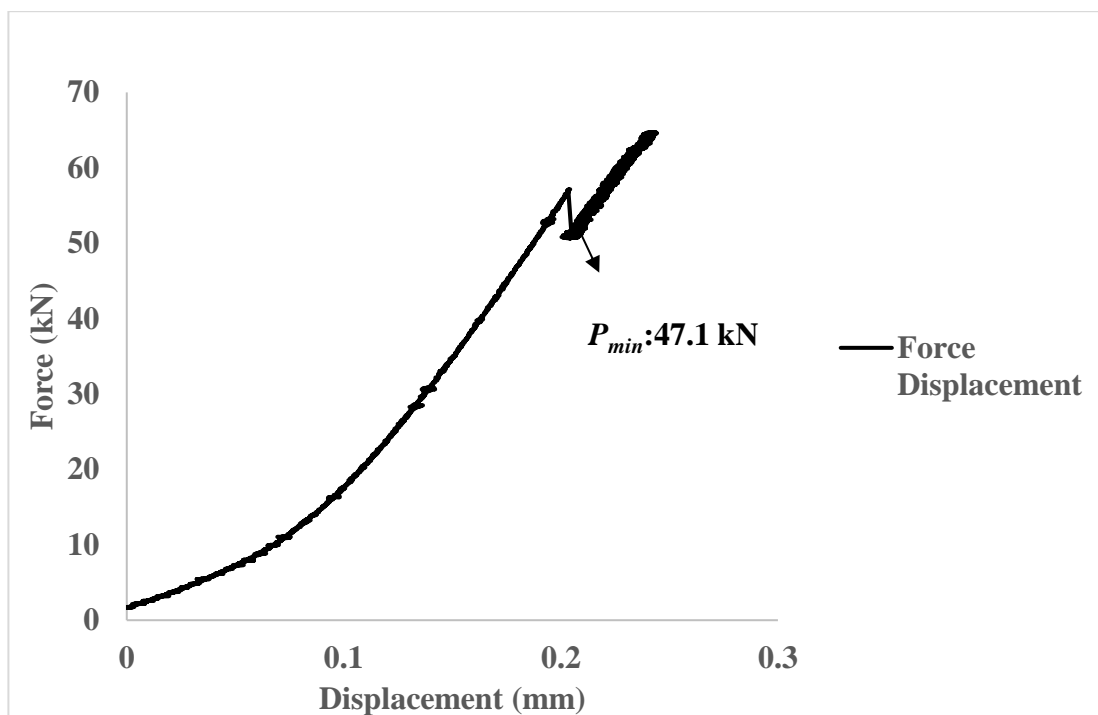
Figure A. 17 Force-displacement curve of M7528s4 specimen
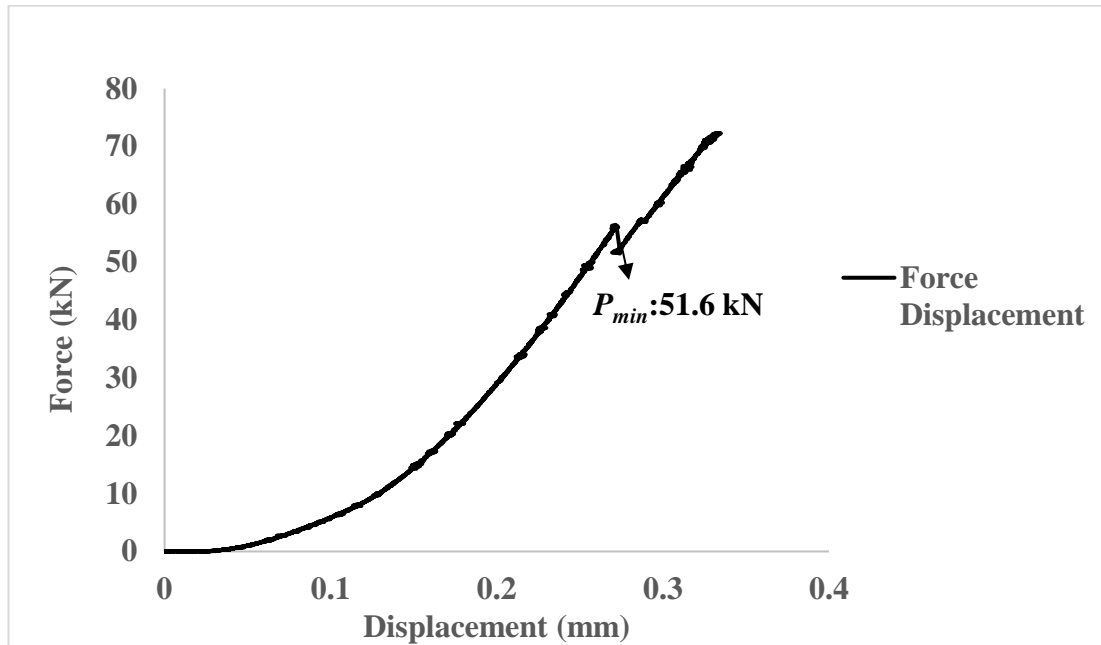
Figure A. 18 Force-displacement curve of M7527s1 specimen

Figure A. 19 Force-displacement curve of M7527s2 specimen

APPENDIX B

SPECIMEN PHOTOGRAPHS AFTER EXPERIMENTAL STUDY
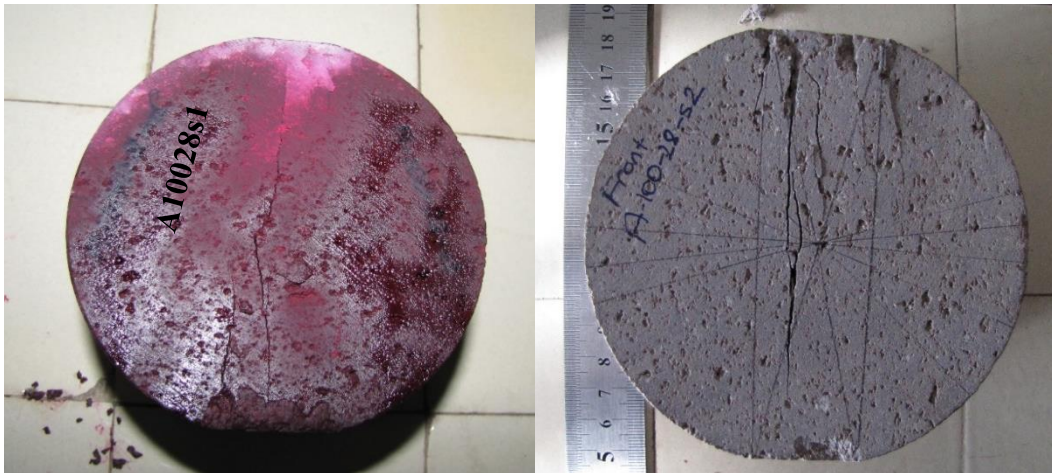
Figure B. 1 Two andesite specimens with a diameter of 100 mm after FBD tests
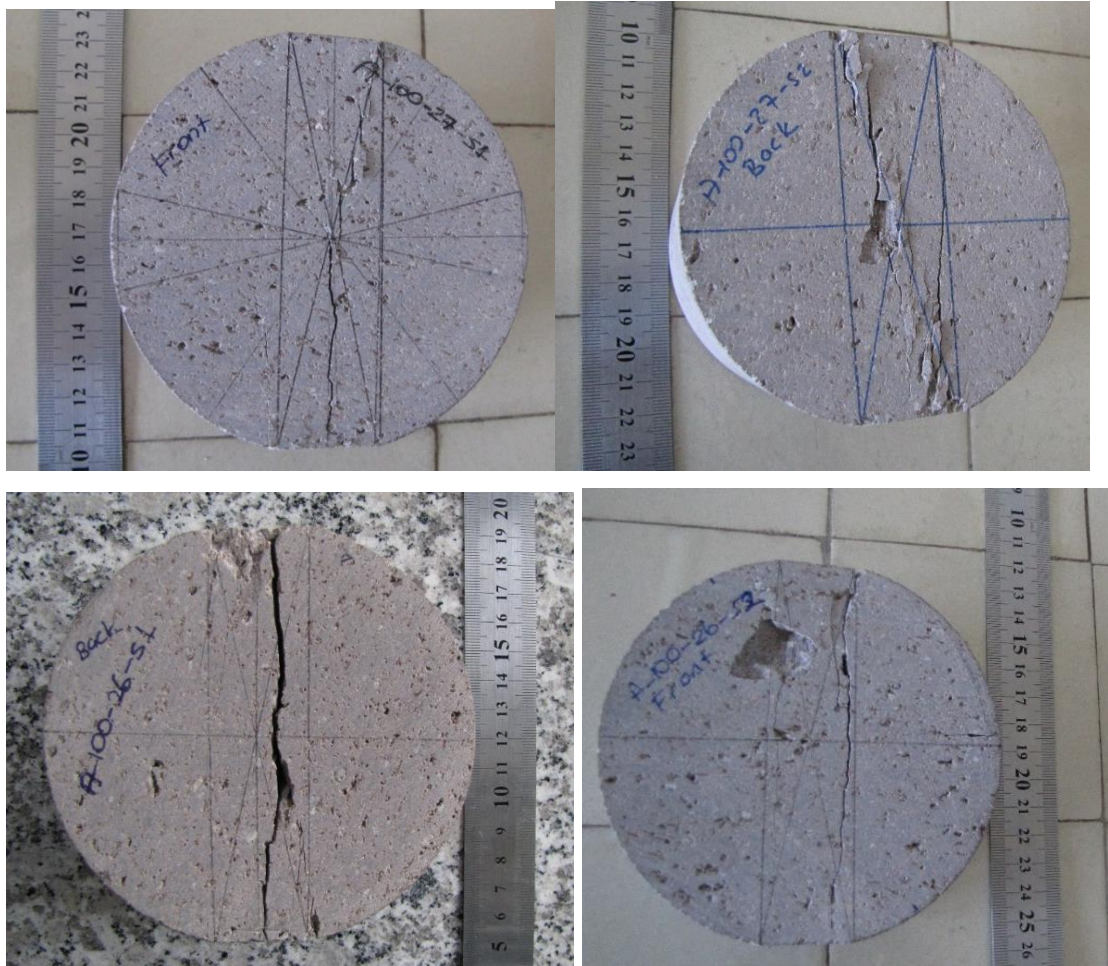
Figure B. 2 Four andesite specimens with a diameter of 100 mm after FBD tests
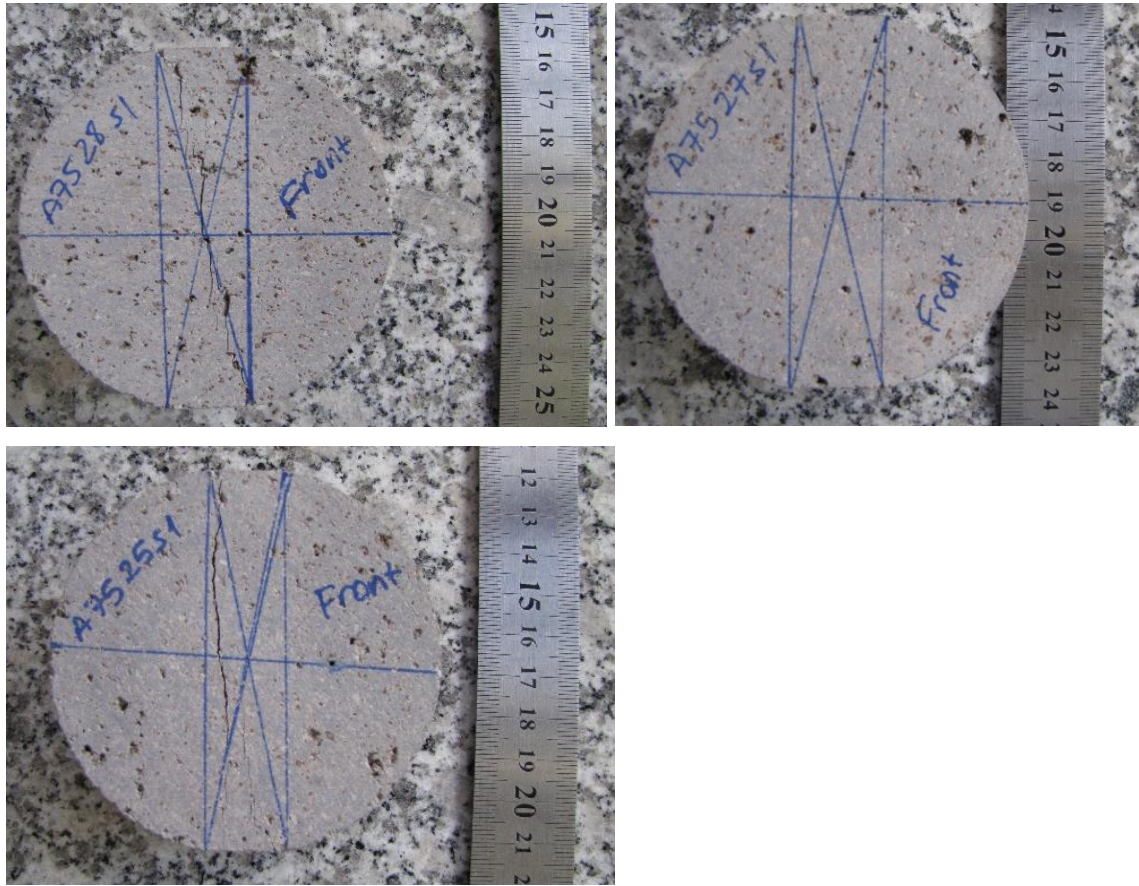
Figure B. 3 Three andesite specimens having 75 mm in diameter after FBD tests
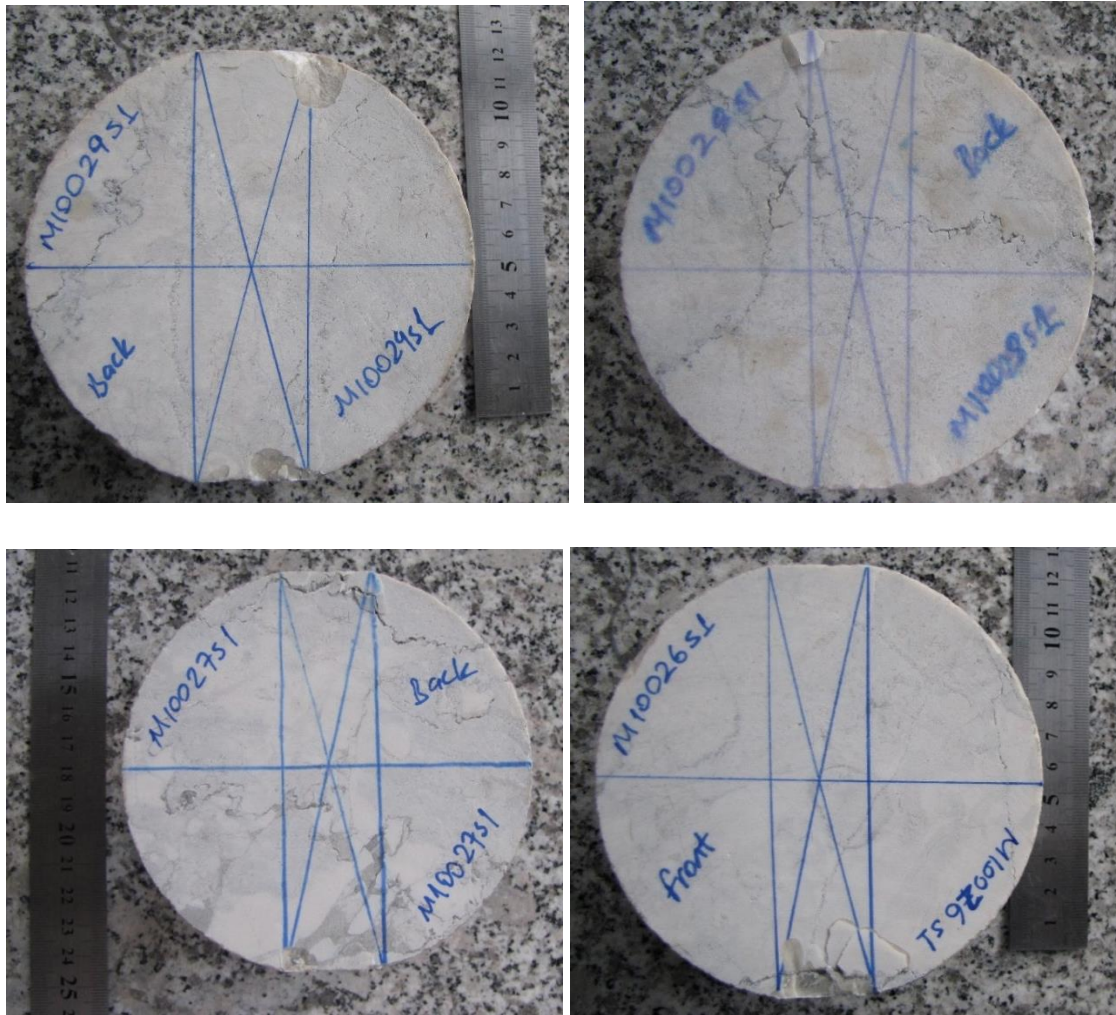
Figure B. 4 Four marbles with a diameter of 100 mm after FBD tests
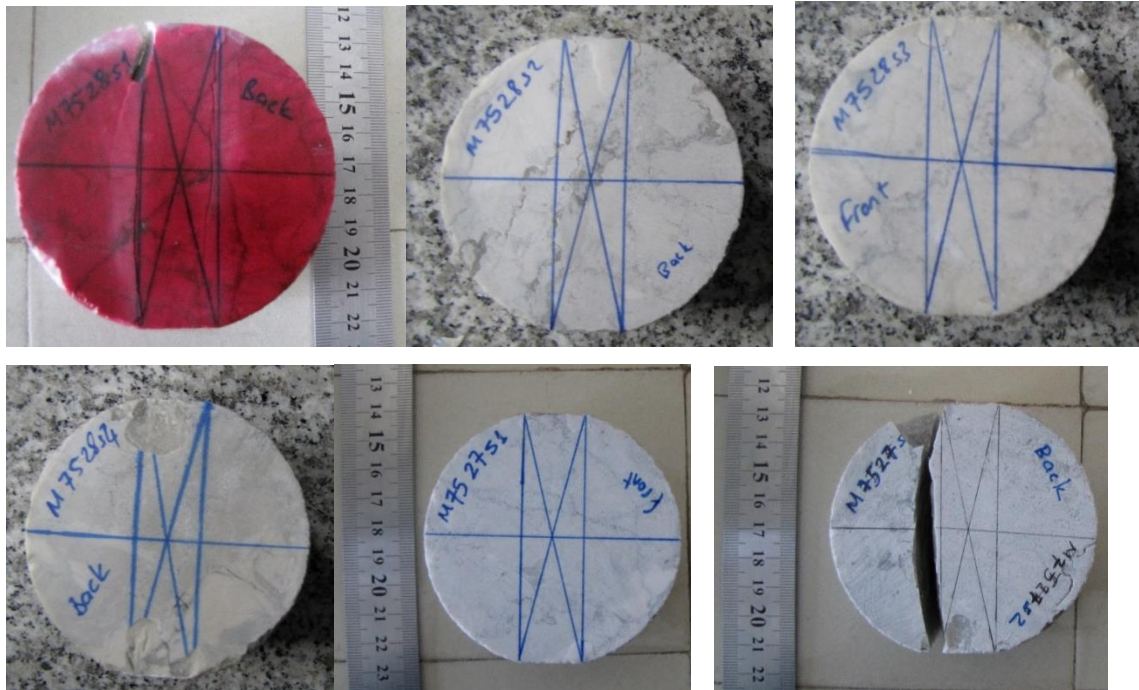
Figure B. 5 Six marbles with a diameter of 75 mm after FBD tests

MAPPING PHOTOS OF DISCONTINUITIES ENCOUNTERED IN

SPECIMENS AFTER EXPERIMENTAL STUDY
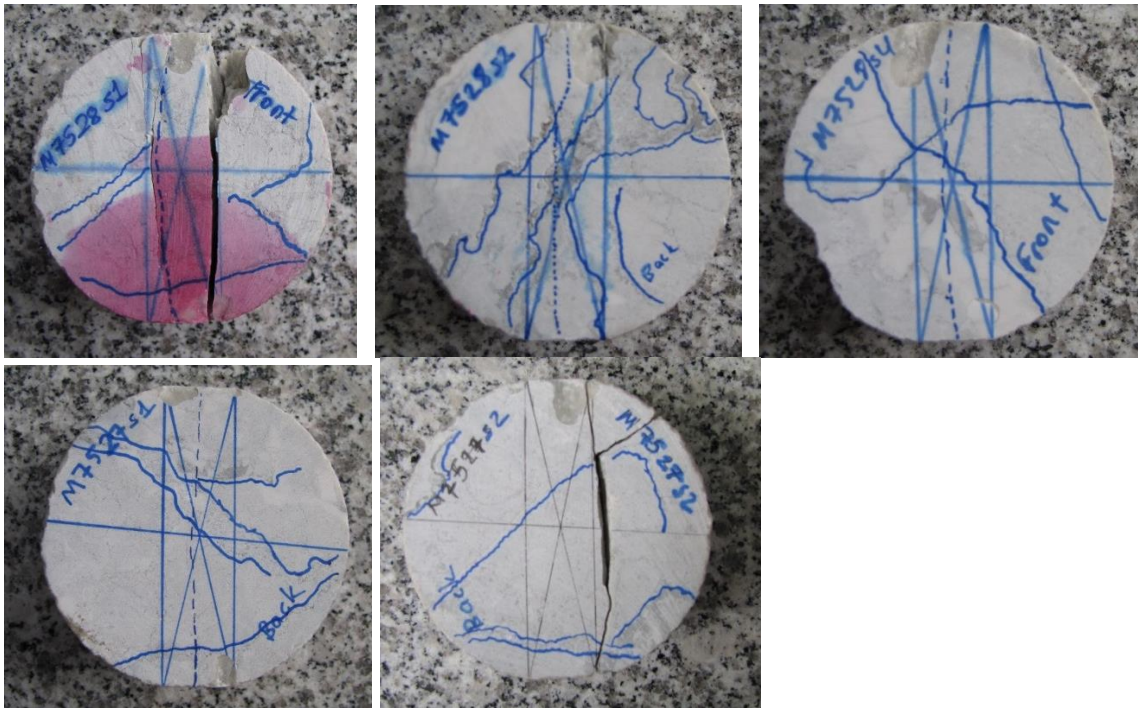
Figure C . 1 Marbles having 75 mm in diameter with discontinuities perpendicular and relatively inclined to loading direction (considered as valid specimens since they don't influence loading direction and crack line represented by dashed lines)

Figure C . 2 Back and front views of marbles having 75 mm in diameter with discontinuities parallel to loading direction (not considered in calculations since it is possible to influence the loading conditions.)

APPENDIX D

# EXPERIMENTALLY MEASURED CRITICAL CRACK LENGTHS OF FBD SPECIMENS
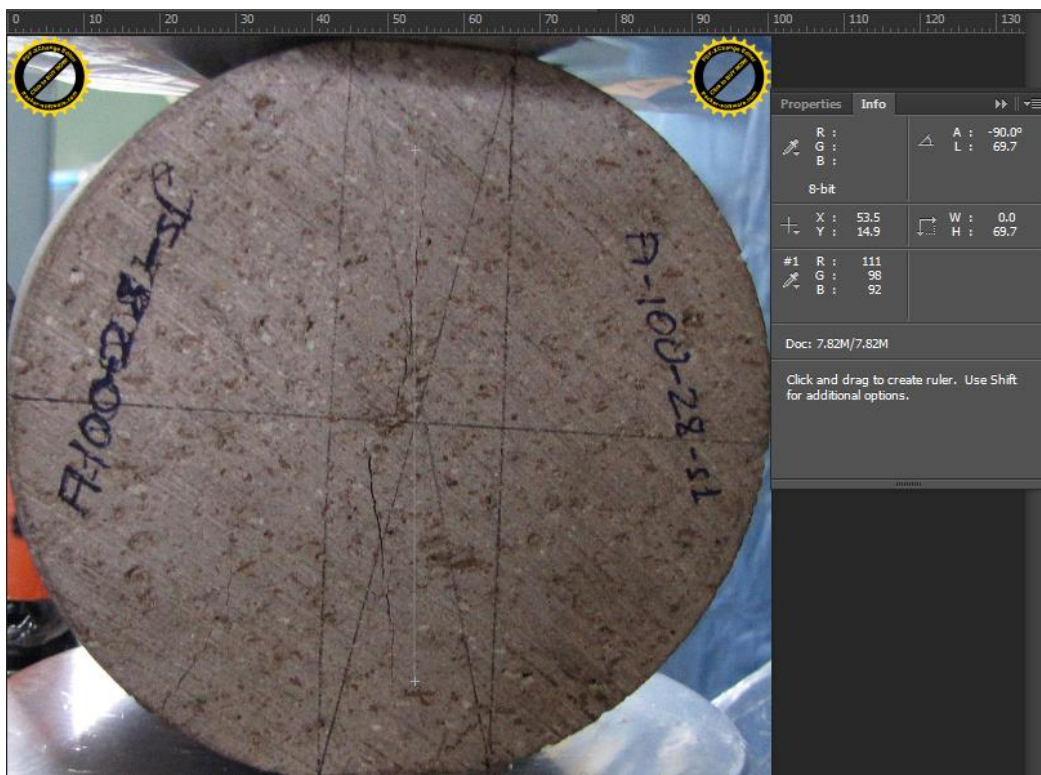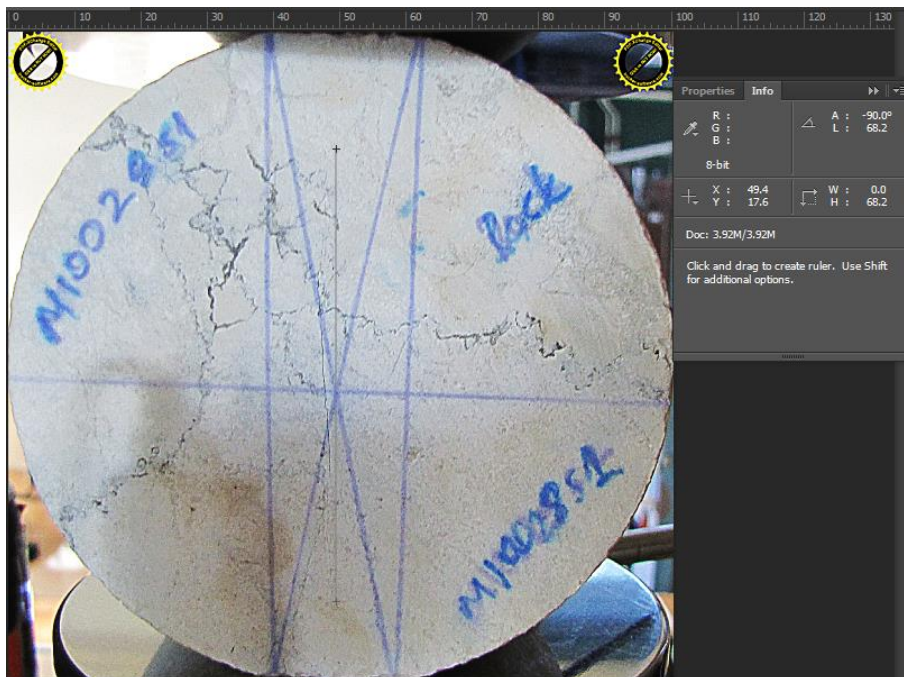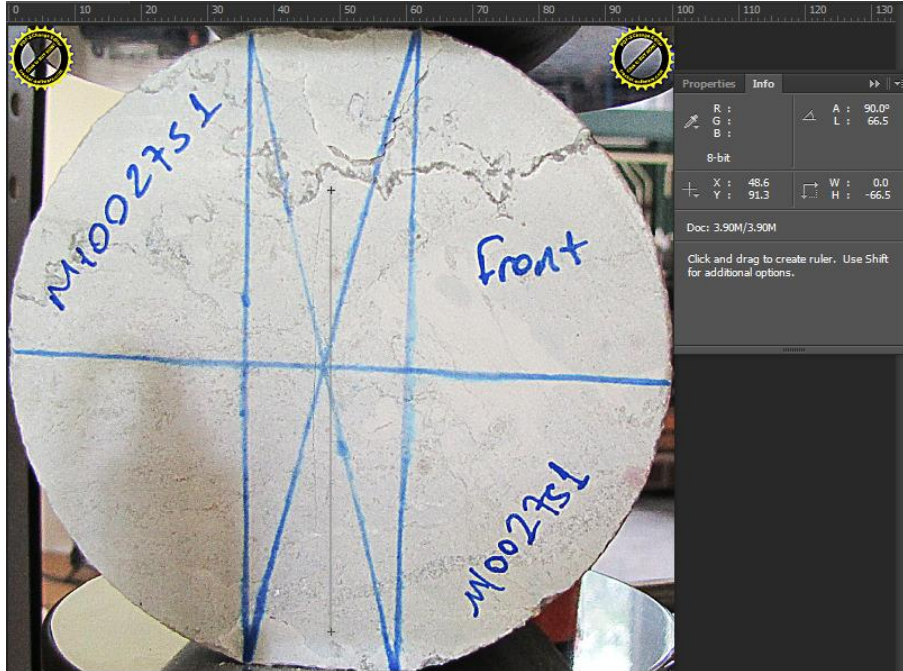

Figure D. 1 Front view of A10028s1 specimen with $2a_{ce}$=69.7 mm
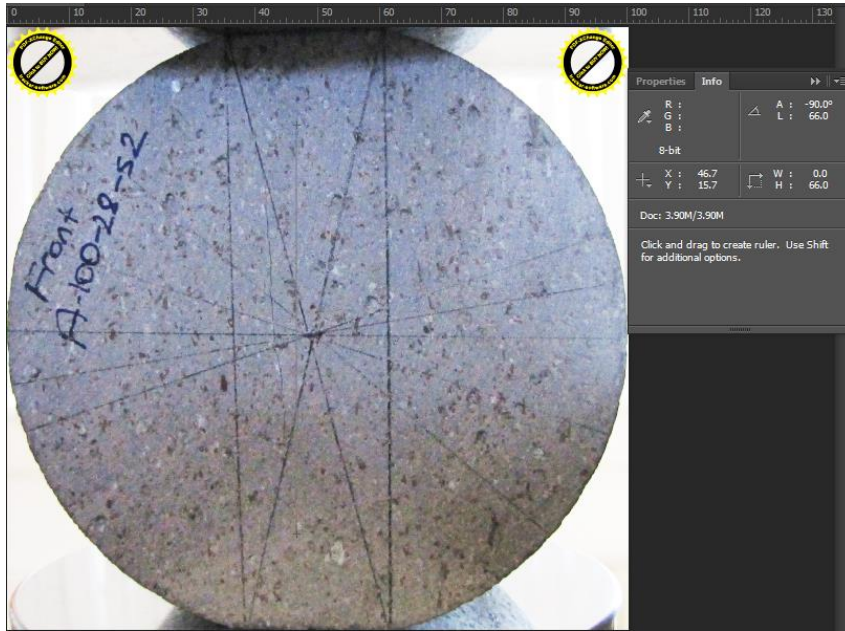
Figure D. 2 Front view of A10028s2 specimen with $2a_{ce}$=66.0 mm
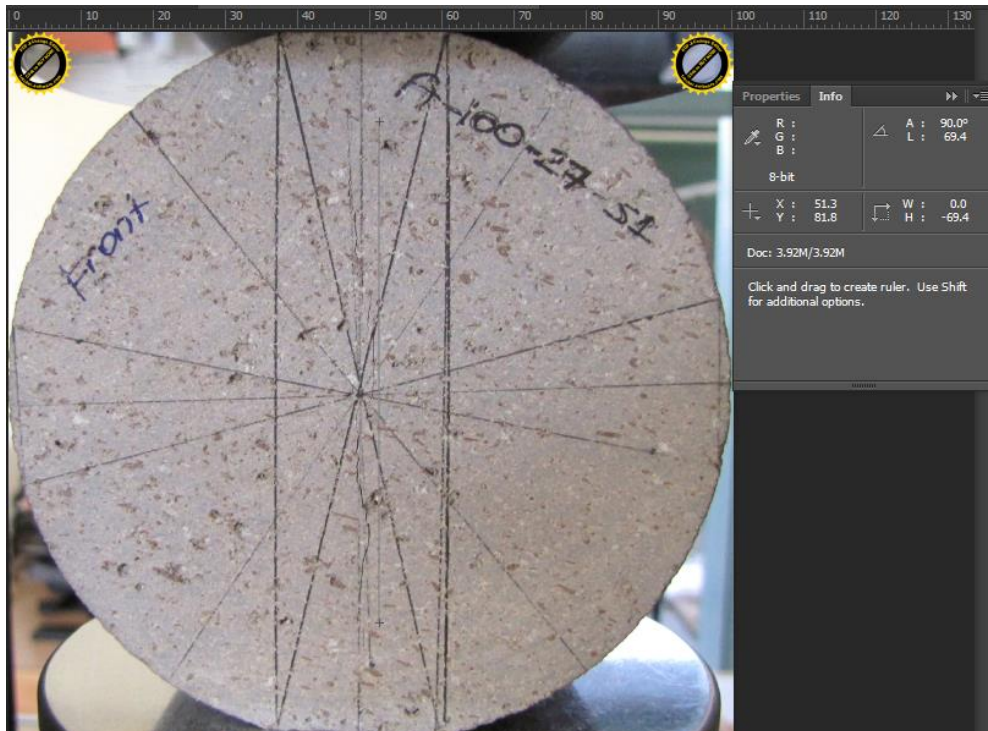
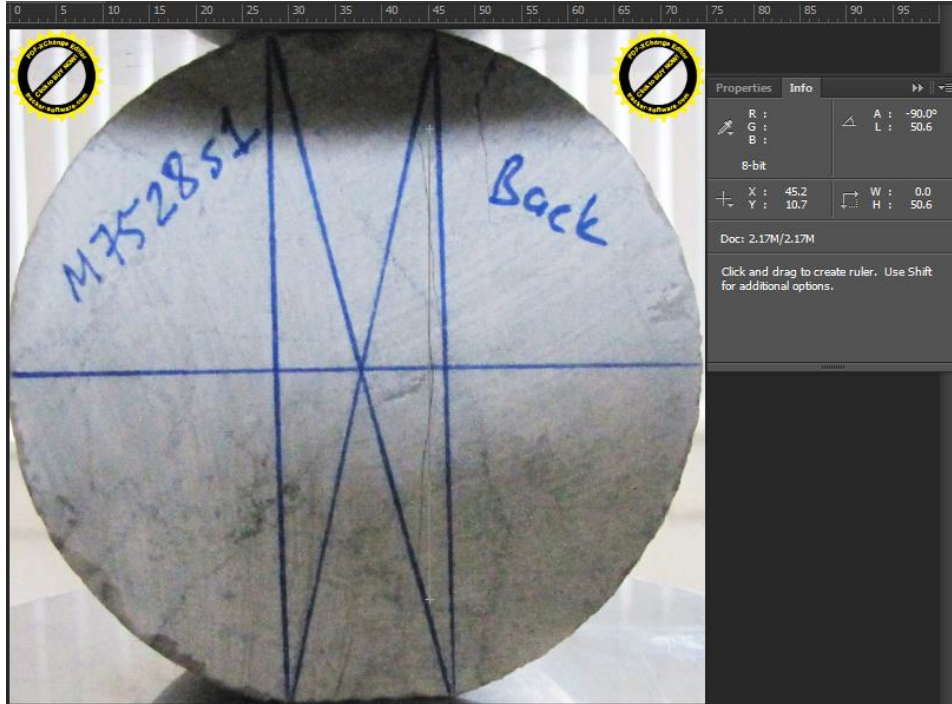Figure D. 3 Front view of A10027s1 specimen with $2a_{ce}$=69.4 mm
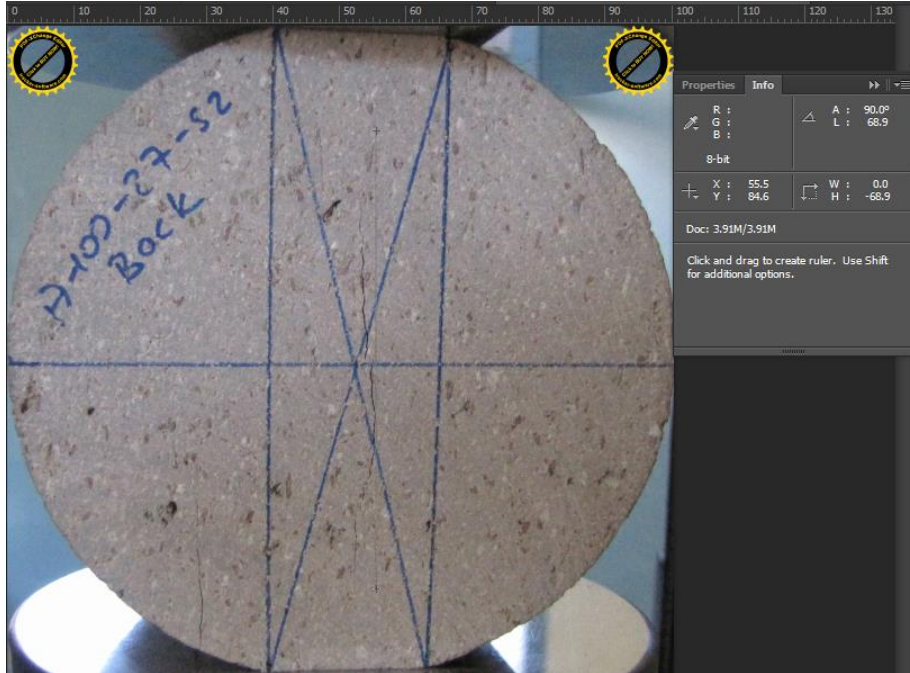
Figure D. 4 Back view of A10027s2 specimen with 2a_{ce}=68.9

Figure D. 5 Back view of A10026s1 specimen with 2a_{ce}=67.2 mm

Figure D. 6 Back view of A10026s2 specimen with $2a_{ce}$=71.3 mm
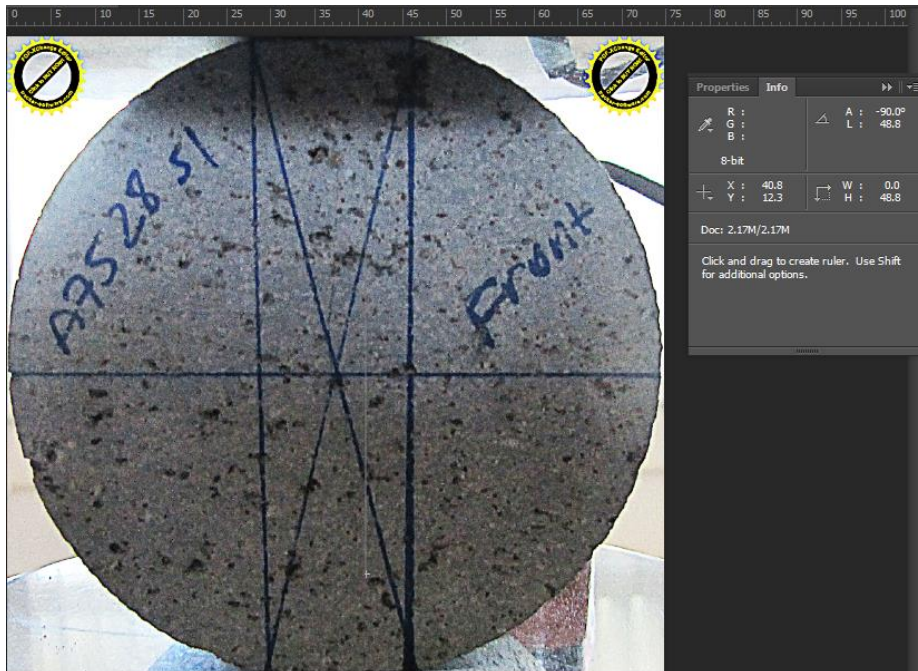
Figure D. 7 Front view of A7528s1 specimen with $2a_{ce}$=48.8 mm
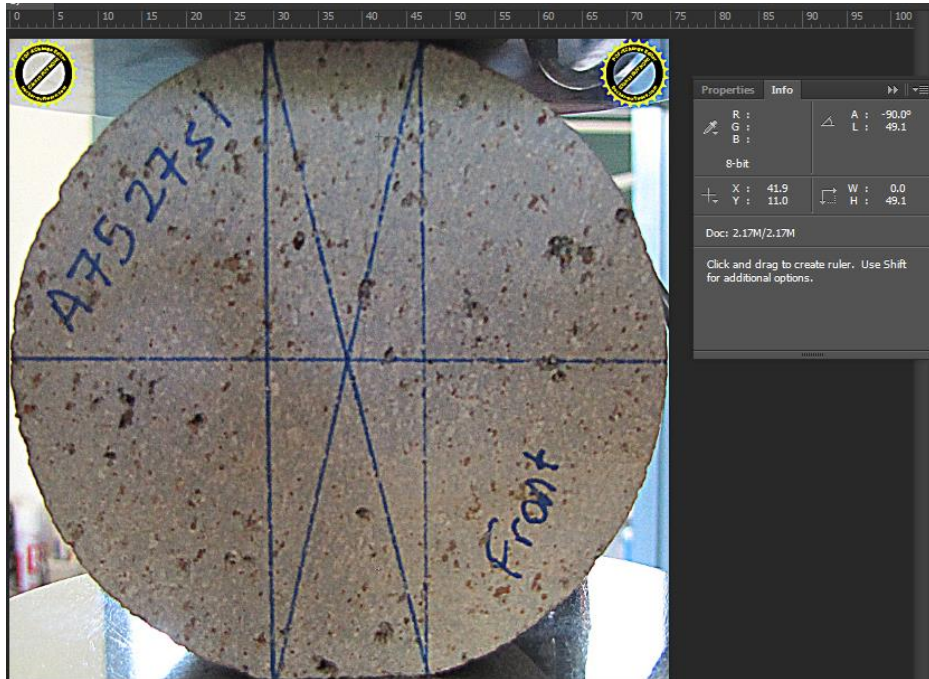
Figure D. 8 Front view of A7527s1 specimen with $2a_{ce}$=49.1 mm
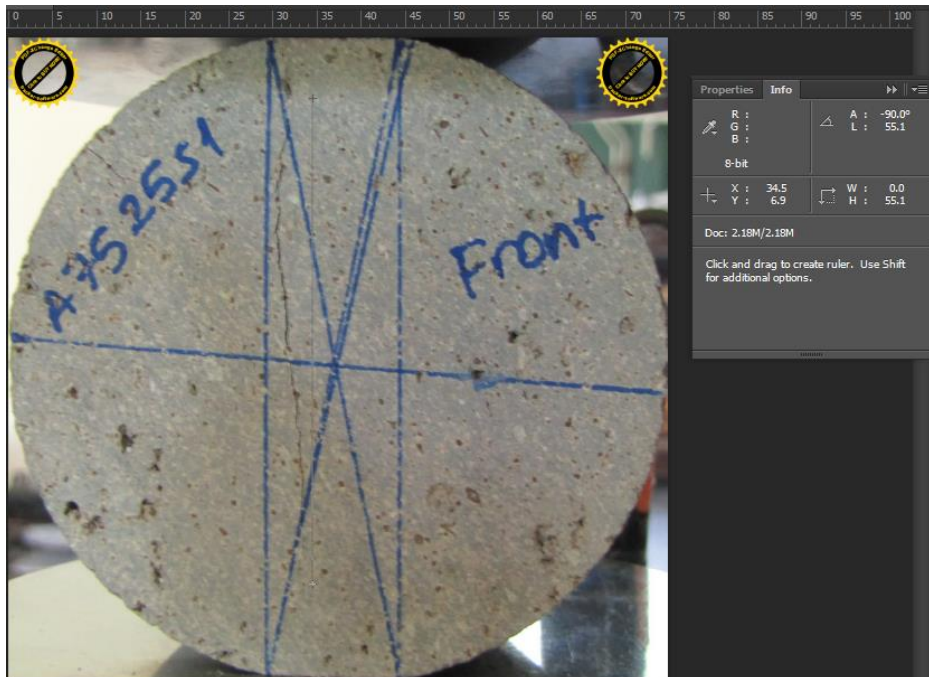
Figure D. 9 Front view of A7525s1 specimen with $2a_{ce}$=55.1 mm
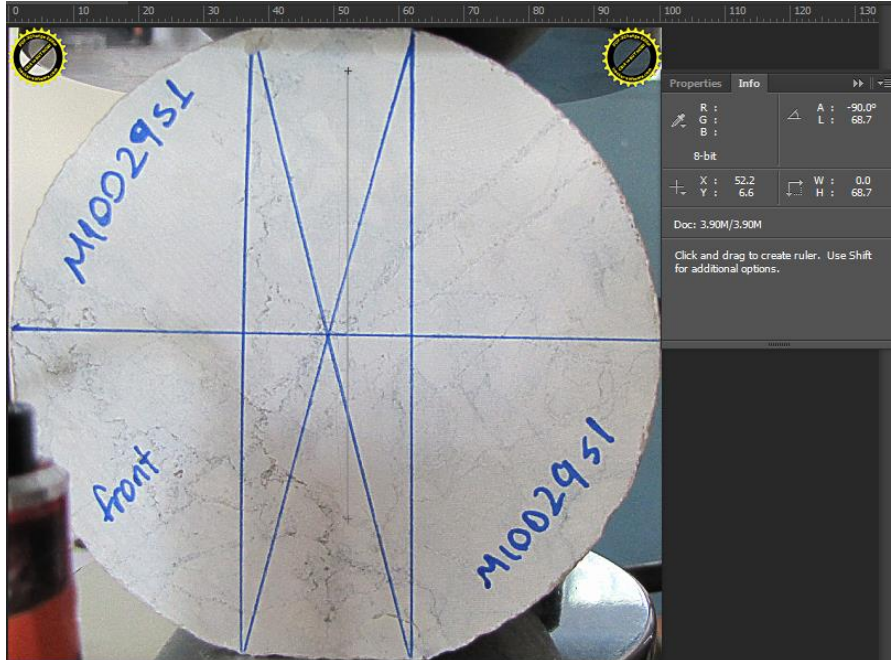
Figure D. 10 Front view of M10029s1 specimen with $2a_{ce}$=68.7 mm

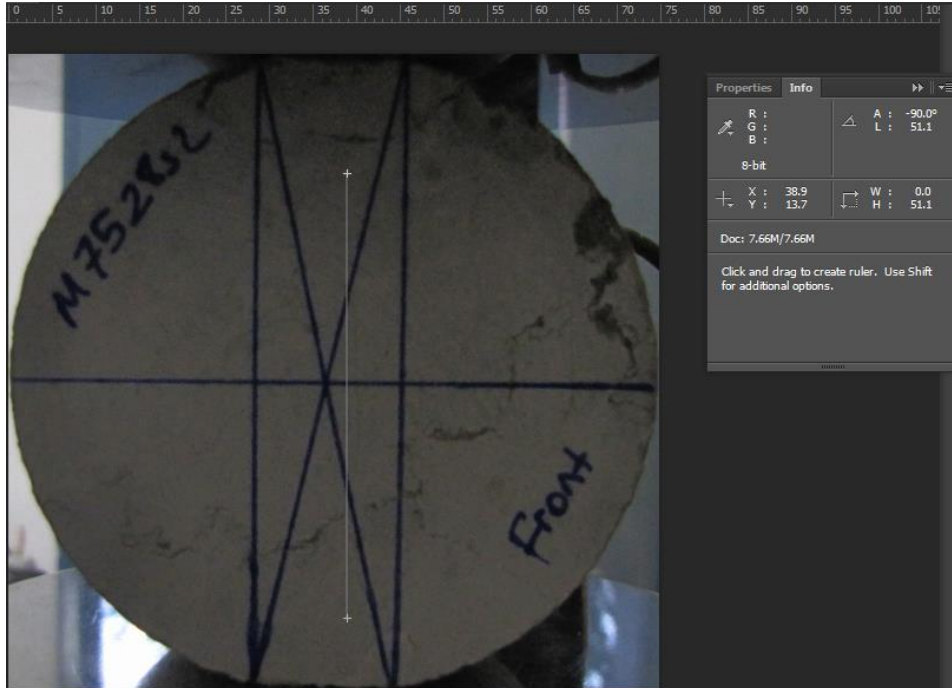Figure D. 11 Back view of M10028s1 specimen with $2a_{ce}$=68.2 mm

Figure D. 12 Front view of M10027s1 specimen with $2a_{ce}$=66.5 mm

Figure D. 13 Front view of M10026s1 specimen with $2a_{ce}$=68.0 mm

Figure D. 14 Back view of M7528s1 specimen with $2a_{ce}$=50.6 mm

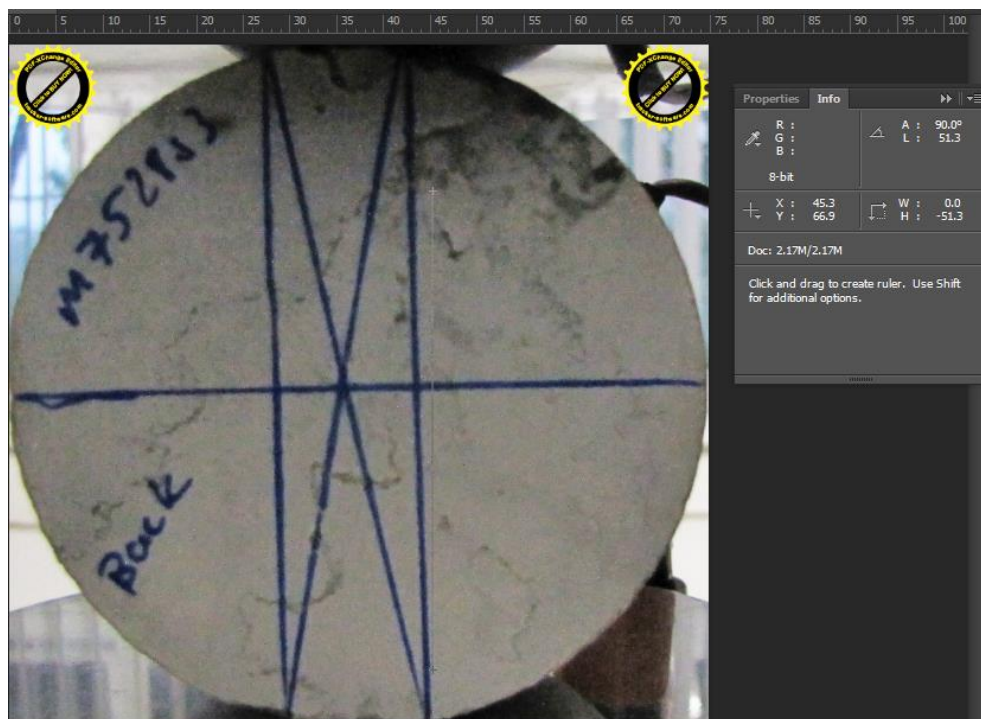Figure D. 15 Front view of M7528s2 specimen with $2a_{ce}$=51.1 mm

Figure D. 16 Back view of M7528s3 specimen with $2a_{ce}$=51.3 mm
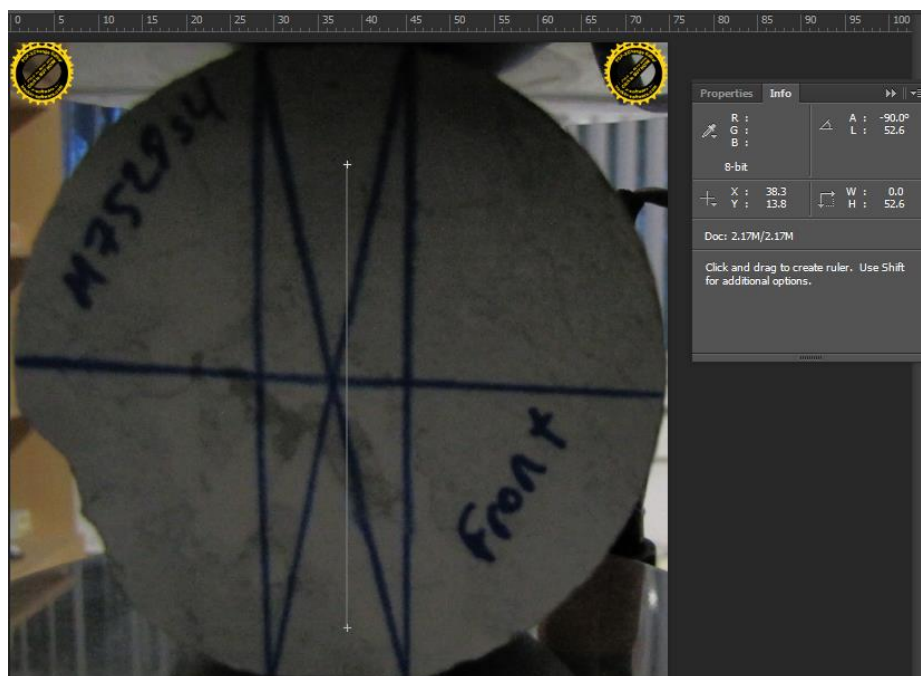

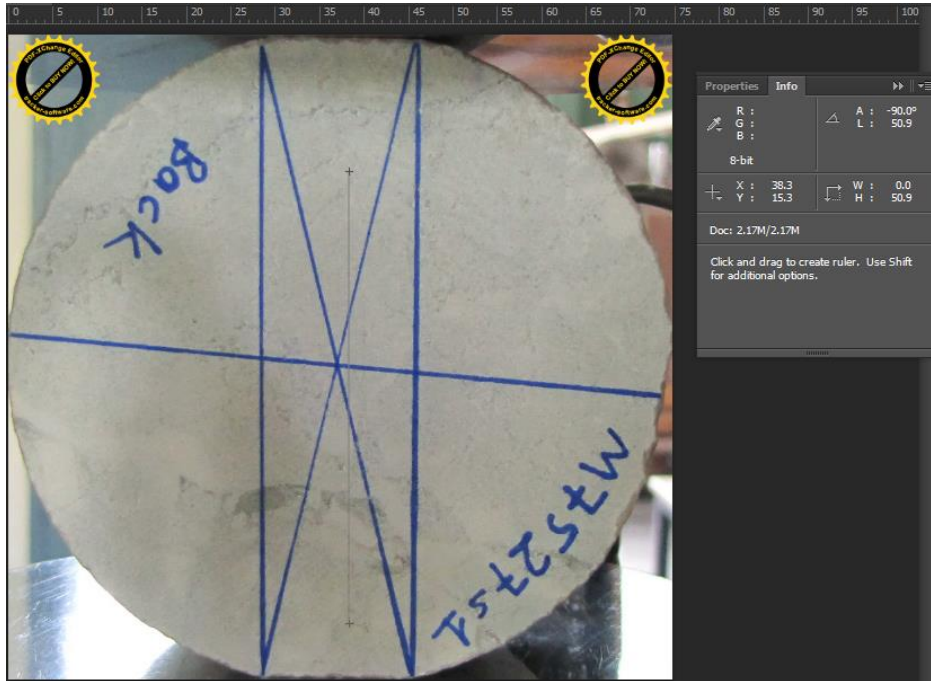Figure D. 17 Front view of M7528s4 specimen with $2a_{ce}$=52.6 mm

Figure D. 18 Back view of M7527s1 specimen with $2a_{ce}$=50.9 mm

Figure D. 19 Back view of M7527s2 specimen with $2a_{ce}$=52.5 mm